TEMPERATURE MONITORING IN SELECTIVE LASER MELTING OF INCONEL 625

By Alexander Shortt, B.Tech.

A Thesis Submitted to the School of Graduate Studies in Partial Fulfilment of the Requirements for the Degree Master of Applied Science McMaster

McMaster University MASTER OF APPLIED SCIENCE

(2019) Hamilton, Ontario (Mechanical Engineering)

TITLE: Temperature Monitoring in Selective Laser Melting of Inconel 625

AUTHOR: Alexander Geoffrey Lawrence Shortt, B.Tech. (McMaster University)

SUPERVISOR: Dr. Mo Elbestawi

NUMBER OF PAGES: xii, 137

Abstract

The objective of this research was to develop a system to effectively monitor temperature in the selective laser melting of Inconel 625. This study established a monitoring system that collects temperature data and describes its relationship with process parameters, develops a control simulation based on the obtained results and determines how to change input parameters in situ. Such research was driven by the unreliability of additively manufactured components, which often contain internal voids and cracks as well as display poor surface finish. With the need for improved part quality, a temperature monitoring system, a promising method of solving several quality issues, proves necessary.

This monitoring system was developed using a pyrometer and a thermal imager mounted on a powder bed metal printer to record the peak temperature of the melt pool. Experiments found that both laser power and scan speed affect the peak melt pool temperature of Inconel 625: as the peak melt pool increases as power increases and as scan speed decreases. A subset of experiments run with a thermal camera further revealed that there is no discernible temperature trend across the laser track, meaning that there was no significant difference in temperature at the start, middle or end of the track. The thermal camera also revealed that temperature across the melt pool resembled a second order response to laser input. Furthermore, according to preliminary offline measurements taken of the primary dendrite arm spacing (PDAS) of Inconel 625 coupons, PDAS increases with peak temperature. In

addition to implementing and testing the monitoring system, this research created and simulated a first order model of the system using a discreet proportional integral derivative controller. Lastly, two separate methods were found to interface a controller with the Omnisint 160 in order to change the laser power based on the temperature feedback

Acknowledgments

I would like to thank my supervisor Dr. Mo Elbestawi for his continued support.

Thank you to all my friends and family.

A special thank you to the team at Mohawk College especially to George Miltenburg and Jeff McIssac.

Contents

Figures

Tables:

List of Abbreviations

3D Printing – Three Dimensional Printing

AM – Additive Manufacturing

CAD – Computer Aided Design

CCD – Charge-Coupled Device

CMOS - Complementary metal–oxide–semiconductor

CNC – Computer Numerical Control

DAQ – Data Acquisition

EBM – Electron Beam Melting

FOV – Field of View

IN625 – Inconel 625

IR - Infrared

MIMO – Multi-input Multi-output

PDAS – Primary Dendrite Arm Spacing

PID – Proportional Integral Derivative

SEM – Scanning Electron Microscope

SISO – Single-input Single-output

SLM – Selective Laser Melting

List of Symbols

°C − Celsius

$cm - Centim°Ceters$

$C_1 - Latent\ Melt\ Energy$

$C_p - Specific\ Heat$

$e - Enery\ Volume$

$E_m - Melt\ Energy$

$E_v - Laser\ Energy$

Gz − Discrete Transfer Function

$h - Hatch\ Spacing$

$J - Joules$

$K - Kelvin$

$K_d - Derivative\ Gain$

$Kg - Kilogram$

$K_i - Intergral\ Gain$

$K_p - Proportional\ Gain$

$\mathcal{L} - Laplace\ Transform$

$mm = Millimeter$

$P - Power$

ρ − Density

s − *seconds*

T − Temeprature

v − Veocity

V − Volmed

W − Watts

Introduction:

In recent years, laser processing technology exploded with the development of high efficiency lasers and the expiration of previously existing patents, resulting in more widespread applications throughout manufacturing technologies and processes. As such, the field of additive manufacturing (AM) has been expanding rapidly. AM is “the process of joining materials to make objects from 3D model data, usually layer upon layer, as opposed to subtractive manufacturing methodologies” [1] and it is commonly referred to as 3D printing (in the field and in the current dissertation). AM is gaining popularity because of its ability to manufacture parts with complex geometries which would otherwise be impossible to produce using other technologies. Furthermore, AM is a much faster process than traditional manufacturing techniques as it does not require the complex set up that is often required with small-batch components. It should be noted; however, that there remain several issues surrounding practical applications of metal AM in industrial settings [2], particularly as it concerns quality and reliability. Parts built from AM are typically poor in surface finish and quality with many porosities and often have dimensional accuracy issues and unpredictable mechanical properties [3]. As a result, researchers are actively seeking control methods that will increase part quality [2] and the field of AM requires such methods in order to create better quality components and to integrate with industry more effectively [3].

The objective of this research is to contribute to this lacuna by developing a monitoring system and a simulated discrete proportional integral derivative (PID) controller in selective laser melting (SLM), a type of powder bed AM that manufactures parts by spreading and processing thin layers of powdered metal one layer at a time, to form a complete structure based on computer aided designs (CAD) of the desired part. The motivation for the implementation of such a system is its potential to solve some of the aforementioned quality issues seen in AM. If such a controller were implemented, parts could potentially display a more uniform microstructure, more consistent mechanical properties and a more uniform melt pool; therefore, resulting in more consistent parts with less porosity and better surface finish.

The break down of this dissertation is as follows. Chapter one is an in-depth literature review on the current state of the art exploring 4 major topics (Modelling, Sensing, Control Strategies, Process Mapping (System characterization)) in AM. Chapter two provides an overview of sensor requirements, sensor selection, calibration and the implementation of the sensors. Chapter three outlines the 5 experiments run trying the determine the effects of laser power and scan speed on melt pool temperature as well as how the temperature relates to mechanical properties and the temperature distribution across a laser path. Chapter four presents the results and discussion of the experiments. Chapter five outlines the model developed as well as the control simulation of the model. Lastly chapter five outlines different ways to interface a controller with the printer

Chapter 1: Literature Review

There have been many research efforts to understand the AM process and to note process parameters which affect the quality and repeatability of SLM manufactured components. These process parameters have been summarized by Spears et al. [2], a summary is shown in Table 1.

Table 1: SLM Process Parameters

Category	**Influencing Parameters**
Laser Scanning Parameters	▪ Pules vs Wave ▪ Beam Quality and Profile ▪ Focal Spot Diameter ▪ Energy output of laser ▪ Scan velocity and acceleration ▪ Laser processing strategy (spacing, hatch pattern) ▪ Pulse width and Frequency
Powder Material Characteristics	▪ Thermal Conductivity of powder ▪ Heat Capacity of powder ▪ Latent head of fusion, Enthalpy and Diffusivity ▪ Melting and Boiling Temperature ▪ Molten viscosity ▪ Coefficient of thermal Expansion ▪ Powder bed temperature ▪ Surface free energy ▪ Solubility
Powder Bed	▪ Particle Morphology ▪ Particle size distribution ▪ Density ▪ Ability to absorb thermal radiation ▪ Emissivity ▪ Recoater velocity, pressure and type ▪ Layer Height ▪ Thermal conductivity of powder bed ▪ Heat capacity of powder bed

Build Environment	▪ Oxygen level ▪ Shield Gas, molecular weight and viscosity ▪ Heat capacity of atmosphere ▪ Build atmosphere pressure ▪ Thermal conductivity of atmosphere ▪ Convective heat coefficient ▪ Atmosphere flow velocity from heat change ▪ Ambient Temperature ▪ Surface free energy of atmosphere and bed ▪ Build plate thermal conductivity

These parameters have been identified as input and output, and controllable, uncontrollable and partially controllable [3]. The block diagram below simplifies all these parameters into a more visual method of looking at the AM processes in terms of controllable inputs and measured outputs (Figure 1). The system itself consists of all fixed parameters such as particle size distribution and recoater properties and contains all other influencing parameters in Table 1.0 which effect the measured outputs.

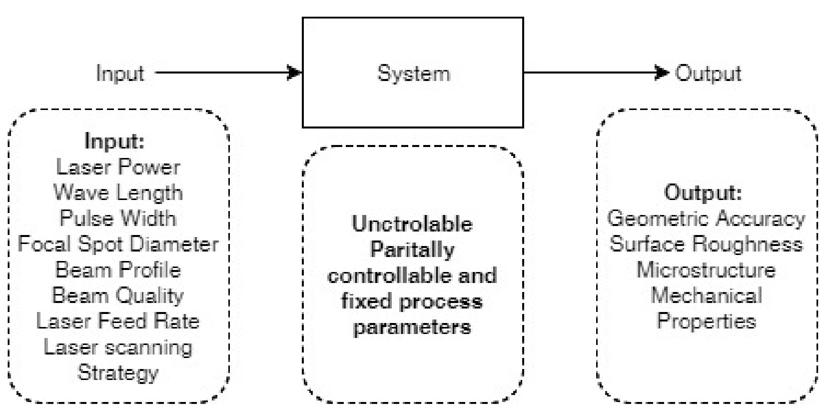

Figure 1: Simplified AM Process Inputs and Outputs

During the SLM process, all output parameters have a direct dependence on the controllable inputs as well as uncontrollable, partial controllable and fixed process parameters. Thus, to maintain the quality of the components made using SLM, some form of control should be in place to manipulate these input parameters to obtain the desired output parameter. Therefore, if it is necessary for a control system to be put in place to achieve the necessary quality in AM for usable parts there are several other factors which need to be resolved.

For any control system, it is necessary to have a model of the system, the ability to sense an output or outputs of the system and to implement a control strategy which can manipulate an input which will change the measured output(s). Furthermore, it is desirable to have some priori understanding of the system to help make decisions in the controller. This literature review examines these 4 major topics (Modelling, Sensing, Control Strategies, Process Mapping (System characterization)) in AM specifically for the in-situ temperature measurement of Inconel 625 (IN625) in an SLM process as well as other materials and AM processes.

Process Maps

Process maps are any form of map which relates an input(s) to an output(s), for example, in business process maps are often used to relate complex economic processes into simpler relationships for better understanding of the process at hand. Process mapping in controls is very similar in the fact that it tries to take complicated process outputs and simplify them into relationships between key input process variables. A common process map in microstructure formation is the “solidification map” used to map microstructure of a particular material in welding applications, laser treatment, continuous casting, directional casting and single crystal structures based on solidification cooling rates and thermal gradients. This solidification map is a very useful tool for understanding how a material forms its microstructure however, in a controls application, monitoring the thermal gradient and cooling rate is very difficult and these solidification maps must be translated into key input process variables which can be controlled.

Solidification maps are typically generated in a simulation such as a Finite Element Modeling (FEM). Solidification maps are rarely generated from experimental trials due to the complexity of monitoring the thermal gradient and cooling rate in often very extreme conditions such as casting and laser cladding. There has been effort to generate solidification maps for AM using FEM and research has been done to “translate” solidification maps into input process variables using FEM and other numerical approaches. However, a limited amount of research directly relating to AM is available and much of the published work comes from the same group of authors.

Another approach to developing microstructure process maps for AM is using standard coupon testing and material characterization techniques to characterize the output microstructure based on varied input parameters such as scan speed and laser power. In this paper, process mapping will be examined for their use in AM, furthermore, an overview of several studies is provided to give a basis for the different techniques used to generate process maps for TI-Al alloys. Finally, an overview of work done to characterize IN625's is provided.

Examples of methods for finding a process map

In the following section, research is examined in which process maps have been developed for Ti-6Al-4V, a very popular material in AM. As mentioned above, the development of process maps is primarily done with the use of simulations such as FEM and/or numerical solutions to solve for thermal gradients and solidification cooling rates. These maps are typically validated through experimental trials and microstructure examination from a varying number of techniques such as: traditional standard coupon testing, material characterization technique, Optical Metallography (OM), Scanning Electron Microscopy (SEM), Transmission Electron Microscopy (TEM), Energy-Dispersive (X-ray), Spectrometry (EDS), and X-Ray Diffraction (XRD).

Gockel et el. [4] describe a method to find a process map by translating existing solidification maps of Ti-6Al-4V into maps based on laser power and scan velocity for use in wire fed electron beam melting. By developing an FEM of the AM process, Gockel et al. are able to determine the microstructure for pairings of absorbed power and scan velocity. By comparing the simulated results for microstructure to existing solidification maps, the known pairings of velocity and absorbed power in the melt pool can be mapped over the thermal gradients and solidification cooling rate of the existing solidification map resulting in a new process map which shows the resulting microstructure based on absorbed power and scan velocity. It should be noted that the process map is developed using a simulation which holds other process parameters constant such as existing temperature in the component. This study also noted that the melt pool geometry directly influences the microstructure of the formed component and furthermore that the melt pool geometry cannot be independently controlled without influencing the microstructure of the formed component. This was discovered when comparing a previously developed process map for controlling melt pool dimensions (expressed in terms of absorbed power and scan velocity) to the newly developed process map for microstructure where the regions of constant grain morphology correspond to those regions of constant melt pool dimensions.

Beuth et al. [5] give an overview of work being done to create a process for developing process maps for any AM process with any material. In this approach, a patent pending process is used involving the development of three FEM's describing three conditions or tool paths which can occur in an AM process. The first is a single track laid on a substrate far from any free edge, the second is a single track laid next to existing tracks and finally, a transient case where the track is laid on an external radius which encapsulates transient thermal properties in the track and is a function of location. Using these three FEM's a process map of melt pool area is developed which describes melt pool area based on absorbed power and scan velocity. Based on previous works [4], [6] melt pool geometry directly corresponds to the microstructure of the finished components, thus making geometry directly control microstructure, and allowing the models to generate maps based on process variables to control microstructure. Beuth and Gockel have used this approach in several other papers validating the process through experimental trials [7][8].

Kobryn et al [9] describe a process of finding process maps through experimental trials as well as FEM. Two different types of process maps are generated; one comparing laser scan speed to grain width for thick and thin wall deposits, and another map comparing incident energy to grain width. Data collected from manufactured samples was done using standard metallographic preparation techniques, XRD analysis and automated electron-backscatter-diffraction. On top of developing maps for AM, solidification maps for casting were also developed and compared to points found for the AM process to evaluate the applicability of existing maps to AM. This study concludes that that the solidification map developed for casting is applicable for predicting grain morphology in solidification in direct laser fabrication. This is promising for the development of a map for IN625, if existing solidification maps have already been created.

Bontha et al.[10] focus on the development of microstructure based thermal process map for thin wall structure in laser based fabrication. These maps are developed using a 2D Rosenthal solution for a moving heat source and verified using FEM analysis. As with some of the other studies presented above, the solution for the process map is developed in terms of solidification cooling rate and thermal gradient as a function of process parameters. The key conclusion drawn from this study is that both laser power and scan velocity change solidification cooling rates and thermal gradients during the manufacturing process, therefore changing the resulting microstructure. This suggests that scan speed and laser power directly affect the grain morphology within the completed component, an important piece of information to generate microstructure maps for IN625.

C. Li et al. [11] develop several process maps for IN625 based on single track builds through variation of laser power and scan speed. Multiple single-track passes were made on a substrate at 5 different scan speeds (500, 1000, 1500, 2000, 2500 mm/min) at laser powers varying from 45 W to 60 W in 5 W increments. Each track was examined using optical microscopes and were cross section perpendicular to track direction using traditional sample preparation techniques. From these examinations, maps of track melt depth, track width layer height, contact angle and surface roughness were created based on the laser power and scan speed. Furthermore, using a scanning electron microscope, a process map is developed for predicting the dendritic arm spacing within the microstructure based on scan speed and laser power. It was observed that SLM manufacturing IN625 has a typical columnar dendrite microstructure caused by the rapid cooling, which also causes the spacing of the dendrite arms to be very fine. Compared to Electron Beam Melting (EBM) manufactured samples by Dinda et al. [12] the arm spacing is in SLM process IN625 is of one magnitude smaller.

Microstructure analysis

Although there has been a significant effort and successful developed of process maps for Ti alloys, few such process maps exist for IN625. That being said, efforts have been made to better understand the behaviour of IN625 microstructure within various AM processes. Some efforts have approached the issue by developing new techniques for evaluating microstructures, while others have used a more brute force technique of trial and error, both having value towards deriving process maps for IN625.

In an effort to better understand the rapid solidification which occurs in additive manufacturing, McKeown et al. [13] employ a relatively new form of microscopy known as dynamic transmission electron microscope (DTEM). The DTEM employed is capable of capturing images in the Nano scale resolution range allowing for images of the solidification process to be captured, furthermore the system captures images in the nanosecond time range giving series of images over time of the solidification process. This allowed McKeown et al to characterize the thermal gradients of Al-Cu and Al-Si. Additionally, the author suggests the DTEM could be used in-situ to monitor the thermal gradients and solidification front velocity which could be meaningful for the use of ion process control of microstructure. However, to use the DTEM, a test fixture is required and the integration of the apparatus into an available AM machine would be nearly impossible.

In an article by Murr et al. [14] the microstructure of EBM manufactured IN625 is analyzed in samples of both cylindrical and rectangular components. The microstructure of both cylindrical and rectangular samples as manufactured and hot pressed are examined using several techniques including: (OM), (SEM), (TEM), (X-ray), (EDS), (XRD) and are compared to nominal microstructure samples of IN625. This is a good technique if the equipment is available due to the amount of information which can be provided; by comparing AM samples with nominal samples, a comparison between desired microstructure and the microstructure achieved can be achieved and a target can be set. It was found that IN625 in an as manufactured state using EBM is a nearly full density component with a heavy Ni-Cr fcc matrix, with a unique columnar structure of thin bct Ni3Nb precipitates. Fully dense parts from EBM are not uncommon due to the high heat experienced in the build process, however in Selective Laser Sintering (SLS) and SLM components, part density is often an issue. Furthermore, this microstructure is likely not to be seen in SLS and SLM due to the lower temperature in these processes.

Research by S Li et al [15] examines the microstructure of SLM formed samples that were made of IN625 powder. It was observed that no voids were formed during the manufacturing, which is contrary to many other trends in materials of SLM-based manufacturing and IN625 specific studies which often have porosities and voids. A potential explanation for this is that the powder was preheated to 50 °C for 5 hours prior to manufacturing, which may have helped to create a more homogenous melt pool temperature, resulting in a denser component. Both SEM and XRD were used to examine the resulting microstructure. It was found that the microstructure was composed of elongated columnar crystals and no precipitates were formed in the matrix. Furthermore, similar to C. Li et al. [2][11], small dendrite arm spacing was observed of approximately 5 um which is also correlated with the rapid cooling occurring in the melt pool. Vickers hardness test values of the formed component were 254 ± 6. On a macro scale of the component, a “V” shape pattern was noticed in the track comparable to that seen in welding applications. Furthermore, solidified grains had a clear orientation in the direction of travel of the melt pool, which coincided with the direction of cooling.

The following table summarizes several more studies regarding the development of process maps in AM and the microstructure of AM produced IN625.

Table 2: Summary of Process Mapping Research

Study		Purpose	Techniques Used	Conclusion
[12]	IN625	Study Microstructure from varying process parameters in as manufactured components (Laser Power, Scan Speed, Powder Feed rate)	X-Ray diffraction, Traditional Microscopy samples	• Parts can be formed free of porosity and cracks • Microstructure consisted mostly of columnar dendritic structure • High Hardness was observed in as manufactured samples due to fine microstructure caused by rapid cooling
[16]	Ti-6Al-4V	Relating laser process variables to solidification rate and thermal gradients using simulations and numerical solutions	FEM, 2D Rosenthal Solution	• Variations in laser process parameters (laser power and scan velocity) can change solidification cooling rates and thermal gradients
[7] [8]	Ti-6Al-4V	Develop process maps for microstructure control by controlling melt pool geometry and validate through an experimental trial	2D FEM and microscopy of manufactured samples	• Constant melt pool cross sectional area resulted in constant solidification rate • It is possible to control resulting microstructure by controlling melt pool width or other geometries

Sensors for Online Monitoring

There have been many efforts in AM to monitor the process in one form or another, different researchers have selected different types of instruments for different purposes. Many of these research efforts use photoelectric pyrometers or thermal imaging for temperature measurements in the melt pool and digital cameras to view a larger area within the build chamber or to monitor melt pool geometry, while other researchers have used laser ultrasonic instruments to monitor for defects. The following section outlines some of the more recent research into offline and online monitoring techniques and further summarizes several articles which have successfully monitored an aspect of the AM process for reference.

Doubenskaia et al. [17] use a photoelectric and CCD type pyrometer to capture the thermal radiation emitted by the heat affected zone during SLM. The pyrometer is used for overall radiation intensity while the CCD camera tries to capture the brightness temperature. The setup used to capture this information requires integration of the optics with the laser and is shown in Figure 2.

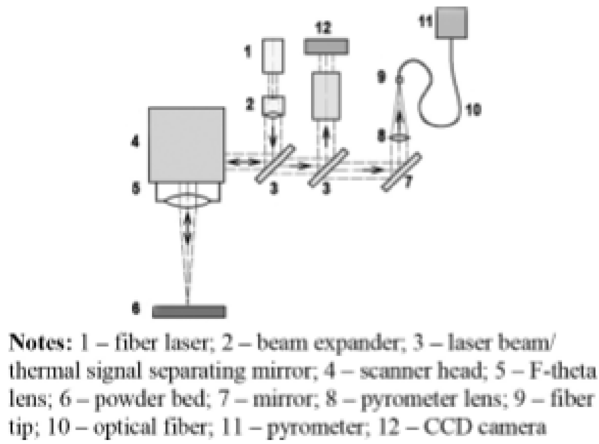

Figure 2: Schematic of the Optical System [19]

What allows this setup to be possible is a partially reflective mirror which separates laser radiation from the thermal radiation of the melt pool. The settings chosen for their measurement apparatus are shown below. Using this monitoring technique, Doubenskaia et al. were able to observe a change in temperature distribution when hatch distance and layer thickness were changed. However, the exact temperature could not be found due to the changes in emissivity with temperature as well as focus errors within the optics setup. A disadvantage of this sensor setup, besides the complexity of integrating the optics with the laser system, is the time constant associated with image analysis. The thermal radiation of the melt pool does not translate to an intensive signal within the photodiode. Because of the radiation's weak signal, a strategy is necessary to filter out electronic noise. The proposed strategy is a modulation shutter; however, this modulation results in a 50 ms delay between measurements. If a closed loop system were to be implemented with this setup, it would be very difficult to create an accurate control system because the time between measurements is so large. A summary of the two devices can be seen in Table 3.

Table 3: Pyrometer Parameters

Type of Device	**Detector**	**Wavelength**	**Temperature range**
Photoelectric: Dual Wavelength	InGaAs	1.26 um with a band width of 100 nm	1200 -2900k
CCD Digital Camera	CCD	Unknown	1200 – 1800k

Jacobsmuhlen et al. [18] used a CCD camera in a slightly different way. Rather than trying to acquire temperature, a pyrometer which functions in the visible light spectrum was used to capture high definition images of the entire build layer. Pictures were gathered between each successful build layer and after recoating. The purpose of this was to look for visible defects in the build process and correlate these defects to visible changes in captured images.

The camera is mounted outside of the actual machine, which unlike Doubenskia's work, does not require modification of the laser system. This, however, also means that photos could not be taken coaxially with the melt pool. Instead images needed to be tilt shifted after acquisition to correct for the angle which would make real time control near impossible due to processing time of images. Overall, this method was very successful at determining defects between layers and identifying potential causes for the defects. However, it would be difficult to implement this into a closed loop control system as image processing would be time consuming and furthermore, buildup of powder or spatter on the view port could cause focus issues in the quality of the obtained image.

Krauss et al. [19] implemented a similar monitoring system to Jacobsmuhlen, using an digital thermal camera on the outside of the SLM machine. The purpose was again to characterize defects and porosity within the SLM process as opposed to creating an active control system. The thermal camera chosen used a microbolometer type of detector which offered some advantages and disadvantages. It costs significantly less than other IR cameras, however it also has a large time constant, making it inappropriate for active control of the SLM process. The interested reader will find Kraus does a good job justifying the selection of optics and wavelength (2012), the camera specifications are outlined in Table 4.

Table 4: Camera Specification [19]

Type of Device	**Detector**	**Wavelength**	**Temperature range**
Microboloemeter Digital Camera	Microboloemeter	8 – 14 um (Filtered Germanium)	1700C

2007 Kruth et al. [20] developed and patented a system using a photodiode and CMOS camera similar to the work of Doubenskaia and Gusarov [21]. The purpose of the system is to control and stabilize the temperature within the melt pool. Experiments were performed with complex geometry and overhangs with a high level of success. Shown in Figure 3 is the prototype setup for the experiment including the pyrometer, digital camera and optics. It is interesting to note that the partially reflective mirrors allow for the thermal radiation to pass through without interrupting the laser beam and is a proof of concept that pyrometers and IR cameras can be used coaxially to measure the melt pool. However, further information on the pyrometer and CMOS characteristics could not be found.

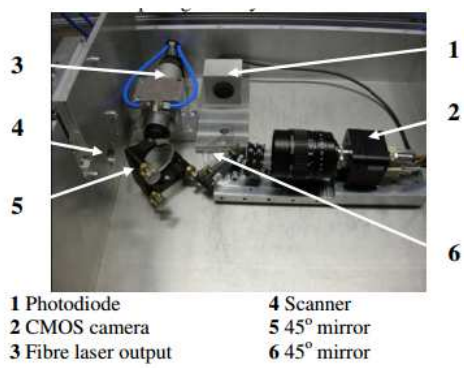

Figure 3: Prototype Monitoring System [20]

All of the above-mentioned research uses additional light sources, either in the build chamber or outside in order to create high resolution pictures. This can be an issue because of the heat generated by the light which may cause solid state sintering. Many other studies have used IR camera near IR cameras, pyrometers and photodiodes to collect various information in AM processes. Throughout the remaining section many references will be made to studies which have used this technology in closed loop controls and model validation.

In a paper by Segerstark et al [22], using the same methodology as Zeh et al [23] and Quain et al [24] thermocouples (TC) are fixed (welded) to the build plate and used to monitor the temperature. This approach presents several issues due to the high temperature of the process including; TC's coming disconnected from the build plate due to melting, TC junctions becoming damage or disconnected and most importantly the slow response time of the TC. To overcome the first two issues Segerastark tests a protective sheet over the TC, which is tested at various thickness to test the influence of the barrier with nominal effects (As seen in Figure 4). However, no solution for the response time of the TC is suggested, due to the rapid heating and cooling of the single wall track the TC does not respond fast enough to capture the peak temperature [25]. In total three TC's were installed to monitor the temperature of a single-track thin wall build in various locations. This would be a valuable test to conduct to see the temperature differences at the beginning middle and end of a track to see absolute differences between the points and from layer to layer. However, the TC's cannot be reused without additional setup and are not suitable for real time control of the process. This idea is later explored further in Chapter 2.

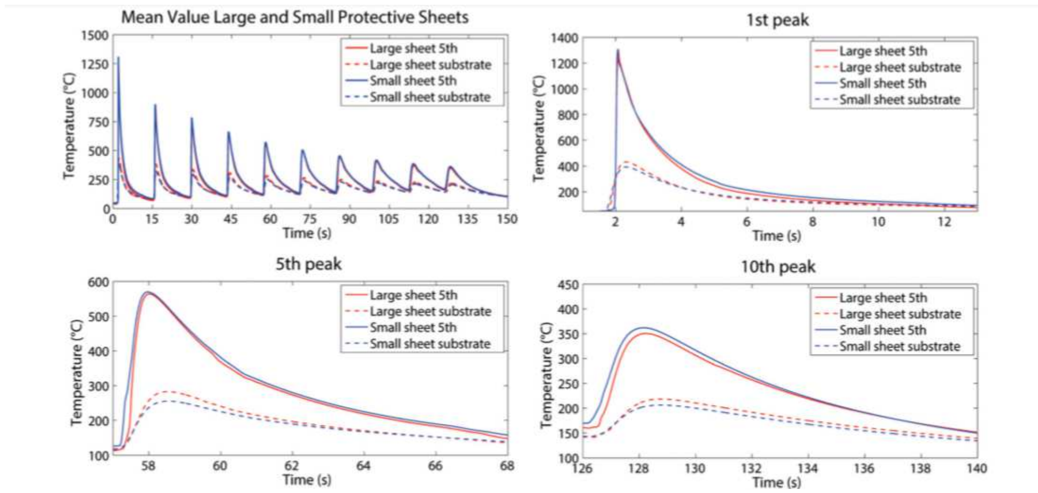

Figure 4: Temperature Measurements [22]

Rieder et al [26]. use a different approach to monitor the AM using an ultrasonic probe imbedded in the build plate. This provides some advantages and disadvantages when compared to the more common pyrometer sensors. Firstly, the ultrasonic sensor has a very fast sampling rate which is great in a controls application, and is achieved due to its sensitivity. This sensitivity is also a disadvantage as it is more susceptible to changes in environment and may require heavy filtering. The particular sensor used in this study sampled at a rate of 1 sample every 4 us, where as some CCD cameras can take up to 50 us to acquire an image and additional time to analyze. Another advantage of this sensor is the simplicity for set up, integration of the sensor was done by machining a pocket in the build plate in which the sensor is attached. There was no need to integrate the sensor with existing laser and optic systems, making it far easier to employ.

Spicer et al. [27] prove that it is possible to monitor the microstructure of stainless steel alloys using laser ultrasonic monitoring. However, this was accomplished in a test fixture with controlled conditions which will be dynamic in AM and controlling the dynamics of the process in order to derive the microstructure would be extremely difficult. Furthermore, to infer the microstructure in the alloy, the temperature of the test sampled was required. As noted from some authors [2],[28],[29] monitoring the exact temperature is difficult due to changes in emissivity and optical obstructions. However, Doumanidis et al [30] have shown how this can be overcome and is discussed in the control strategy review. Overall, most research efforts in monitoring have focused on measuring the temperature or shape of the melt pool. The following table summarizes several efforts of developing monitoring systems in AM.

Table 5: Summary of Monitoring Systems

Study	**Monitoring System**	**Physical Setup**	**Application**
[31]	IR Imaging camera integrated into EBM system	Mounted outside build chamber with view port	• In-Situ measurements of surface temperature of entire build surface for monitoring defects
[32]	Coaxially installed IR camera with IR filter	Integrated into laser system	• Control of the heat input and size of the molten pool

[33][34]	Laser ultrasonic sensors: wave is generated and monitored for variation	Wave generator and receiver mounted inside chamber	• Defect Detection
[35]	Combination of laser probe to generate (Surface Acoustic Waves) and Optical system for detection of that wave	Integrated with machine on outside with access ports	• Monitoring local temperature
[36]	Combination of two thermal cameras with different shutters. Attempt to develop shutter less IR camera	Specially designed view ports for elimination of powder build up and filtering wavelengths	• Porosity detection (In-situ) • Study effects of beam spot size
[37]	IR Thermal imaging	Mounted on tripod with view port, to handle heat and a specially designed heat shield is mounted inside the build chamber to the protect lenses	• Monitor melt pool size • Temperature profile in melt pool

Modelling Approaches

In any control's application, a good model of the process is necessary in order to control said process. In the case of AM modelling there have been many different types of models created to describe different aspects of AM. However, most of these efforts of modelling for control have taken place in powder deposition processes, while models for powder bed applications have been focused on Finite Element Modelling (FEM). As such, this literature review covers model approaches for controls of powder deposition as well as models used in FEM's of powder bed processes.

Existing Models for Control

Han et al. [38] describe a three-dimensional analytical model of the melt pool for predicting the shape of the resulting melt pool based on measured and known process parameters. To validate the model, used simulation results were compared to experimental results. In order to compare predications over time, a CMOS camera was used to capture the melt pool geometry during the build process and was later compared to simulations. Furthermore, the as manufactured samples were cross-sectioned and measured using a microscope. Using both 304 Stainless steel and H13 tool steel some insight into how a better model of melt pool geometry could be created were found. The first insight is that convection cannot be ignored in thermal models as it plays a significant role in heat dissipation within the melt pool. Secondly, that the melt pool deforms from several forces acting on it; recoil vapour pressure, thermocapillary force and surface tension which all keep the melt pool from staying a constant shape.

Tang et al. [39] start by developing a simplified model for a CNC based laser disposition additive manufacturing machine that describes the relationship between melt pool temperature and process parameters. The goal of developing this model was to use it in a control strategy to control track geometry which was thought to be dependent on melt pool temperature This model is a first order transfer function which describes the melt pool temperature in terms of scan velocity, laser power and powder flow rate with a single gain and time constant. The gain for the transfer function is determined experimentally. Validation of the model is done by comparing the simulation temperatures to experimental temperatures captured by an unspecified temperature sensor. The model is then used in a control scheme in which melt pool temperature is successfully predicted however, even with temperature being controlled track geometry could not. Similarly to Han et al., it was found that a simplified model for the melt pool cannot ignore heat transfer properties, and that this model is insufficient for controlling track geometry.

In a second study by Tang et al. [40], an attempt was made to develop a model for controlling layer height in a layer by layer scheme. By using three main balance equations for momentum, mass and energy, a model was developed to describe the layer height of the process. The process of using energy balances to develop a model is not a novel idea and has been used by many other research's in both AM and non-AM processes. However, in an in-situ process control, these sets of equations would be computationally intensive. Therefore, between layers this model was used along with temperature data gathered from an unspecified temperature sensor and track height data collected from a laser height sensor to estimate a beam profile path for the subsequent track. In other words, between layers a beam profile path is generated for the subsequent tool path which varies with time based on priori measurements of the existing layer height and in-situ measurements of melt pool temperature as well as the model. Overall this was a novel approach to using accurate models without losing accuracy in the model due to over simplification for minimizing the time constant however, no evidence of model validation was provided.

The model used in the above study is based on a pre-existing model developed by Doumanidis et al.[30] which provides further information into the workings of the model. It is interesting to note that this model was developed for wire feed AM but was applied also to powder disposition suggesting that with knowledge of the process this model could be adapted to powder bed applications. The model used is designed to be employed in a 4x4 multi input multi output control scheme relating outputs; width, height, length and temperature of the melt pool to inputs; thermal power, scan speed/feed rate, material feed rate and the direction of material transfer. These relationships are developed using mass, momentum and energy balances as well as an expression for conduction in the substrate. The control scheme implemented in this study is discussed further below

Existing Models for Powder Beds

As mentioned above there has been limited efforts in the control of powder bed processing. As such, to this research's best efforts, no existing models could be found for SLM/SLS which could be used directly in in a real time controller for the powder bed processes. This being the case a new direction was taken to gather existing FEM models on powder bed process.

Gusarov et al. [41] have provided several of the studies involving the development of models for powder bed additive manufacturing and have expressed several different models for residual stress, thermal properties and geometry for use in FEM. In this study, a model is developed to describe temperature distribution by means of a mathematical model which describes the interaction between the laser and powder bed. The model is used not only to describe temperature distribution in the melt pool but the geometric properties of the melt pool based on thermal radiation and heat transfer. Using this model, the effective radiative properties and heat transfer were found and changes in process parameters allowed for insights into how these properties vary with respect to process parameters. It was found that the particle size, number of pores and solid to liquid fraction of powder are significant factors in determining the effective heat transfer of the powder bed.

Furthermore, it was found that the radiative properties were affected most significantly by powder make up and laser wavelength. Radiative properties, thermal conductivity and consolidation kinetics were described in the model and were validated in several separate studies involving experimental trials. This could be a very useful model for microstructure control due to the emphasis on thermal properties however, it would need to be simplified for use in controls.

Yali Li et al [42] develop a 3D FEM model for simulation of temperature fields in SLM of ALSI10Mg to study the effect of laser power and scan speed on thermal properties during manufacturing. The simulation consists of two models, one for the interaction between the laser and powder bed and another for the laser. The first model is a thermal model which models the effect of conduction, convection and radiation, while taking into account material density, specific heat capacity of powder, thermal conductivity and heat generated in the powder. The second is a model describes the Gaussian distribution of the laser. The simulation results were validated using experimental trials which were done using the same process parameters as were used in the simulation of the model and results were compared. Several important findings came from this study which could be useful for developing process maps for various materials as the thermal gradients and cooling rates were a primary measure for the effects of the process parameters. Findings suggest that laser power had a less significant effect on cooling rate compared to scan speed. The temperature gradient was affected more heavily by laser power.

The travel speed and a similar result in melt pool size when scan speed and laser power were varied. As suspected and noted by several other researchers, as multi-layer tracks were built, more heat was conducted through the existing track. This approach to modelling could be useful for controlling microstructure as it uses thermal gradients and cooling rates as a measure which are key components to the solidification process and microstructure formation.

Luis E. Criales et al. [43] study the sensitivity of IN625 to changes in process parameters using a 2D finite element model. The model created estimates the melt pool geometry from a top view (2D) based on thermal behavior of the melt pool. It was found that variation in the peak temperature in the melt pool can be altered by changing the laser power and the reflectivity of the material. Furthermore, material reflectivity, scan speed, and laser power can significantly affect the melt pool geometry while the laser spot size has a much less significant effect. It should be noted however that convection and radiation have both been ignored in this model, which is contradictory to existing research, that proposes that radiation is as a key element for an accurate model. Furthermore, the model validation was done by comparing simulated results to simulated results of studies conducted by other researchers, which may affect the validity of the model and therefore, the results.

Another key model exists which have been used to try and characterize the outcome of powder bed manufacturing. This model is known as energy density and has been used to try and describe in microstructure, mechanical properties and porosities and is common only used in the field, cited are 3 examples of its use[44][45][46].

Table 6: Summary of Modelling Approaches

Study	Material & Purpose	Validation	Conclusions AM Type
[47]	Ti AL6 V Use system ID to characterize laser power's effect on melt pool size by inputting sin waves into the laser and analyzing the result output of a CMOS camera whose signal is correlated to melt pool size. Using a Fourier transform and fitting curves to the data a second order model was fitted to describe the size of the met pool based on laser power.	CMOS 8-bit grey scale used to validate melt pool size prediction	• By using System identification and controlled experiments an accurate model of how laser power effects melt pool area was acquired • Custom Built Powder Bed laser melting
[48]	303L Stainless Develop a first order model which describes the desired track height based on beam diameter, scan velocity, powder jet diameter, projected plane size of powder flow and serval constants which are determined using experimental data and a least squares regression technique	Model was validated through simulation only; a full controller was validated with experiments	• The model was successfully used in an SMC controller with PID to control clad height • Model constants are varied based on process parameters • Laser Deposition
[49]	Polycarbonate A model is built to simulate the phase	Compared to existing	• By coupling an equation for laser interactions and heat transfer, a successful

	transformation occurring in the melt pool. The model includes 3 main components; interaction between laser and bed, heat transfer in both powder bed and previously formed part and the phase transformation from powder to part.	models in other literature	model was built to model the temperature distribution in the powder bed • SLS
[50]	To develop a model to express radiation transfer to study the effect of radiation heat transfer in powder beds	Comparison between model and experimental results was used to validate the model.	• "the absorptance of a powder bed with large optical thickness is a universal function of the absorptivity of the solid phase and independent of the morphology of the powder particles and the porosity" • Powder bed laser processing
[51]	IN625 Manufacture test coupons of IN625 to test mechanical properties and microstructure under varying process parameters, such as scan speed, laser power and scan strategy.	Mechanical property testing (Fatigue and tensile testing), Part Density Testing, Standard metallographic specimen preparation methods	• No conclusions are drawn, however lots of useful information on variance of microstructure from parameter changes is available. • IN625

Control Strategies

Overall, a very limited amount of work has been done into monitoring and controlling selective laser melting and sintering processes and of the noted work, the documentation on the actual control scheme is very limited. As such, a review of control schemes used in AM is provided rather than just for powder bed applications. The majority of available literature focuses on controlling deposition or cladding processes, which can have a large crossover into powder bed control due to the fact that they are both “thermally dominant processes […] and temperature distributions and history are critical to the process characteristics and performance”[50] and have for the most part the same input variables and output variables.

Clijsters et al. [52] employ a monitoring system and algorithm to predict part quality in real time. Although nothing is done with this information to correct the process and thus no control is implemented, it is the closest to a control strategy that could be found for SLM/SLS with documentation regarding the control strategy. The purpose of this study was to develop an in-situ monitoring system which could predict melt pool variation that resulted in pores in the part. This was accomplished by using two optical sensors (Near IR camera and CMOS camera) which capture images of the build process. The wavelength of these cameras was carefully selected to capture clear images of the process. These images are sent to a field programmable gate array which is used to collect images at a rate of 10 kHz which helps overcome time constant issues with traditional image process hardware. The quality of the part was sensed by translating these captured images from the time domain to the position domain, using an algorithm to check for defects. Specifically, the algorithm detected deviation in melt pool intensity and melt pool area (length and width). Although this is not implemented in a feedback controller, the technique used for capturing and analysing data would be a good application for a closed loop controller.

The purpose of a study conducted by Farshidianfar et al. [28] was to control microstructure in a CNC based deposition machine by controlling the melt pool cooling rate in-situ. This was achieved by using an IR camera as a feedback system in a PID controller. The IR camera captured images of the melt pool in real time. An algorithm translated pixel colour over time into cooling rate and developed thermal maps of the melt pool. This information was then used to adjust the travel speed of the CNC table to control the cooling rate. Travel speed was selected as the control input due to experiments conducted that showed that travel speed has the greatest impact on the cooling rate and thermal gradients and thus the greatest effect on the resulting microstructure. An interesting note about this study was that the IR camera used was calibrated for a single average emissivity. This would affect the accuracy of the temperature reading due to the fact the emissivity of the melt pool changes over time due to temperature change and oxides on the surface. This would have less of an effect on cooling rates because it looks at the change in temperature rather than the actual temperature, although it would still affect the measurement. Overall this control strategy had promising results; showing that at two different set points for cooling rate, the microstructure was uniform, even when both set points were established in the same track. However, there may be room for improvement if a priori knowledge of the melt pool emissivity was known to make real time changes of emissivity based on desired peak temperature in the melt pool.

Devesse et al. [29] develop a higher order model for description of thermal dynamics in the melt pool. Their model predicts the growth of the melt pool based on temperature. The goal of the controller is to use temperature feedback to control the width of the melt pool by varying laser power. To do this, a hyperspectral system is used to gather temperature data of the melt pool. The camera has a very high spectral and spatial resolution of 0.8nm/pixel and 11.6um/pixel respectively. As with any contactless temperature measurements, emissivity is an issue, as seen in several studies presented in this paper. To overcome this, an approach was used to characterize the emissivity offline for many wavelengths and temperatures; generating a table or map of the results. This map would later be used to pick the correct temperature based on deviations in wavelengths, overcoming the emissivity issue almost entirely. This controller was not implemented in an actual machine but instead was partially simulated. The physical camera captured images on a computer screen of a simulation of the process which allowed for very confident validation of the sensors and temperature algorithms. The purpose of this was to allow for a generalized controller which could be applied to any form of AM. With some adaptation to account for the thermal dynamics of the powder bed, this model and controller set up is favourable in a closed loop controller for microstructure.

A control system designed by Fathi et al. [48] incorporates a PID controller with a feed forward loop in order to control the clad height of a deposition AM process through the adjustment of scan velocity. The parametric model for this controller is based on two separate models; one which describes the linear, transient response of the system and the other that describes the non-linear, steady state portion of the system. The model developed is a first order model which describes the desired track height based on beam diameter, scan velocity, powder jet diameter, projected plane size of powder flow and serval constants which are determined using experimental data and a least squares regression technique. This parametric model of the system which describes the clad height during the build process is used for the feedforward portion of the controller. However, since the desired clad height is not an input variable to the system, it must be translated into an input variable. In this strategy, scan velocity is used as the input variable and can be determined as the inverse of the parametric model. This inverse relationship between track height and scan velocity was determined from experimental trials which showed that track height changes inversely with scan velocity. For example, as scan velocity in was increased, track height decreased and vice versa. With a desired set point for track height, the feedforward model provides the input for the necessary scan velocity to the system. The error of the model is determined by a feedback loop measuring the actual clad height output and comparing to the commanded track height. To correct for error in the feed forward loop a PID controller is integrated with a memoryless block. The memoryless block is again an inverse block to change error of position into error of scan velocity and is added to the feed forward loop to correct for any errors in the model. To determine the gains for the PID controller, experimental trials were run to find the best results. Experimental results show that accurate trajectory tracking of track height was achieved when a sinusoidal input for track height is given as the command signal. When comparing the controller with and without the feed forward loop a noticeably better result in trajectory tracking was achieved with the feed forward loop. This suggests that a feedforward loop could be linked to better melt pool geometry control, which is a key factor in controlling microstructure of the AM process.

The goal of the controller designed by Doumanidis et al [30] is to control the geometry of the melt pool by varying process parameters; thermal power, scan speed/feed rate, material feed rate and the direction of material transfer. The controller uses a unique method for capturing part geometry in-situ for feedback. In many ways, it is similar to other works in the fact that a CCD camera is used to capture 8 bit images of the geometry, where it differs is how it does this, rather than take a picture of the melt pool or of the part, it takes a picture of a laser which is shone on the freshly built layers just behind the melt pool. The CCD captures images of the laser reflection and is able to extrapolate track height data using an image processing algorithm. To overcome the brightness of the melt pool interfering with the laser light, a physical curtain separates the melt pool from the laser. For further feedback, a pyrometric camera is used to capture images of the melt pool in real time in order to derive the temperature distribution of the melt pool. Unlike so many studies that fail to mention how emissivity is overcome for extrapolating melt pool temperature, Doumanidis et al. adjust the emissivity in real time based on emissivity identification techniques developed prior to identify emissivity based on melt pool size.

The model used, as mentioned in the model review section, is a Multi-Input Multi-Output (MIMO) model. What is not mentioned, is the model's need to calculate the material transfer and thermal troch efficiencies associated with the equations. This could be done offline by manufacturing samples but may not work well in the fabrication of real components due to the changes in shapes of parts being manufactured compared to samples. Alternatively, a map of necessary constants could be produced offline as reference base for the geometry being manufactured however, that is time extensive and not adaptable. Therefore, in the control loop a parameter estimation is to be made for the model efficiencies which is done by using the error of the controller and the above-mentioned feedback of melt pool temperature and geometry. Ideally, the controller would optimize all input parameters for controlling the melt pool geometry based on error but would be computationally intensive, and therefore only use scan velocity, making the controller strategy closer to traditional single input single out system.

Error is estimated by comparing the model generated geometry of the melt pool for along with in-situ geometry measurements to the desired geometry. However, as mentioned, the geometry measurement occurs behind the melt pool, which causes a large delay that in turn, causes the error to be large as the comparison would be desired temperature at time 0 compared to time -feedback delay. To overcome this delay, a prediction strategy (Smith predictor) is employed which uses the delayed data from the model and feedback loop to predict the shape of the track being laid at time 0. With real time predictions of melt pool geometry as the feedback mechanism, error can then be calculated. Lastly, a PI controller is used to control the process input scan velocity going back into the system. The controller is validated experimentally. This approach to controlling the process has some valuable take away moving forward; the biggest of which is that time delayed sensor input can be overcome with a good control strategy for AM and that an overly complex model can lead to computational time issues.

Some other studies to have implemented closed loop controls in powder bed and powder deposition systems however a lack of documentation on the control strategy used makes it very difficult to extract valuable information regarding the specific control structure. D. Hu et al [53] describe a controller which uses a NIR imaging system for feedback in order to control the melt pool geometry and subsequently the thermal gradients and cooling rates and thus the resulting microstructure and mechanical properties. In that study, a simulation of the controller is compared to experimental data in order to validate the controller model. Mireles et al.[54] develop a controller for powder bed applications which uses an IR camera for imaging and uses LabView to control the actual AM system. A general control strategy Is provided where images are collected from the IR camera and analyzed using an imaging process system to decide on new parameters. However, this image processing takes 10 s and therefore no real-time controller is possible. Craeghs et al. [52] also develop a control system for powder bed systems which also uses a photodiode sensor for feedback combined with a second order system describing the thermal process occurring during the build. A PI controller is designed to alter laser power to control melt pool geometry however, once again, no description of the control strategy is available. Tang et al [39][40] provide more information on their control scheme for maintaining melt pool temperature and a block diagram is given showing a feedforward controller and a Kalman filter for filtering extremely noisy temperature sensor feedback data. However, no additional information is provided into the feedforward portion of the controller or other inputs in the block diagram. A fair amount of experimental data is available from this controller and shows that the controller can control temperature tracking well, aligning with Fathi er al. [48] that a feedforward loop has value in AM control systems.

Summary

Overall a fair amount of work has gone into the development of control systems for AM. Many sensors have been used to capture a wide range of data such as melt pool temperature, track height, melt pool geometry and radiation intensity [19-33, 43-48]. These sensors have been implemented in many different forms; on both lab built and commercially available AM systems and show great promise for monitoring powder bed processes in real time. However, this review shows that there is a lack of research directly related to the modeling and controlling powder bed processes. Although a great deal of modelling has been done for controlling deposition processes [33,34,35,37,38], most modelling for powder beds has been done for simulations and FEM's [39-44], which can be translated into control models, but this has only been done by a handful of researchers. This can also be seen in the closed loop controls which have been used in AM, in which the majority have been designed for use in powder deposition [46, 38, 48] or created for general use for any system [47] but few have been developed for powder bed [36, 49]. Lastly, researchers have gathered priori measurements for the IN625 microstructure [12, 13] but no useful process map has been generated, although techniques for generating these maps have been developed [6-11, 14-18]. This leaves a gap in the research, not only in real time microstructure control of IN625 and Invar 36 but also, more broadly and reveals the need to develop models, sensing and control strategies for powder bed systems.

Chapter 2: Sensors: Selection, Calibration and Implementation

In this chapter sensors are explored calibrated and implemented. Both contact and non-contact thermal measurements sensors are explored in detail before a selection is made. After which the chosen sensors are calibrated and implemented. The first step was to more closely define the requirements of the sensors and is done below. Before any work can be done on monitoring it is critical to define the system to be monitored. The system inputs and outputs need to be selected based on both the literature review and the specific SLM machine used and what process parameters can be changed online. For this system (the Omnisint 160) many input variables can be fixed to help make the choice of input variables easier. Based on the machine being used, laser power is the only variable that can be changed for both layer to layer control and within each layer. Additionally, the literature review showed that laser power also affected the temperature of the system. Therefore, the output of the system will be simplified to peak melt pool temperature. The system shown in Figure 5 shows the input and output of the system as well as the system or plant itself.

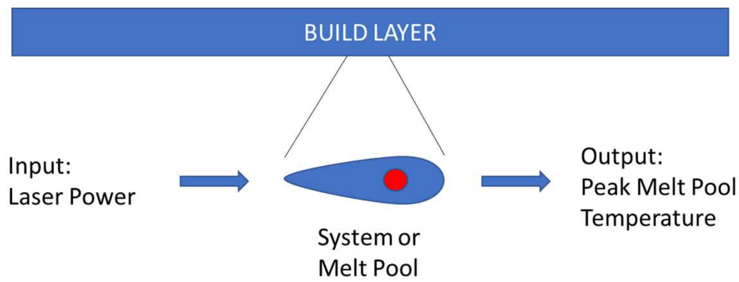

Figure 5: System Definition

However, this block diagram does not have a detailed system definition. Although it is desired to measure the temperature of the system there are many ways with which that could be done. The temperature of the surrounding area could be monitored or the temperature of the entire part or the temperature of a specific area or even just the melt pool as it moves. As the goal of the monitoring system is to help improve the part quality of SLM manufactured components it makes sense to explore the temperature of the part itself, which can be narrowed to two possible temperatures to monitor. The first is the temperature of the melt pool (single point peak temperature) and the second is the temperature profiles of the entire part (Full Build). Both of which have advantages and disadvantages shown in Table 7. The goal of the sensor selection process is to be able to monitor both. With the system more closely defined the sensor requirements were laid out in the following section.

Table 7: Summary of system definition

System Type:	**Advantages**	**Disadvantages**

Single point peak temperature	Easy to implement	Only one point of the path is considered rather than the entire build
Full Build	Can monitor the temperature entire build entire process including residual heat Encompasses measuring the moving melt pool	Requires a Camera Due to the scan speed the camera would need to be fast (1Khz or up) Due to melt pool size the resolution would need to be very high.

Sensor Requirements

There are several requirements for the selection of sensors for measuring the melt pool temperature. Factors such as the speed of the laser, the size of the melt pool, the temperature range of the process, environment (powder bed), as well as the solidification rate must be considered. The following 4 requirements have been laid out based on these factors and are the most significant when selecting the sensor.

1. **Speed of the melt pool (Scan Speed):** The scanning speed of the laser is proportional to the speed the melt pool is travelling. Therefore, the sensor used needs to consider that the object being measured i.e. the melt pool moves and therefore must, either move with the melt pool or have the capability to monitor temperature across a large area in order the capture the temperature of the melt pool for the entire build process. Alternatively, a single point could be measured.
2. **Size of object being measured (Melt Pool Size)**: The size of a melt pool ranges from a few μm to several hundred μm in width. Therefore, the sensor requires good resolution across the area being monitored in order to capture the temperature of the small melt pool.

3. **Temperature range:** Temperatures in additive manufacturing estimated to range from 800°C to 2000°C for various materials.
4. **Environment (effects of the powder bed):** Due to the nature of SLM there is a powder bed and a recoater blade which does not allow sensors to be mounted directly on the build plate as it would interfere with the recoating process but does allow sensors to be mounted beneath or above the build plate.

Temperature Measurement Systems

In order to select a sensor a study of the current technologies was completed. The most widely used temperature measurement sensors are RTD's, thermocouples and thermistors. All three devices make use of material properties to create a sensor that either generates small amounts of current or changes its resistance with changes in heat. Thermal imaging and pyrometers are also commonly used digital sensors which use photodiodes to measure radiation and infer the temperature based on the radiation's intensity. The following table categorizes these sensors into two sub categories, Contact and Non-Contact sensors, meaning sensors which need to touch the object they are measuring and sensors which do not. From this division we can compare advantages and disadvantages both across and within each category.

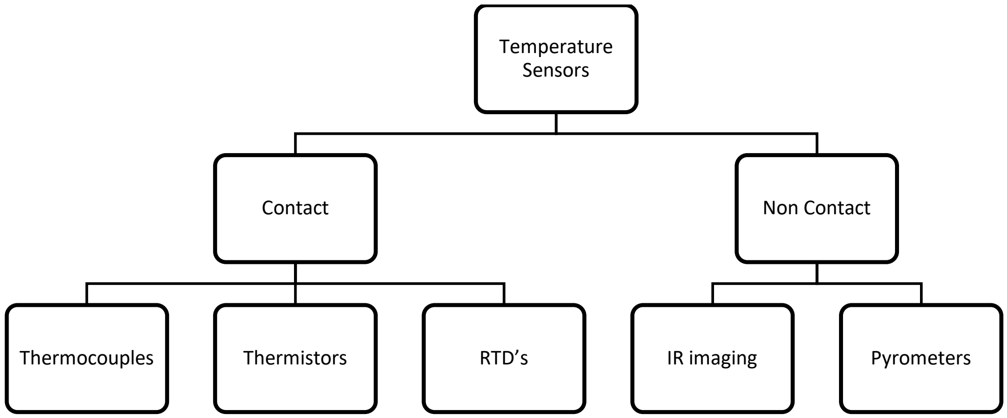

Figure 6: Temperature Sensor

Comparing Contact and Non-Contact sensors there are many advantages and disadvantages of either type. Qualitatively thermistors, RTDs and thermocouples have many advantages over pyrometers and IR Imaging, they are more easily available, significantly cheaper, simple, reliable but must be in contact with the object being measured. While pyrometers and IR imaging have the significant advantage of being non-contact, both are very expensive and difficult to calibrate. In the selection process it is also necessary to look at the technical specifications of each sensor which is explored in detail below.

Contact sensors

Table 8 summarizes the critical characteristics needed to meet the sensor requirements set out earlier in this chapter. All three contact sensors are explored (Thermistor, RTD and Thermocouple) are relatively low cost and have an acceptable level of accuracy. However, the temperature range of each sensor clearly shows that only RTD's and thermocouples have a sufficient temperature range to measure molten metals. However, RTD's do not measure a high enough temperature for IN625 and have extremely slow response times for this application. Therefore, thermocouples are the only choice for the contact sensors explored and a specific sensor is selected later in the chapter.

Table 8: Contact Sensors - Technical Specifications

Specification	**Thermistor**	**RTD**	**Thermocouple**
Temperature Range	-100 to 500°C	-200 to 1000°C	-250 to 1750°C
Accuracy	0.05 to 1.5°C	0.1 to 1°C	0.5 to 5°C
Response time	Fast 0.12 to 10s	Slow 1 to 50s	Fast 0.10 to 10s
Cost (Relative)	Low	Low	Low

Non-Contact Sensors

Examining the contactless sensors both pyrometers and thermal imaging meet the technical requirements to overcome all the considerations with sufficient temperature range, response times and accuracy as shown in Table 9 .

Table 9: Contactless Sensors - Technical Specification

Specification	**Thermal Imaging**	**Pyrometer**
Temperature Range (typical)	-80 to 3000°C	0 to 3200°C
Accuracy (typical)	0.05 to 1.5°C	0.1 to 1°C
Response time	Fast 0.01-0.25s	Fast 0.002-0.012s
Cost (Relative)	Very High	High

Where the two sensors differ is in the way they "look" at objects. Although both sensors use photodiodes to collect emitted radiation and both do not require to be in contact with the object, each sensor has a unique and specific field of view (FOV) with separate requirements for what can be in that FOV. That is to say the there is a certain area in which the sensors can measure the temperature and have different requirements for how much of that area (i.e FOV) need to be occupied by the object being measured. The pyrometer has a smaller field of few and more stringent requirements to how much of that field of view needs to be occupied by the object being measured (typically around 15% or greater). Thermal imagers have no real constraint on the FOV if the sensor is big enough (i.e small enough pixels to capture detail) and has no requirements for how much of the FOV needs to be occupied. Both sensors were chosen for this research and the selection of each is shown below.

Sensor Selection

Thermocouple selection

Based on the sensor requirements there are only two thermocouples which have the necessary temperature range, the B and C type thermocouples as shown in Figure 7. Even though a C type would be more desirable then a B type (due to its larger temperature range) they are significantly more expensive. As it was unknown whether or not the thermocouples would work for the process a B type was chosen due its price point and accessibility.

TOLERANCE OF THERMOCOUPLES

ANSI/ASTM	°C			°F		
	Temperature Range	Standard	Special	Temperature Range	Standard	Special
T	-200° to -67°	± 1.5% T	± 0.8% T*	-328° to -88°	± 1.5% (T – 32)	± 0.8% (T – 32)*
	-67° to -62°	± 1°	± 0.8% T*	-88° to -80°	± 1.8°	± 0.8% (T – 32)*
	-62° to 125°	± 1°	± 0.5°	-80° to 257°	± 1.8°	± 0.9° *
	125° to 133°	± 1°	± 0.4% T	257° to 272°	± 1.8°	± 0.4% (T – 32)
	133° to 370°	± 0.75% T	± 0.4% T	272° to 700°	± 0.75% (T – 32)	± 0.4% (T – 32)
J	0° to 275°	± 2.2°	± 1.1°	32° to 527°	± 3.96°	± 1.98°
	275° to 293°	± 2.2°	± 0.4% T	527° to 560°	± 3.96°	± 0.4% (T – 32)
	293° to 760°	± 0.75% T	± 0.4% T	560° to 1400°	± 0.75% (T – 32)	± 0.4% (T – 32)
E	-200° to -170°	± 1% T	± 1°*	-328° to -274°	± 1% (T – 32)	± 1.8°*
	-170° to 250°	± 1.7°	± 1°*	-274° to 482°	± 3.06°	± 1.8°*
	250° to 340°	± 1.7°	± 0.4% T	482° to 644°	± 3.06°	± 0.4% (T – 32)
	340° to 870°	± 0.5% T	± 0.4% T	644° to 1600°	± 0.5% (T – 32)	± 0.4% (T – 32)
K	-200° to -110°	± 2% T	—	-328° to -166°	± 2% (T – 32)	—
	-100° to 0°	± 2.2°	—	-166° to 32°	± 3.96°	—
	0° to 275°	± 2.2°	± 1.1°	32° to 527°	± 3.96°	± 1.98°
	275° to 293°	± 2.2°	± 0.4% T	527° to 560°	± 3.96°	± 0.4% (T – 32)
	293° to 1260°	± 0.75% T	± 0.4% T	560° to 2300°	± 0.75% (T – 32)	± 0.4% (T – 32)
N	0° to 275°	± 2.2°	± 1.1°	32° to 527°	± 3.96°	± 1.98°
	275° to 293°	± 2.2°	± 0.4% T	527° to 560°	± 3.96°	± 0.4% (T – 32)
	293° to 1250°	± 0.75% T	± 0.4% T	560° to 2300°	± 0.75% (T – 32)	± 0.4% (T – 32)
R or S	0° to 1260°	± 1.5°	± 0.6°	32° to 1112°	± 2.7°	± 1.08°
	1260° to 1480°	± 0.25% T	± 0.1% T	1112° to 2700°	± 0.25% (T – 32)	± 0.1% (T – 32)
B	870° to 1700°	± 0.5% T	± 0.25%	1600° to 3100°	± 0.5% (T – 32)	± 0.25% (T – 32)
C**	0° to 426°	± 4.4°	—	32° to 800°	± 8°	—
	426° to 2315°	± 1% T	—	800° to 4200°	± 1% (T – 32)	—

Figure 7: Tolerance and Types of Common Thermocouples [55]

Pyrometer selection

Two main types of pyrometers exist, one colour and two colour. The difference between them is that a one colour pyrometer measures temperature at one wavelength while two colour measures at two wave lengths. This allows the colour pyrometers (once calibrated) to create a ratio between the two wave lengths which can make corrections in temperature measurement while obstructions such as dust, scale or changes in emissivity are present, where a one colour pyrometer cannot [56]. Additionally, a two colour pyrometer does not need its FOV completely filled by the object (object being measured area < FOV area) where a single colour does needs its FOV completely filled. Therefore, a two colour pyrometer cable of measuring more then 1800°C with a fast response rate was needed. A Fluke Endurance pyrometer was chosen, and its technical specifications are listed below.

Table 10: Fluke Endurance Technical Specifications

Parameter	**Value**
Response time (90%)	2ms
Temperature Range	1000°C - 3200°C
Repeatability	+/- 1C
Optical Resolution	65:1

Thermal Camera selection

Choosing a thermal camera requires the consideration of a few different elements of the camera. The resolution, temperature range, and frame rate are the most critical of these elements. The temperature range should be able to handle temperatures above 1800°C in order to capture the melt pool of IN625 and other materials. The resolution must be high enough to resolve the melt pool from the images captured and the frame rate must be high enough to capture the fast-moving laser. A list of commercial IR imagers was gathered and gone over to see the best option. The thermal camera with the best resolution, temperature range and FOV was chosen that also fit the budget. The camera selected was an Optris PI 08M with a focal length of 25mm and its properties are shown in

Table 11.

Table 11: Optris P1 08M Specifications

Temperature Range	575°C - 1900 °C
Resolution	764 x 480
Frame Rate	1 kHz
Pixel Size(at 200mm)	0.12 mm

Calibration

Thermocouple Calibration

Calibration of the thermocouple was a straight forward process. The thermocouple was placed in a furnace which had a known temperature. Using the same DAQ and wires that would be used in practise were also used in the calibration process. With the thermocouple placed in the oven a correction value was made in the DAQ software. For this calibration a temperature of 1345°C was used as it is the melting point of IN625.

Pyrometer Calibration

Before using a contactless temperature measurement system such as a pyrometer, it is necessary to know some properties of the material you are measuring, specifically, how that material emits radiation, otherwise known as its emissivity. In the case of a two-colour pyrometer it is necessary to adjust the emissivity slope of the device (the emissivity at two wavelengths) for every material. The most effective way to determine and adjust the slope is to take the temperature of the material using a probe sensor such as an RTD, thermocouple, or other suitable method. Once you determine the actual temperature with that probe, adjustments can be made to the slope setting until the sensor's temperature reads the same as the actual temperature reading. To accomplish this for IN625, a vacuum induction furnace with an argon environment was used to heat the sample of IN625 powder. This is a very suitable environment because it represents a proxy to the SLM machine in which the sensor will be used. In total three trials were run of this experiment resulting in a slope of 0.960. The experiment to calibrate is outlined below.

Materials and apparatus

- Vacuum induction furnace with argon environment (Capable of greater than 1400°C)
- 1 Alumina & 1 graphite crucible
- Two-colour pyrometer (Fluke Endurance)
- B Type thermocouple (Safe to 1800C)
- Data Acquisition device
- Refractory insulation and blocks
- IN625 powder

Procedure:

1. Calibrate the thermocouple using the same DAQ, channel and wires that will be used to measure in the induction furnace. This can be done by measuring known temperatures and insuring the thermocouple is reading correctly. **Note:** Only done in second trial
2. Set up of the induction furnace: connect power supply, cooling lines and vacuum pump and check for any leaks in all lines Shown in Figure 8.
3. Connect induction coil and prepare furnace charge (placed the powder in the alumina crucible, which goes inside the graphite crucible and is wrapped in refractory insulation). This can be seen in Figure 9

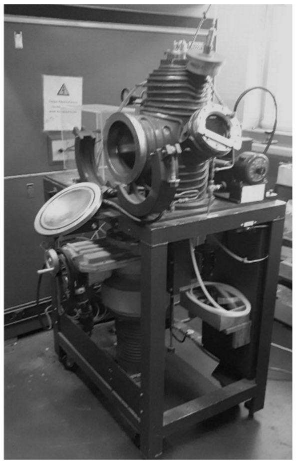

Figure 8: Vacuum Induction Furnace

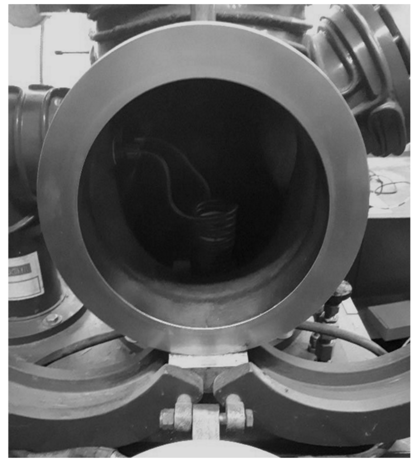

Figure 9 The crucibles and insulation

4. Set up sensors
    a. The thermocouple is positioned in the middle of the furnace and is connected with a vacuum seal at the top of the furnace. It is lowered and raised using a torr fitting and can be seen in Figure 11
    b. The pyrometer is positioned in a viewing port of the furnace and is focused on the crucible (Figure 10)

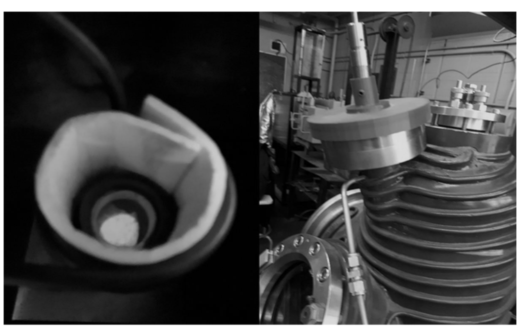

Figure 10(a) The pyrometer spot in crucible (b) The pyrometer mount

Figure 11: Thermocouple configuration

5. Oxygen is to be removed from the furnace by pulling a strong vacuum and slowly allowing argon to fill the chamber. This is repeated several times (3-5) to take out as much oxygen as possible.
6. The current is slowly turned up in the induction coils until the charge is completely melted and the furnace has reached a maximum temperature (i.e maximum current)
7. The charge is left at this temperature for 20 minutes to reach steady state (the change in temperature can be monitored with the pyrometer, although not an accurate temperature value it can still show whether the temperature is changing)
8. The thermocouple is lowered into the charge **Note:** this was only done in the first trial in the second trial it was left in the crucible
9. The furnace is turned off and the emissivity slope is changed on the pyrometer until the thermocouple and pyrometer are reading the same value
10. This is repeated until a value shows the correct temperature on the pyrometer
11. A final set of testing is done to collect error information and is compared to the pyrometer results. This was done in a third trial.

Results of Calibration

In the first trial in which a 10 mL crucible was used filled with IN625 powder, the slope was found to be 1.06. The results of this trial can be seen in Figure 12: Trial 1 Calibration Curve in which readings from the pyrometer and thermocouple are shown. It is clear from this figure that the readings from the pyrometer and the thermocouple are the same at the tail end of the plot. This was accomplished by adjusting the pyrometer slope well recording measurements from both the thermocouple and pyrometer at the same time and changing the slope on the software. However, in this trial the thermocouple was not heated with the sample but was inserted into the crucible once the furnace was turned off as was noted in the procedure.

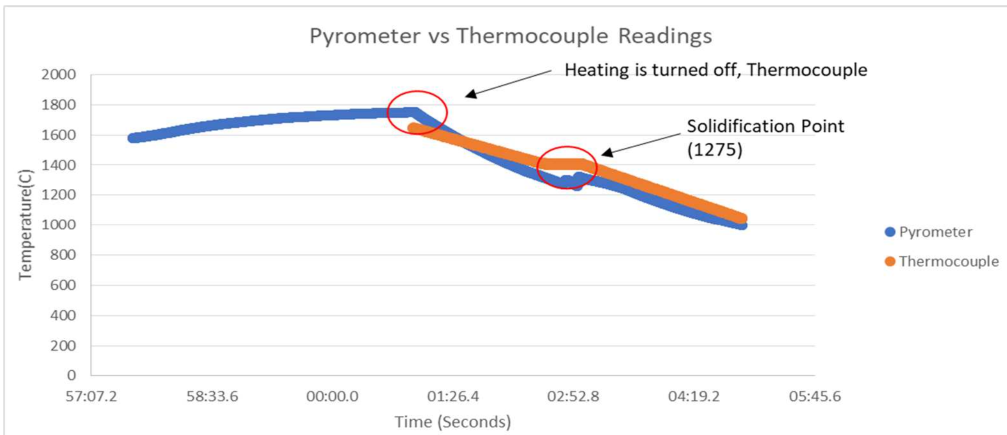

Figure 12: Trial 1 Calibration Curve

Although the results from the first trial were promising there were some errors in the experiment which were realized after.

1. As mentioned above the thermocouple did not have time to reach a steady state temperature as the cooling happens very rapidly.
2. The thermocouple takes up almost 36.6% of the crucible volume which will absorb a lot of the heat in the molten Inconel once inserted into the crucible
3. The thermocouple takes up some of the field of view (FOV) of the pyrometer (Figure 11*:* Thermocouple configuration). Although the

pyrometer only needs 15% of its FOV occupied by its target it is better the have the entire FOV filled by the object being measured [57]

4. The thermocouple was not calibrated with the DAQ system

Each of these errors was eliminated in the second trial and shown below is the method to eliminate each error.

1. To avoid any issues with the thermocouple reaching steady state it was inserted into the crucible while it was brought up to temperature and allowed to heat up with the sample. In this way the thermocouple was at the same temperature as the IN625 powder once calibration started.
2. The crucible size was increased from 10 mL to 100 mL allowing the thermocouple to take up only 17% of the volume shown below

Figure 13: 10 mL crucible (left), 100mL crucible (right)

10 mL	100 mL
Inside Diameter: 26 mm $Percent\ of\ TC$ $= \frac{Diameter\ TC}{Crucibile\ ID} X100\%$ $= \frac{9.525mm}{26mm} x100\%$ $= 36.6\%$	Inside diameter: 56 mm $Percent\ of\ TC = 17\%$

3. To improve on the experiment, it was desired to have 100% of the FOV of the pyrometer occupied by the target and not the thermocouple. This was accomplished with the increased crucible size and can be seen in Figure 14 (left) 100 mL (right) 10 mL

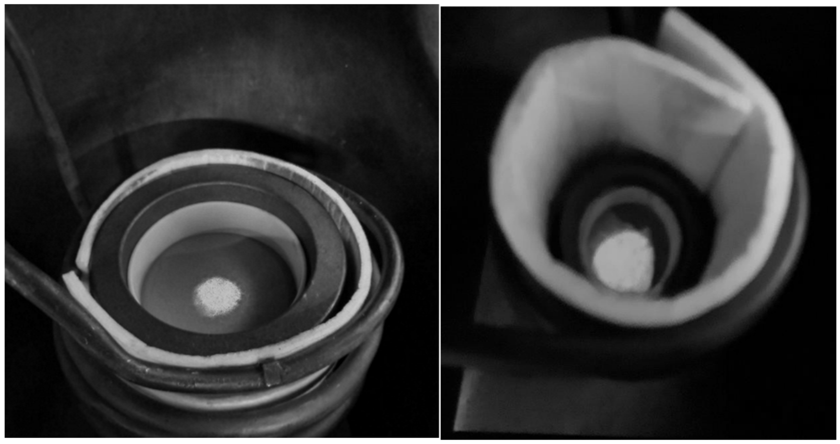

Figure 14 (left) 100 mL (right) 10 mL

4. The thermocouple was calibrated using the same leads, DAQ and channel in an electric furnace in which the temperature was known.

With these measures (1-4) put in place the errors of the first trial were over come and a second trial was run and is shown below. Furthermore, the procedure was lengthened to repeat the process multiple times to help hone in an accurate slope. Initially the slope was adjusted in large increments until the thermocouple and pyrometer were in rough agreement, after which the slope was adjusted in small amounts in subsequent cooling cycles until the thermocouple and pyrometer were reading the same temperature.

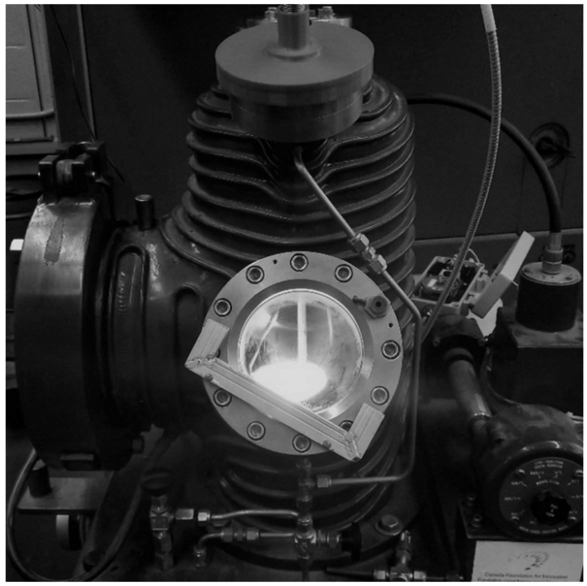

Figure 15 Trial 2 – Melting Inconel 625

The final trial is shown below (Slope = 0.960). The noise at the beginning of the plot in the thermocouple is caused by the Eddie currents induced by the induction coil on the thin thermocouple leads, as soon as the current is reduced to zero the signal is noise free. In this figure there is a strong agreement between the pyrometer and thermocouple temperature measurements.

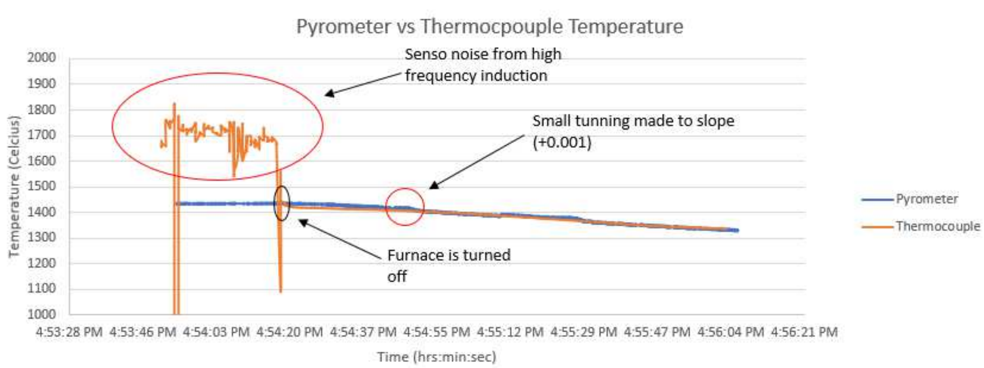

Figure 9: Trial 2 Calibration Curve

Lastly, an additional set trials was run with emissivity slopes at 0.950, 0.960 and 0.970 to ensure the accuracy of the testing. The data from the thermocouple and each trial was compared to find out the average temperature error, max temperature error and standard deviation.

Table 12: Calibration Results for Inconel 625

Pyrometer Slope	**Average Temperature Error** (°C)	**Max Temperature Error** (°C)	**Standard Deviation** (°C)
0.960	4.39	8.48	2.09
0.970	5.93	9.63	2.46
0.950	4.68	14.58	3.11

It is clear from Table 12 that the slope of 0.960 is the best choice as a slightly higher slope of 0.970 and lower slope of 0.950 increase the average error by 1.54°C and 0.29°Cs respectively, the max temperature error by 1.15°C and 6.1 °C and standard deviation by 0.37°C and 1.02°C respectively.

After learning from this set of experiments, two additional trials were run using one colour mode on the pyrometer. It was found that at the peak temperature of 1425 C the emissivity which resulted in the best fit was 0.35.

Summary of Pyrometer Experiments

In conclusion the second trial yielded very strong results and overcame all the errors of the first trial. A slope for the pyrometer was found to be 0.960 for IN625 and was verified in a third trial, a sample of that data can be seen in Figure 16**.** One of the limitations of the second experiment was the fact that a maximum temperature of only 1450C was reached. This was due to the fact the charge in the furnace was much larger and the induction coil used had less coils and were more spaced apart compared to the first trial. IF it were to be repeated a larger more powerful furnace could be used to reach higher temperatures and to have a larger charge. Furthermore, if a single colour pyrometer mode is to be used an emissivity of 0.35 is approximate to capture the peak temperature at a wave length of a nominal 1.0 um.

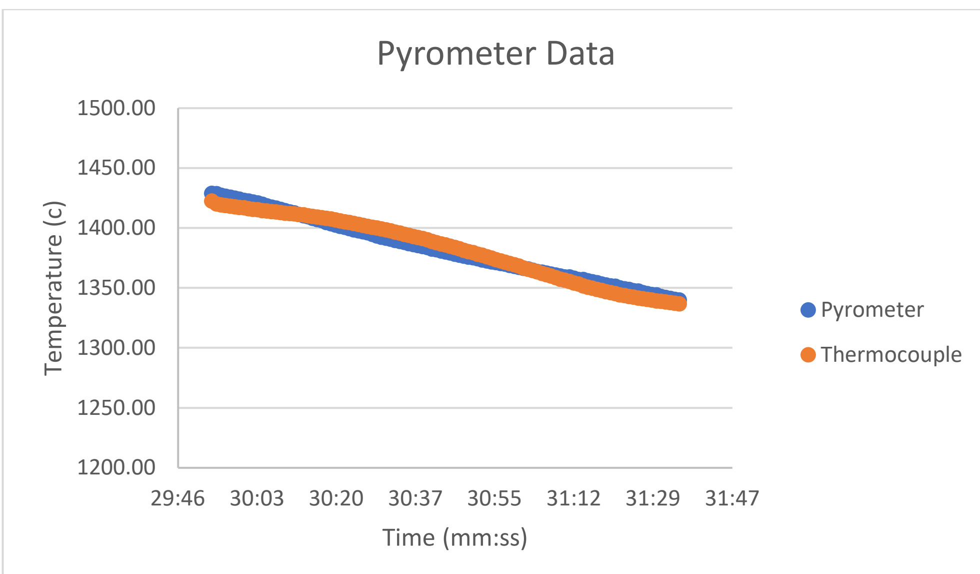

Figure 16: Temperature Data from Pyrometer Calibration 1

Camera Calibration

Calibration of the thermal camera was done within the 3D printer (Omnisint 160). The calibrated pyrometer was used as a reference point to make adjustments in the thermal camera software (PIX Connect) until the thermal camera and pyrometer read the same temperature. The parameters adjusted were the emissivity and transmissivity. Emissivity was fixed at 0.2 [58] while the transmissivity was adjusted as it was unknown due to the atmosphere of the build chamber.

The calibration process was done over 5 trials on the printer (process parameters in Table 13). In each trial the Transmissivity was adjusted and the average peak temperature of the first laser pass was monitored until the value was reading the same average as the pyrometer. This process happened in-situ for each layer. After ten layers this process was repeated. In total the process was repeated 5 times to hone in the calibration.

Table 13: Process parameters for Calibration

Process Parameter	**Value**
Scan Speed	200 mm/s
Contour Passes	0
Hatch Spacing	0.1 mm
Layer Thickness	0.04 mm
Beam Diameter	0.09 mm
Laser Power	300 Watts

Implementation of sensors

Thermocouples:

To implement the thermocouples first a concept needed to be made where by the thermocouples could come close to the surface of the build plate without touching the build surface as to not interfere with the build process. Secondly the thermocouples leads could not be on the build plate surface as they would interfere with the recoater. Thirdly there is no way on the SLM machine being used to modify the build area or to have leads coming out of the machine. Therefore, it was necessary to design a self-contained system. The last consideration was how to measure across the build area, because thermocouples can only measure a single point, many thermocouples would be needed to monitor the entire build plate. In Figure 17 the initial concept for this system is mapped out in which a data logger, battery and multiple thermal couples are mounted below the build plate and are contained in a cylinder, with the thermocouples mounted through the bottom of the build plate close to the surface and the logger and battery remaining in the cylinder.

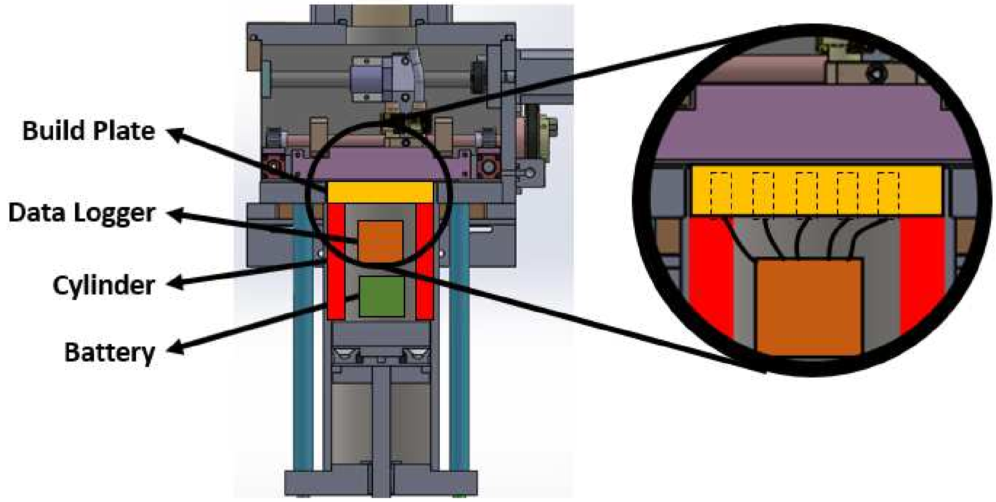

Figure 17: Thermocouple Installation Concept

With the concept of how to implement the sensors figured out it was then necessary to find an engineering solution to make this concept a reality. Referencing a paper by Segerstark et al. [22]. it was found that the thermocouple should be around 0.2mm from the surface of the build plate. 0.2 mm is a very tight requirement as it creates a thin layer of material which is difficult to machine and may be prone to warping during the initial build layers on the machine. Three solution were explored and are shown in the table below.

Table 14:Thermocouple Implementation

Solution	Explanation	CAD Model
0.2mm plate Insert	An insert for the build plate with 0.2mm shim shin nuts welded to it to secure it on the build plate. The thermal couples could be inserted in thru holes in the build plate up to the surface of the thin plate. Creating the necessary 0.2 mm barrier between the thermocouple and build plate top surface.	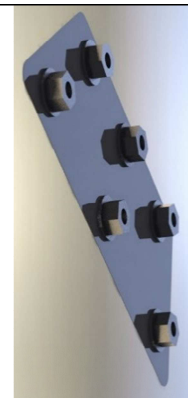
Modified Set Screw: Dog point	A threaded insert in which the thermal couple could be inserted through a hole drilled to 0.2 mm from the surface of the Dog point. Each set screw could then be inserted into the build plate in corresponding threaded counter bored holes.	
Hybrid Machined plate Insert	A combination of the first two methods an insert is machined to attach to the build plate with holes with which thermocouples can be threaded through the build plat up to the surface	

After reviewing these designs and the cost associated option 3 was chosen as the best choice due to its ease of manufacturability and is outlined in more detail in Figure 18.

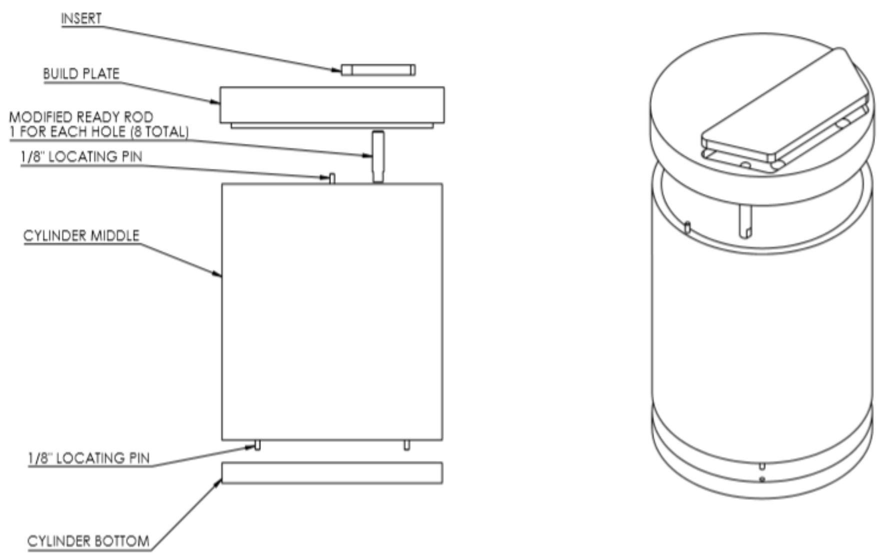

Figure 18: Thermocouple Installation Drawing

Pyrometer:

The pyrometer installation was more straight forward compared to the thermocouples as there was no need to have the sensor contact the surface. Only two requirements were laid out about the physical implementation of the sensor; the first was to have the pyrometer lens exactly 100 mm away from the build plate and the second was to have a viewing angle between 45-90 degrees both based on the pyrometers optical resolution(Table 10). With these requirements a CAD model was built to expand the existing build chamber to accommodate these requirements and manufactured. Additionally, a 6 degree of freedom mounting arm was manufactured so that the Pyrometer position could be adjusted. Shown below is the CAD model of the entire assembly.

Thermal Camera:

The installation of the thermal camera was done after the build chamber had been expanded (Figure 19, Figure 20). A fixture was designed to hold the thermal camera 25 cm from the build area. The fixture was designed to replace the existing window on the right side of the build chamber. This allowed the thermal camera's FOV to overlap with the build area. Shown below is the actual view of the expanded build chamber and fixture (circled in red).

Figure 19: Thermal Camera Fixture (Circled) and build chamber

Figure 20 shows the mounting fixture for the thermal camera, it should be noted that this fixture was also designed to house a high-speed camera which was not used in this research. A sapphire lens was also used to protect the thermal camera and was incorporated in the fixture.

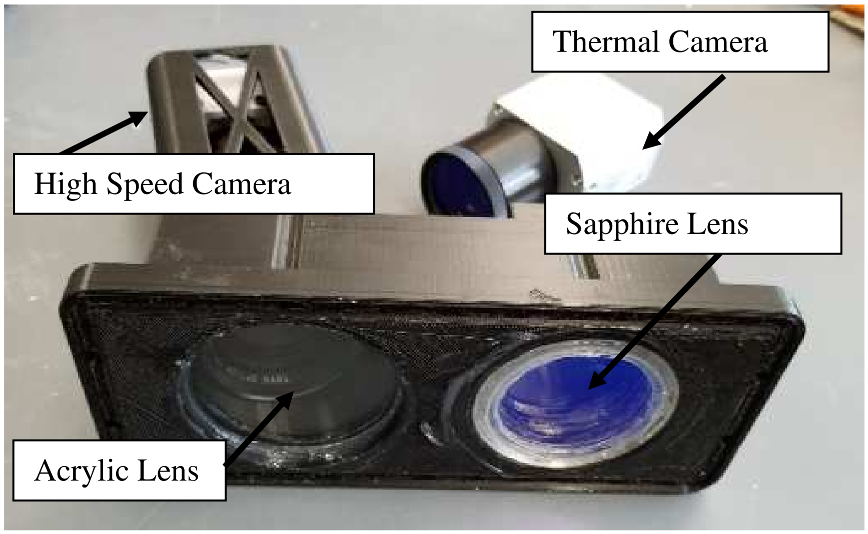

Figure 20: Mounting fixture

Testing

With the sensors installed initial testing was down to further validate the temperature readings. For the thermocouple a single thermocouple was purchased to perform testing rather than implementing the multiple sensors required to monitor the entire build area. This consideration was not needed with the thermal camera or pyrometer as only a one of each could be purchased. Test data was collected from IN625 and compared to literature. Additionally, the pyrometer was tested with H13 tool steel to validate the reading further.

Thermocouple:

With the thermocouple installed in the SLM machine it was possible to test to see whether it could record the temperature accurately. To do this a single coupon (1 cm x 1cm x1cm) was manufactured directly on top of the insert plate (Figure 18) where the thermocouple was installed. The test was performed, and a sample of the results are shown below in Figure 21.

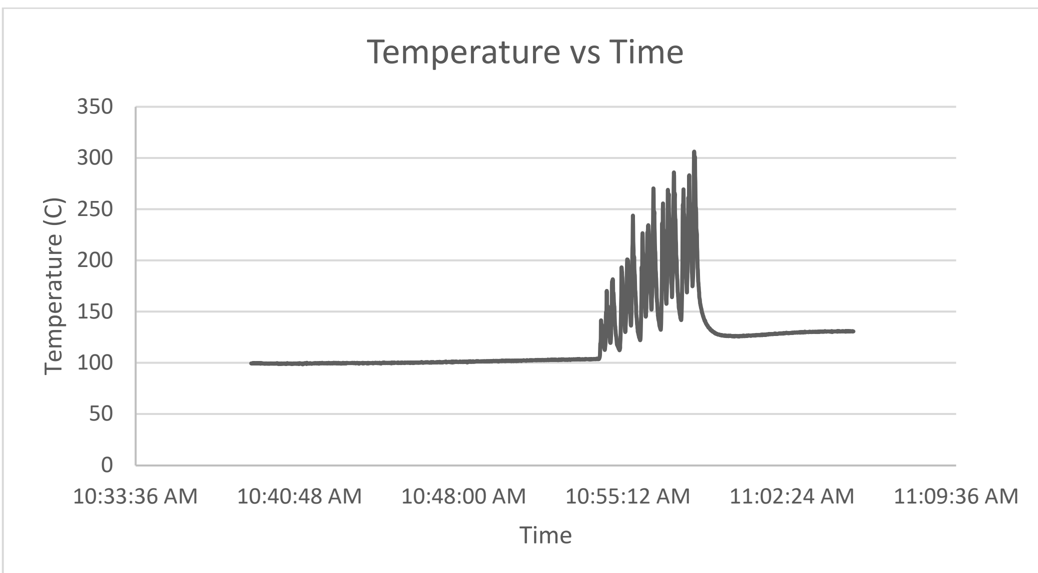

Figure 21: Thermocouple Data

Unfortunately, the thermocouple did not show any readings below a laser power of 300W. Additionally, over time it was seen that the temperature reading by the thermocouple continued to increase which was unexpected. It was unexpected because as the layer height increases the thermocouple was further away from the heat source and therefore should read a lower temperature. It was suspected that this was caused by the heating of the build plate itself and that the thermocouple was measuring the temperature of the build plate rather than measuring the melt pool temperature. Lastly, the B type thermocouple is only rated to above 875°C which means any result below that cannot be validated. The combination of these three effects meant that the B type thermocouple in this configuration was not a reasonable method for measuring the temperature.

Pyrometer:

Two tests with the pyrometer were performed. The first was to collect sample data from IN625 and to compare this data to literature. To further validate the results a second unrelated material, H13, was tested and compared to literature. H13 was chosen because more work has been done on the material and the material is readily available.

Shown below in Figure 22 is sample data from IN625 and it is compared to data shown in Figure 23 [58]. It is clear that these two figures show peak temperature measurements in the same range as each other. Additionally, in Figure 22 it is shown from IN625 testing shows 3 laser passes from each layer (this is changed by decreasing the FOV of the pyrometer in future tests).

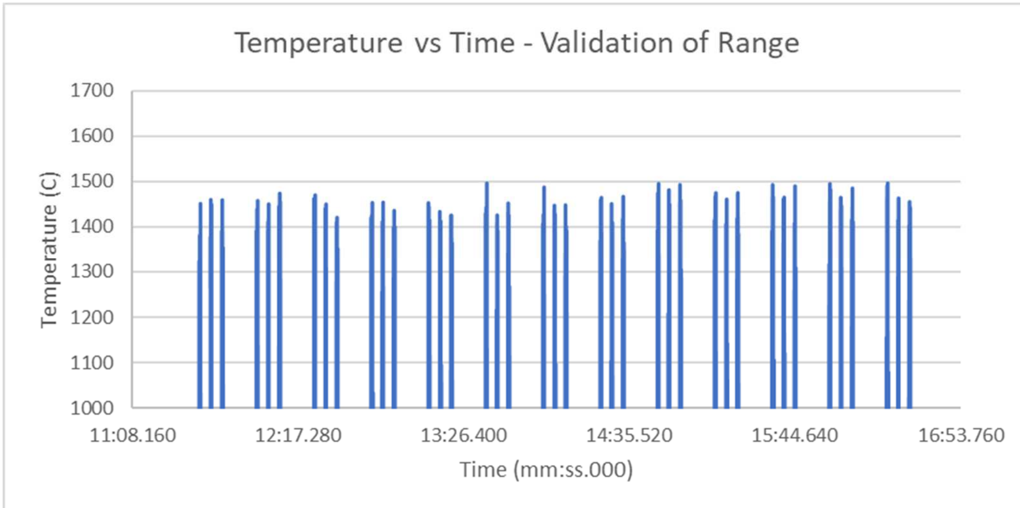

Figure 22: Inconel 625 Pyrometer Test Data

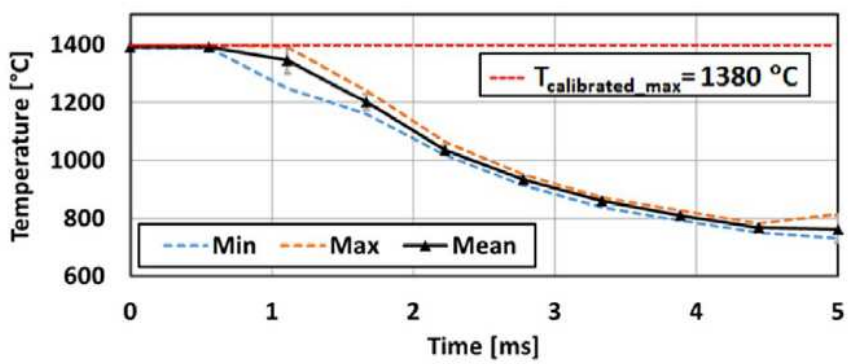

Figure 23: Inconel 625 Temperature Data [58]

Sample Data from H13 is shown below in Figure 24 and compared to a simulation from Manvatkar et al [59] shown in Figure 25. It shows that the temperature measurements being taken are within a reasonable range based on the simulation. Additionally, it should be noted that the FOV of the pyrometer was decreased to capture a single laser track.

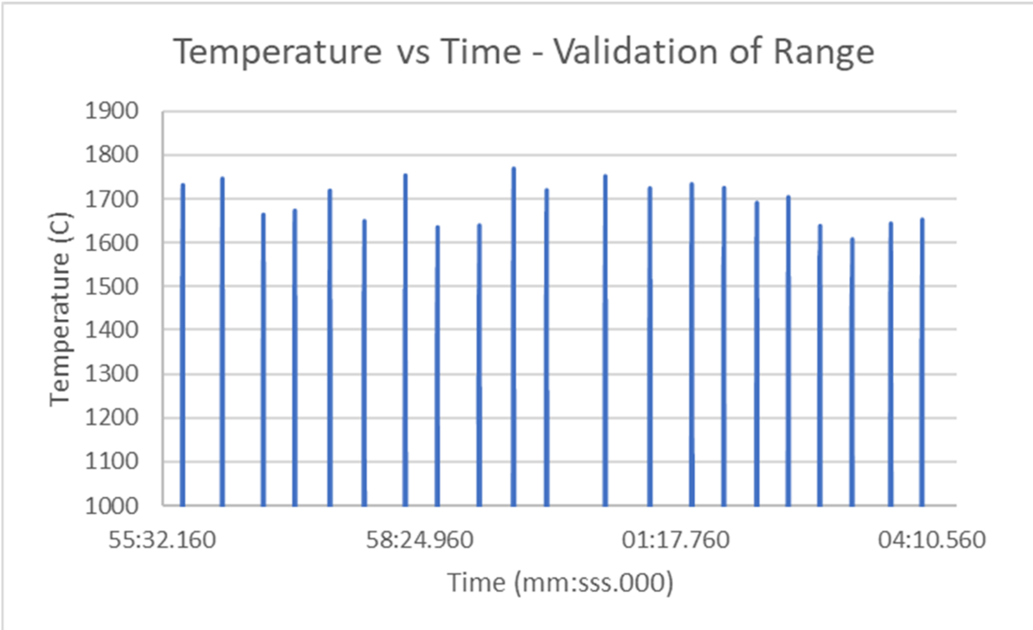

Figure 24: H13 Pyrometer Test Data

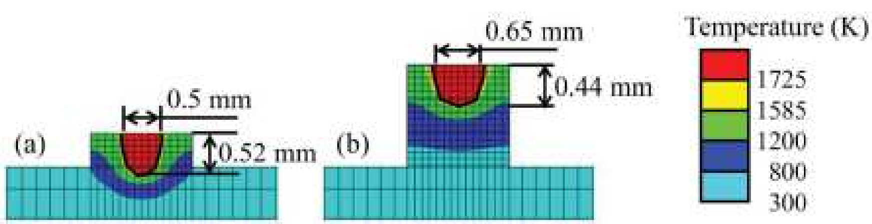

Figure 25: H13 Temperature Data [59]

Thermal Camera

To test the thermal camera after calibration a few trials were run at a range of process parameters. A sample of the image obtained is shown in Figure 26. Using the Optris software it is possible to monitor the peak temperature of the melt pool, set specific areas to monitor and measure temperature distribution across a path. Using these various modes, it is possible to track the melt pool at the beginning middle and end of the track.

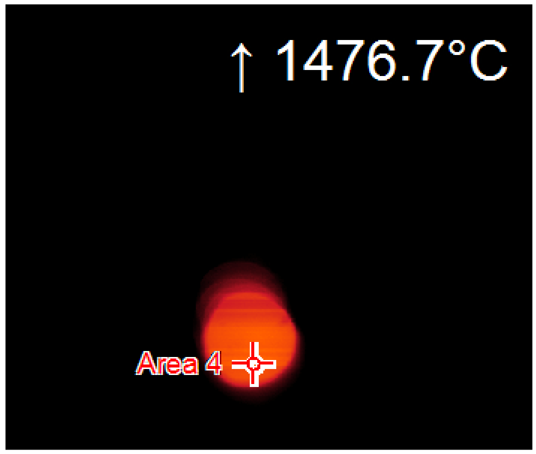

Figure 26: Sample data from Optris P1 08M thermal camera

Summary

In summary the thermocouple did not work in this application. The temperature measured is below the calibrated range of the thermocouples. The pyrometer worked very well in this application not only because it is non-contact, but because it overcomes all requirements set forth and measures accurately the peak temperatures. The thermal camera worked equally as well as the pyrometer but is an even more flexible tool in the information which can be extracted.

Chapter 3: Experimental Setup:

With the pyrometer and thermal camera in place and the calibration performed temperature data could be collected. In total 5 different experiments were conducted to explore the effects of laser power and scan speed on the peak melt pool temperature, examine the microstructure and microhardness at varying laser powers and to try and capture the response of the system. Each of the 5 experiments and the question they were trying to answer are listed below. **Note**: For 3 experiments an additional material Invar 36 was tested to validate the setup

1) Variation in laser power:

   What is the effect of laser power on peak melt pool temperature?

2) Variation in Scan Speed:

   What are scan speed effects on peak melt pool temperature?

3) Microstructure analysis:

   How does it relate to peak melt pool temperature and laser power?

4) Microhardness analysis

   How does it relate to peak melt pool temperature and laser power?

5) Temperature Profile

   What is the temperature distribution across the melt pool?

In all of the experiments where parts were manufactured the same scan strategy was used and is shown below in Figure 27 where it can be seen that no outline was used and single long stroke passes in the same direction were used to make the part. This strategy was chosen to eliminate variability in the components from changing the scan direction.

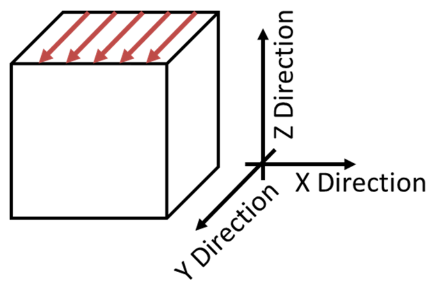

Figure 27: Scan Strategy

The pyrometer and camera were setup so that their field of views overlapped with one another. This allowed for the comparison of the results. Shown in Figure 28 is a simplified depiction of the set up. The blue line represents a single laser track with different areas to measure data. The pyrometer was pointed in the middle at Area 2 while the thermal camera was set up to monitor the entire track.

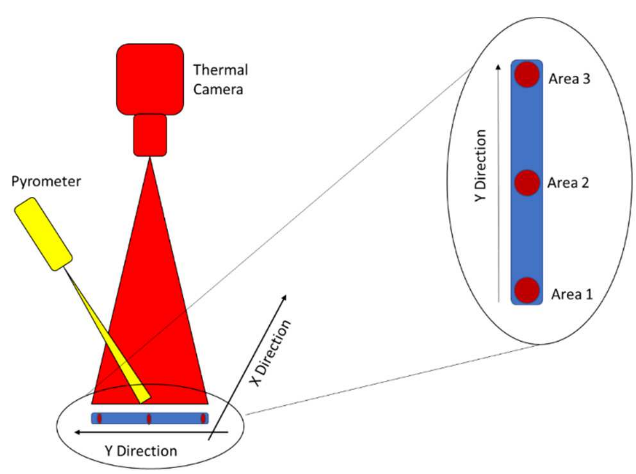

Figure 28: Simplified pyrometer and thermal camera set up

Each experiment is outlined in further detail below.

Experiment 1: Variation in Laser Power

In this experiment peak temperatures were recorded using the pyrometer while the laser power was changed, 5 laser powers were chosen for IN625: 100 W, 250 W, 300 W, 350 W and 400 W and for Invar 36: 100 W, 200 W, 250W, 300 W and 400W. Table 15 shows the remaining process parameters. Each laser power was tested twice with 20 layers built each time. The 10 peak temperatures were recorded for each layer.

Table 15: Experiment 1 - Process Parameter

Process Parameter	**Value (IN625)**	**Value (Invar 36)**
Scan Speed	200 mm/s	400 mm/s
Contour Passes	0	0
Hatch Spacing	0.1 mm	0.1 mm
Layer Thickness	0.04 mm	0.04 mm
Beam Diameter	0.09 mm	0.09 mm
Laser Power	Variable	Variable

Experiment 2: Variation in Scan Speed

In this experiment peak temperature was recorded using the pyrometer while the scan speed was changed, 4 scan speeds were chosen for IN625 : 200 mm/s, 300 mm/s, 400 mm/s, 600 mm/s and 3 for Invar 36: 200 mm/s, 300 mm/s and 400 mm/s. Table 16 shows the remaining process parameters. Each scan speed was tested twice with 20 layers built each time. The 10 peak temperatures were recorded for each layer.

Table 16 Experiment 2 - Process Parameters

Process Parameter	Value (Inconel 625)
Scan Speed	Variable
Contour Passes	0
Hatch Spacing	0.1 mm
Layer Thickness	0.04 mm
Beam Diameter	0.09 mm
Laser Power	350 watts

Experiment 3: Microstructure

In this experiment 5 coupons (1cm x 1cm x 1cm cubes) were manufactured at different laser powers. The laser power and process parameters for these 5 coupons corresponded with those in Experiment 1. The manufactured coupons were used to investigate the microstructure of each material, specifically the primary dendritic arm spacing (PDAS). Using an SEM, 10 PDAS measurements were taken at 3 locations (Bottom Middle Top of the coupon) seen in Figure 36. Comparisons were also made between the PDAS and the peak temperature at different laser powers from Experiment 1. Lastly, comparisons were made between the micro structure and cooling rates at each laser power.

Experiment 4: Microhardness

In this experiment the 5 coupons manufactured in Experiment 3 were tested for microhardness. 15 measurements were taken for each part. The measurements were then compared to the PDAS from Experiment 3.

Experiment 5: Temperature Distribution

In this experiment the thermal imager was used to evaluate the temperature at different melt pool locations at varying laser powers. The chosen locations to measure were at the beginning (area 1), middle (area 2) and the end (area 3) of first laser track of each layer. As each layer of the coupon was manufactured the peak melt pool temperature were recorded at each area. The manufactured coupon had a size of 10 mm x10 mm x 35 mm. In the figure below the blue area represents a laser path while which red circle is the area measured from the thermal camera.

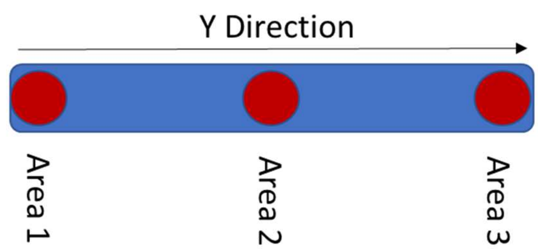

Figure 29: Measuring locations along laser track

Over ten layers the peak temperature of each area was recorded for the first laser pass. This was repeated for three laser powers (250 Watts, 300 Watts, 400 Watts). The other process parameters used can be seen in Table 17.

Table 17: Process parameters for thermal camera experiment

Process Parameter	**Value (Inconel 625)**
Scan Speed	200 mm/s
Contour Passes	0
Hatch Spacing	0.1 mm
Layer Thickness	0.04 mm
Beam Diameter	0.09 mm
Laser Power	Variable

Additionally, samples of temperature profiles of the melt pool were collected at each area and can show the profile of the melt pool across its length as shown in Figure 30.

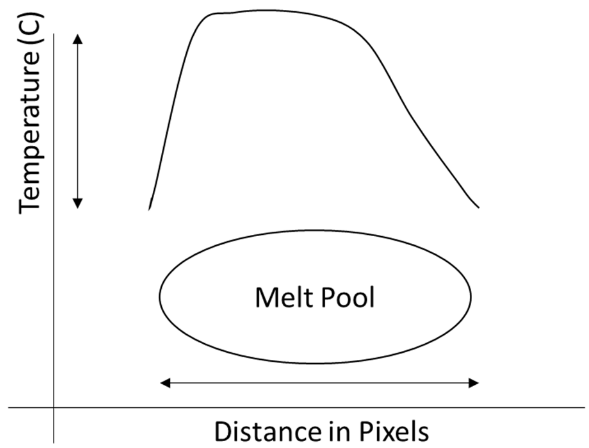

Figure 30: Temperature profile of melt pool

Chapter 4: Experimental Results and Discussion

The following section reviews the results from all 5 experiments and discusses the relationship between different process parameters, melt pool temperatures and the step response to the laser.

Experiment 1: Results:

Inconel 625

The peak temperature results from Experiment 1 can be seen in Figure 31, Figure 32 and Table 18 which relate peak temperature to the laser power and show that the melt pool temperature increases with an increase in laser power.. Figure 31 shows the distribution of the data collected at each laser power and demonstrates a tight spread of data. Additionally, from Table 18 it can be seen that the largest spread (within the inter quartile range(IQR)) is 19.5°C again showing a tight spread of data at each laser power. Furthermore, the melt pool temperature is well above the melting point of IN625 (1390°C) with the lowest temperature 1454.5°C and the highest temperature recorded 1514.4°C. However, this also means that the change in temperature from the lowest laser power to the highest laser power was only 56°C which is discussed further below.

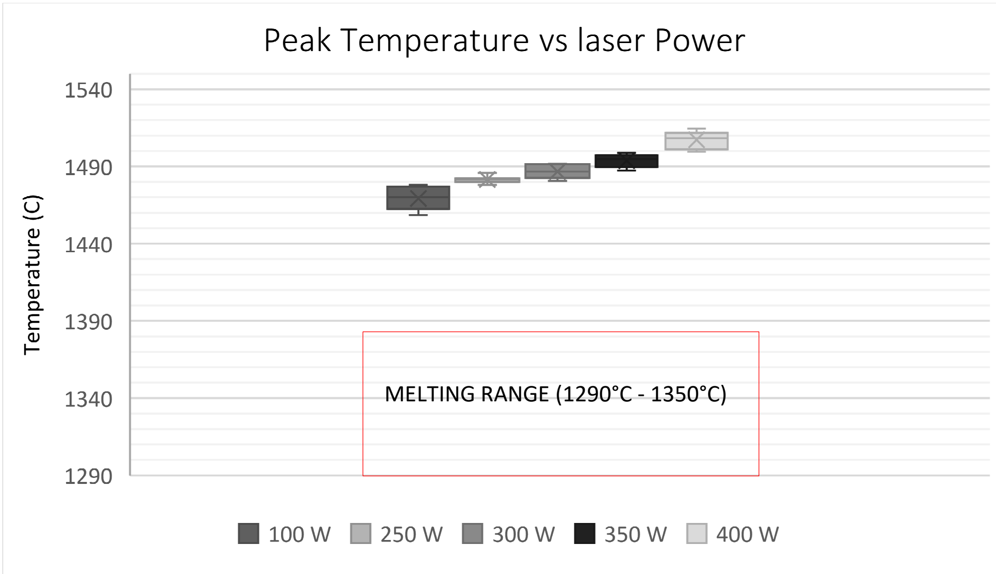

Figure 31: Inconel 625 - Peak Temperature with Varying Laser Power

Table 18: Inconel 625 Experiment 1 – Results (Laser Power)

Power	**100 W**	**250 W**	**300 W**	**350 W**	**400 W**
Average (°C)	1469.2	1481.5	1486.7	1493.7	1507.3
Max(°C)	1477.9	1490.9	1491.7	1498.8	1514.4
Min(°C)	1458.4	1477.9	1480.6	1487.3	1499.6
STD(°C)	7.3	9.1	4.1	4.0	5.2

In Figure 32 a plot of the average peak temperature of each laser power shows a strong linear relationship between the peak temperature of the melt pool and laser power (R^2 = 0.9244).

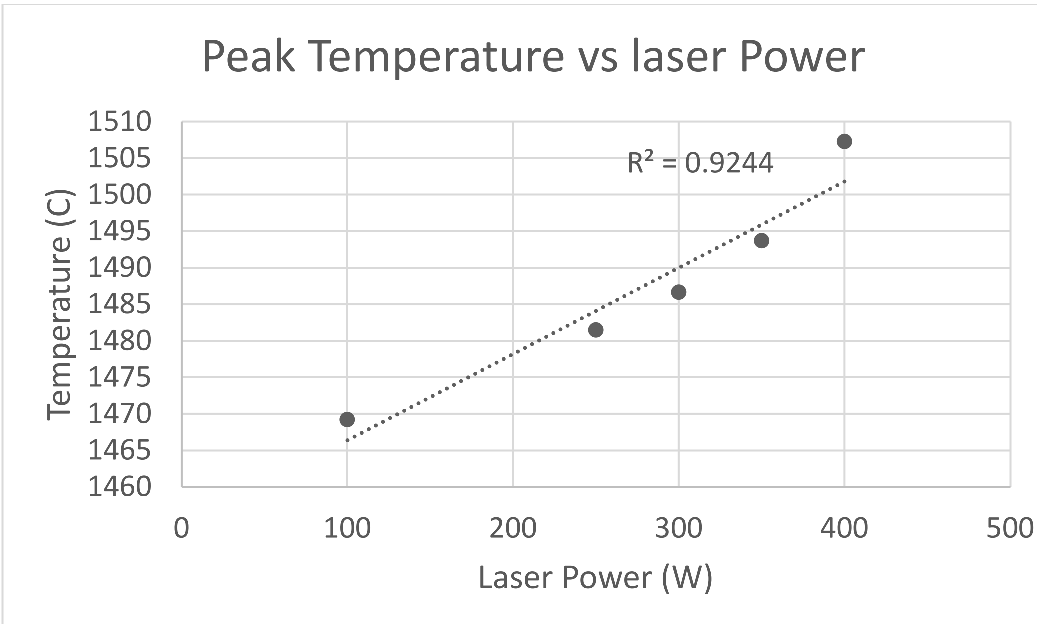

Figure 32: Inconel 625 - Average Peak temperature vs Laser Power

Invar 36

From the box plot in Figure 33 an interesting trend can be seen in the Invar 36 data in which the spread of data is increasing as the laser power increases, with a standard deviation of 23°C at the 300 Watts and 12.6°C at 100 Watts. Additionally, outliers can be seen at higher laser powers (2 at 300 W and 1 at 400 W), which implies that with higher laser power there is a larger spread in data, however this trend is unique to this data set and cannot be seen in IN625 or in Experiment 2 as discussed below.

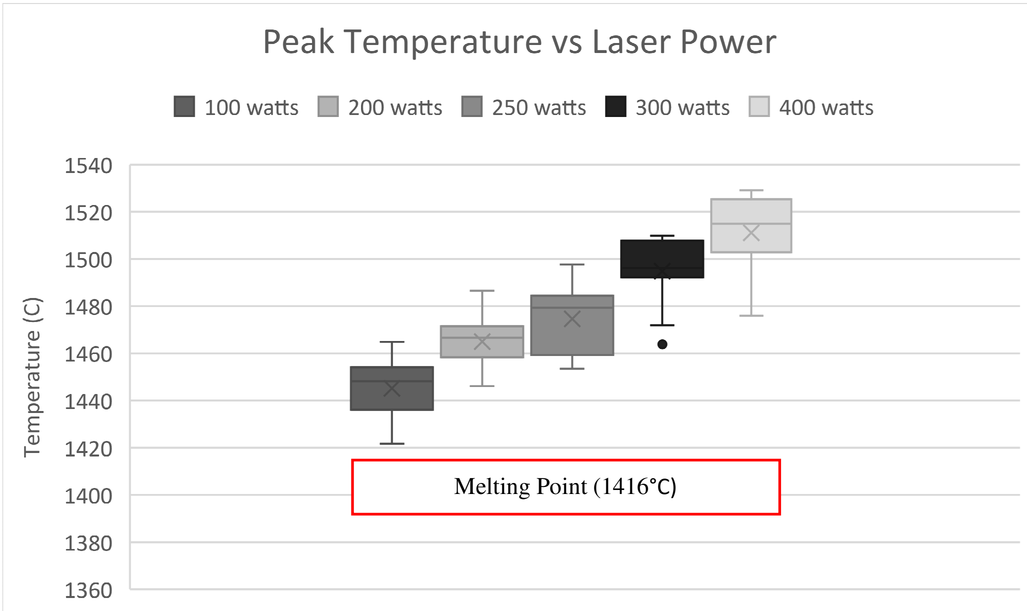

Figure 33: Invar 36 - Peak Temperature with Varying Laser Power

From Figure 33 the maximum temperature at 400 W was recorded to be 1529.1°C and the lowest temperature at 150 W is 1421.7°C which although are both above the melting point of Invar 36 are fairly close together (108°C) showing that the increase in laser power did not have a large impact on temperature change as was shown in IN625 Experiment 1. Similarly, to Experiment 1 with IN625 the results from Invar 36 also show a strong linear correlation between the laser power and peak temperature as per Figure 34 (R^2 =0.9946).

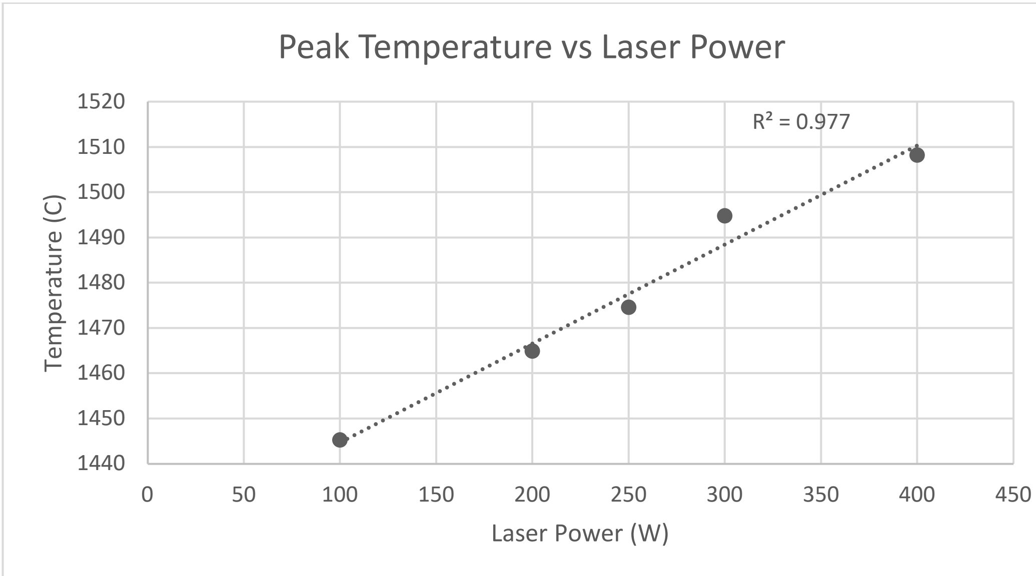

Figure 34 : Invar 36 - Average Peak temperature vs Laser Power

Summary

Overall both materials showed a strong linear relationship between laser power a peak temperature and the peak temperatures captured for IN625 can be confirmed from Criales et al [58] as was shown in the testing phase of the pyrometer. It should be noted that the increase in temperature from laser power increase was not significant for either material as shown in Figure 31 and Figure 33**.** It is suspected that this increase in temperature is not magnitudes larger since as the laser power is increased the melt pool has a more significant change in size rather than temperature. That is to say as energy is added to the melt pool from the laser (i.e. an increase in laser power) more of the surrounding powder absorbs this energy growing the melt pool in size rather than increasing the peak temperature dramatically. Similar results have been seen in welding process within the weld pools [60][61].

Experiment 2: Results

Inconel 625

When varying the scan speed, the results for Inconel 62 show a more significant change in peak temperature compared to when laser power was changed. It can be seen in Figure 35 that the peak temperature decreases with an increase in scan speed. Additionally, the temperature has a tight spread meaning that the peak temperature was consistent at different scan speeds and also shows a strong linear relationship between the scan speed and peak temperature (R^2 = 0.9991 with averages plotted against scan speed).

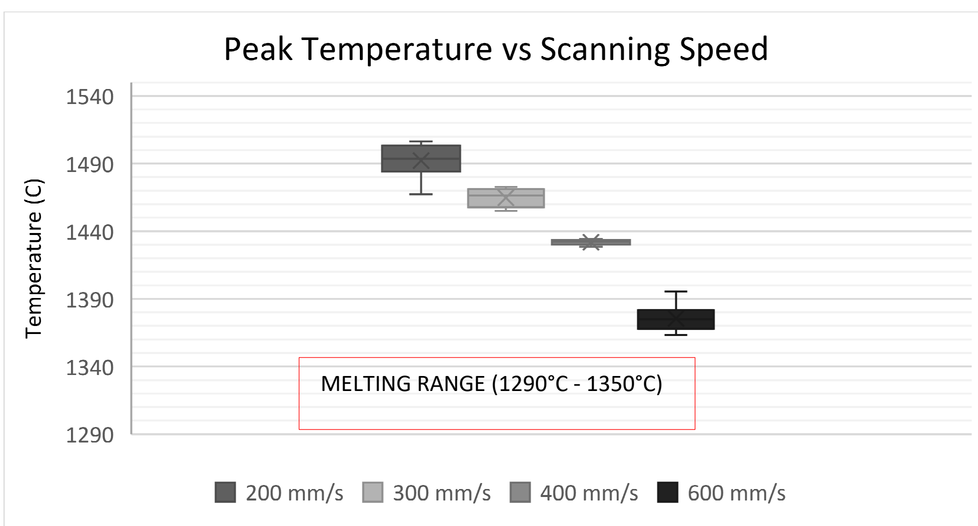

Figure 35: Inconel 625 - Peak Temperature with Varying Scan Speed

Furthermore from Table 19 it can be seen that the temperature changes 116 °C from its slowest scan speed to its highest scan speed which is significantly higher than the 56°C observed in Experiment 1.

Table 19: Inconel 625 – Results (Scan Speed)

Scan (mm/s)	**200**	**300**	**400**	**600**
Average (°C)	1492.3	1464.7	1431.9	1375.6
Max(°C)	1506.4	1472.7	1434.1	1395.3
Min(°C)	1467.3	1455.1	1428.5	1363.3
STD(°C)	12.3	6.6	1.8	9.3

Summary

Overall IN625 showed a strong linear correlation with the scan speed. Additionally, the scan speed seems to have more of an impact on the peak temperature compared to the laser power. This is suspected due to the fact that the scan speed influences the exposure time the laser has with the material and the less exposure time means the less time to absorb energy.

Experiment 3: Results

As noted in the outline of this experiment, 5 coupons were manufactured to explore microstructure. Each coupon printed was cross sectioned perpendicular to the build direction (shown in Figure 36). The then cross sectioned part was mounted and polished using standard microscopy techniques. Both materials results are presented below with a description of the etchants used to look at PDAS. Once the parts were cross sectioned and etched images were taken using a SEM at the bottom (1), middle (2) and top (3) as shown in Figure 36 and the arm spacing was measured using a software called ImageJ.

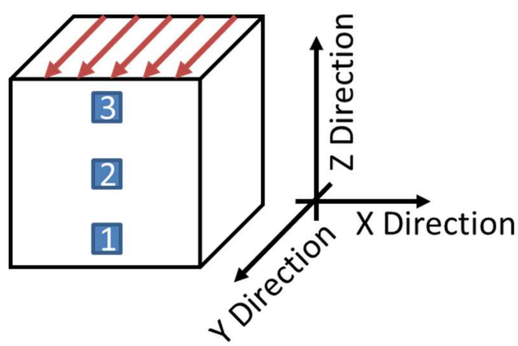

Figure 36: Cross section and Image Locations for primary arm spacing

Inconel 625

After the coupons were manufactured, cross sectioned and mounted it was possible to etch them to investigate the microstructure. After experimenting with Kallings number 2 and Aqua Regia etchants on the IN625 coupons neither worked to show microstructure. Instead of etching the surface of the coupon these reagents exposed scratches over the polished surface. It is suspected that this was caused by either small troughs on the surface of the coupon which the etchant would get trapped in and eat away the material or from the work hardened surface from polishing which may have had sub surface scratches. It was found that an electro etch with an electrolyte solution of 10 grams of Oxalic acid and 100 ml of water at 6v for 15-45 seconds worked very well to reveal the microstructure. The electro etch setup was placed on a magnetic stirrer with stir bar to make sure the electrolyte was flowing over the sample; a copper cathode was used with a steel anode. The etched samples were then photographed using Scanning Electron Microscopy (SEM) and an example can be seen below in Figure 37.

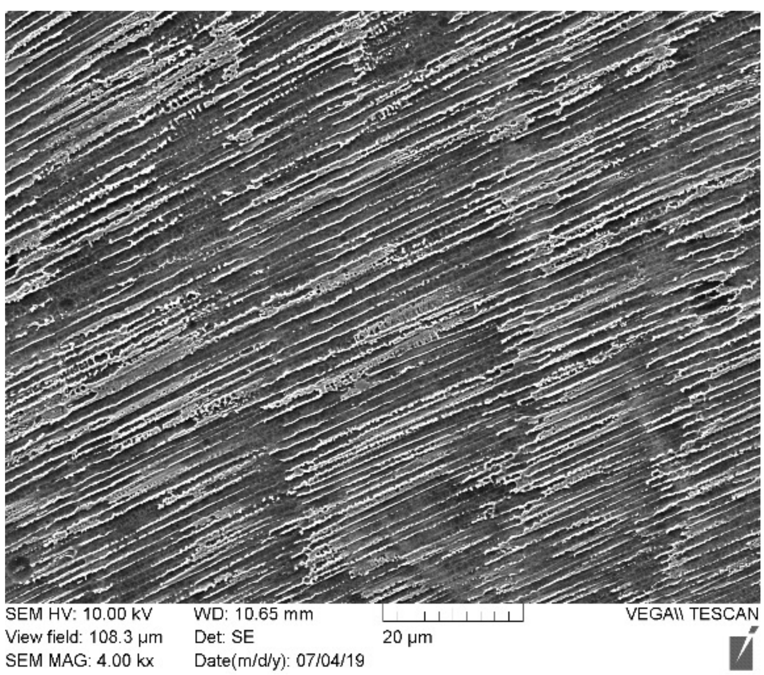

Figure 37: Example of Etched Inconel 625

The images were measured and the average PDAS from each sample was plotted against the corresponding laser power (Figure 38) to see the effects laser power had on the resulting microstructure. It can be seen that the average PDAS increases as the laser power increases from 0.7 to 1.02 um. The arm spacing measured are also similar to those recorded by Amato et al [62] who saw arm spacing between 0.5 and 1 um in Inconel 718. This trend of increasing PDAS makes sense from what was learned in Experiment 1, with higher laser power the melt pool grows in size and the peak temperature increases meaning that there is more heat and energy in the melt pool which would in turn take longer to cool which results in large arms and thus larger PDAS.

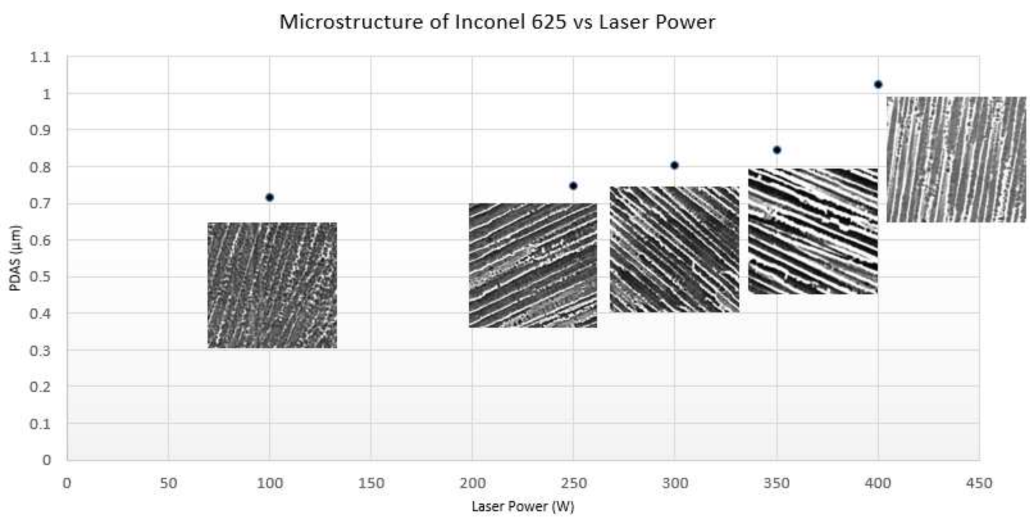

Figure 38: Inconel 625: Average PDAS vs Laser Power

This can also be confirmed by looking at the cooling rates vs the laser power shown below (Figure 39) which confirms that the cooling rate is decreasing with an increase of laser power a trend also seen by Crailes et al. [58].

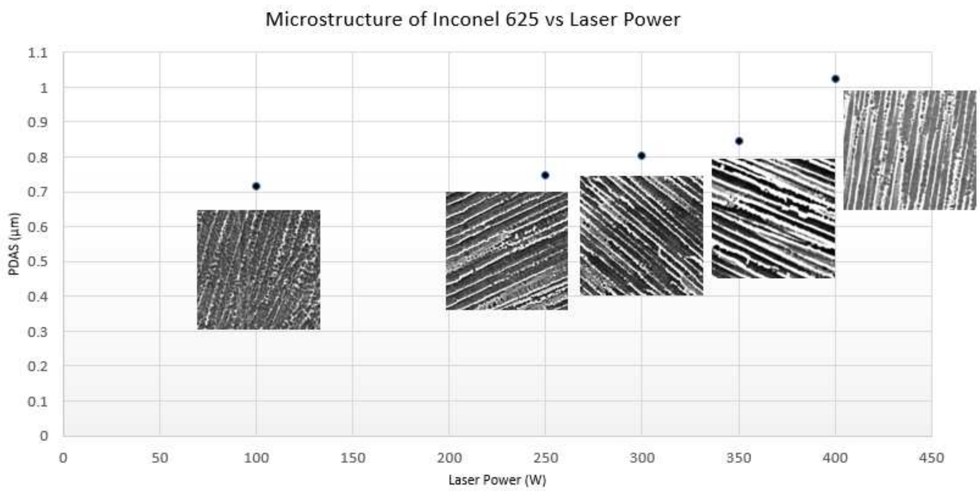

Figure 39: Inconel 625 Cooling Rate vs Laser Power

Invar 36

Just as was done with Inconel 625, Invar 36 was etched after the coupons were cross sectioned, mounted and polished. The etchant used was Kallings number 2 and was applied with a cotton swap in approximately 3 second intervals and was checked continually using an optical microscope. This was highly effective at etching these parts and revealed the PDAS which was photographed using a SEM. An example is shown in the following figure.

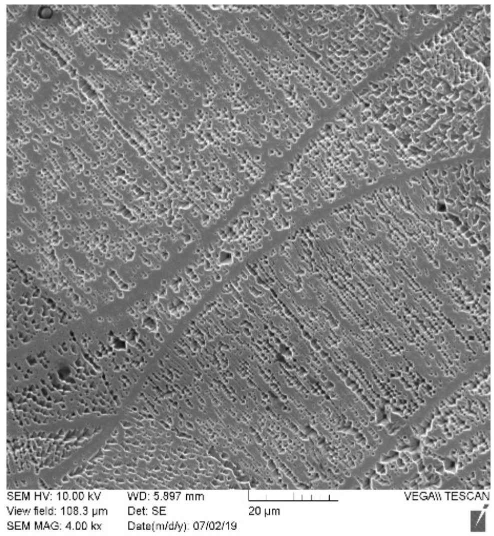

Figure 40: Example of Etched Invar 36

Like IN625 Invar 36 showed an increase in the PDAS with an increase in laser power shown in FIG. The increase in PDAS is from 0.7 um to 1.5 um on average across the different laser powers.

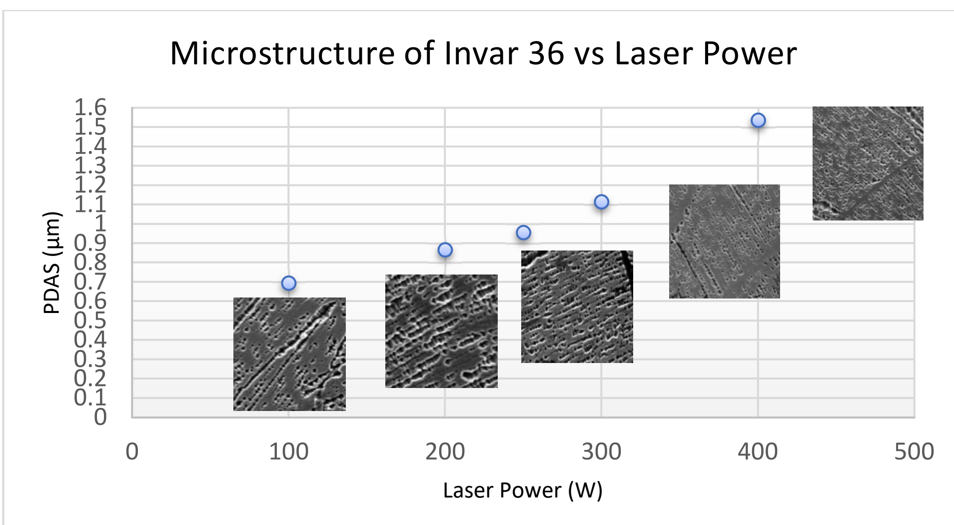

Figure 41: Invar 36: Average PDAS vs Laser Power

Similar to IN625 it is believed that the cooling rate decrease with an increase of laser power. The following figure shows that this trend holds up for Invar 36 as well.

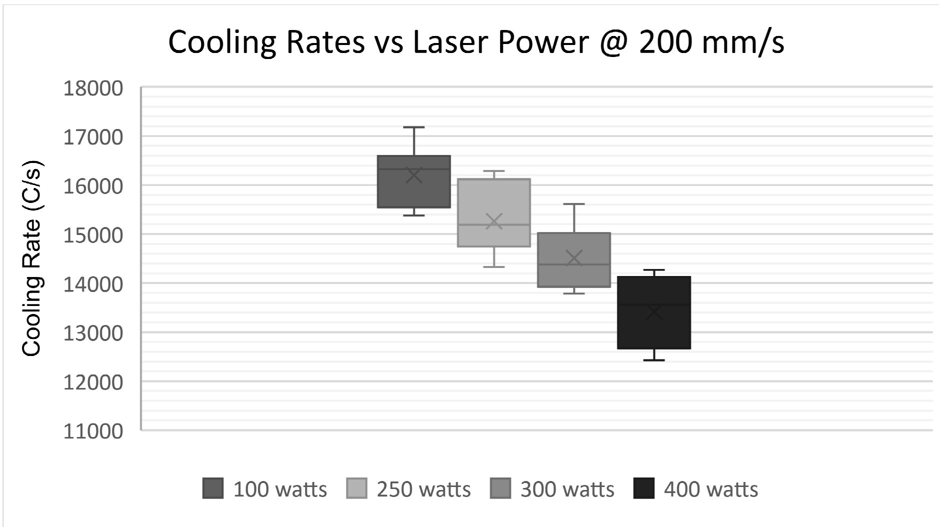

Figure 42: Invar 36 Cooling Rate vs Laser Power

Note: The results for cooling rates of both Invar 36 and IN625 need further validation. The pyrometer did not have the capability of recording the cooling rate consistently due to the extremely fast nature of the cooling rates. It took many trials to get consistent enough readings of the cooling rates for this experiment. Due to the lack of data points the methodology for calculating the cooling rate from that data was done by taking the peak temperature at time and the lowest temperature and time and finding the slope. These experiments should be redone with a sensor which can constantly measure the cooling rates.

Summary

Over all Experiment 3 showed that there is a relationship between the PDAS for both IN625 and Invar 36 and the laser power used. The relationship is suspected to be related to the peak temperature as well as melt pool size however additional experiments would need to be run to ensure no other factors were involved. Additionally, as the PDAS is related to the cooling rate it is shown that the cooling rate is also affected by peak temperature and laser power suggesting that laser power can be used to change to resulting microstructure of the parts.

Experiment 4: Results

In Experiment 4 the coupons were manufactured at 100 watts and 400 watts with the remaining parameters the same as shown in Table 15. The samples were cross sectioned perpendicular to the build direction as per Figure 36.

The results for both IN625 and Invar 36 show and increase in hardness of, on average, 80 Hv and 30 Hv respectively with an increase in laser power and can be seen in Figure 43 and Figure 44. Similar results have been shown by Brown et al. [63] and confirm that the change in laser power not only effects the microstructure but also the mechanical properties.

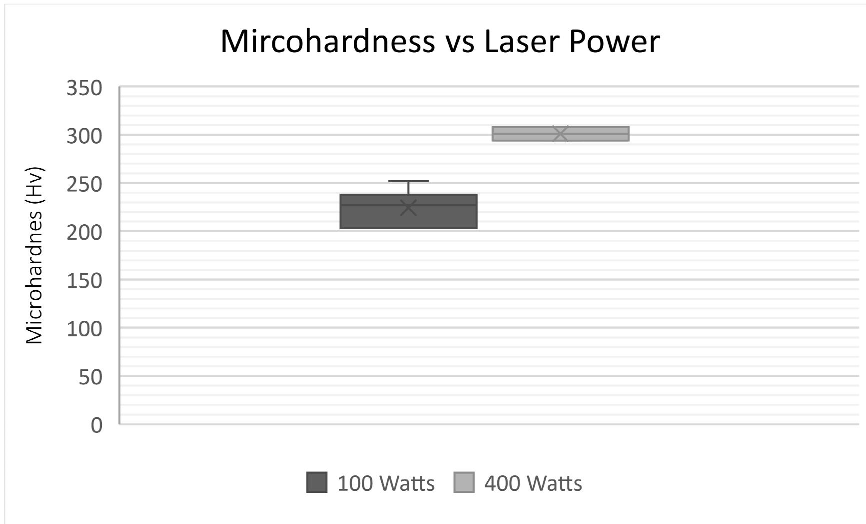

Figure 43: Inconel 625 - Microhardness at different laser powers

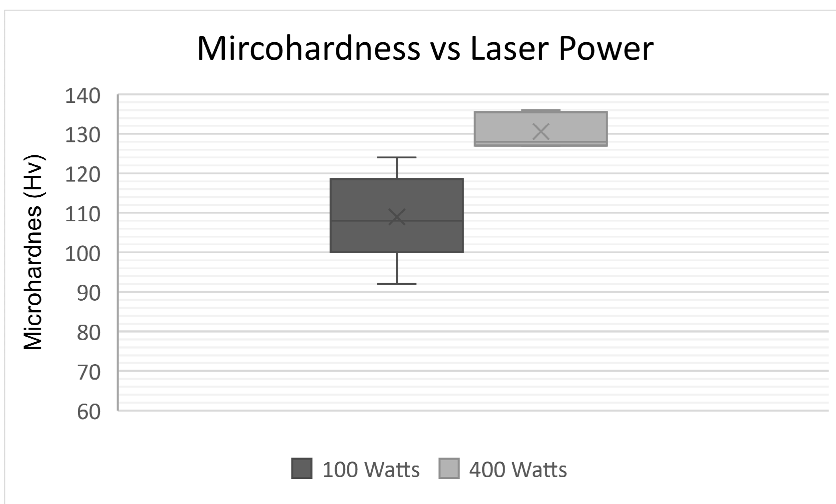

Figure 44: Invar 36- Microhardness at different laser powers

Experiment 5: Results

The peak melt pool temperature was collected at 3 different areas on the laser path as depicted in Figure 45. In Figure 45 the peak temperature in Area 3 is 1444.6C, as the melt pool moved across the areas the peak temperature was recorded.

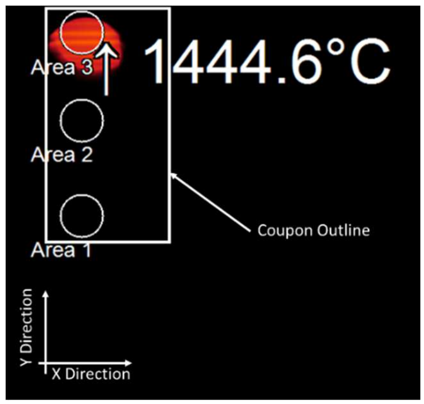

Figure 45: Example of thermal camera data

The peak temperature of each melt pool was recorded for the first laser track (Figure 46) of each layer for 10 layers at three laser powers of 250 watts, 300 watts and 400watts.

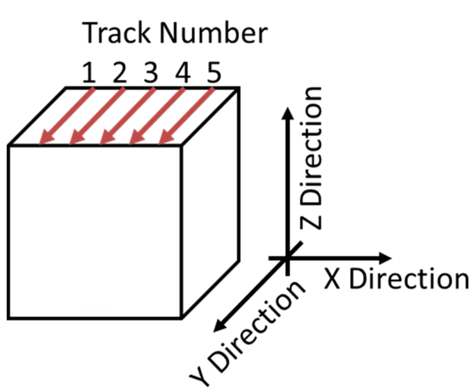

Figure 46: Track number illustration

Along with the peak temperature, data was also collected to show the temperature profile of the melt pool as shown below. In Figure 48 the graph shows the temperature across the middle of the melt pool. Figure 47 is a simplified for of the temperature profile and path.

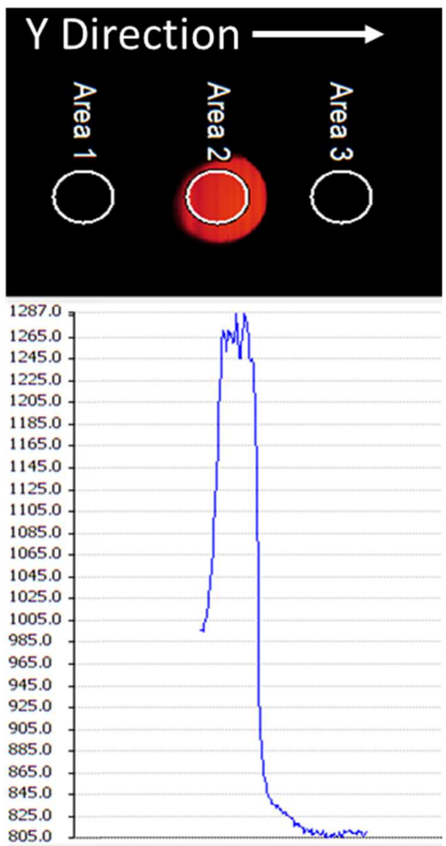

Figure 48: Sample of melt pool profile

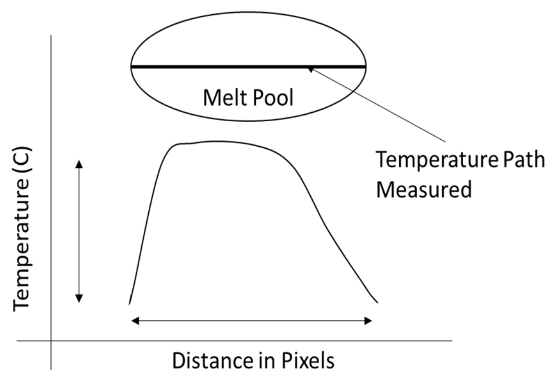

Figure 47: Temperature path measured in the melt pool

Peak Temperature

The average peak melt pool temperature was recorded in each area are summarized in

Table 20. An average of the three areas is also shown and is compared to the result of the pyrometer in experiment 1. When comparing the two experiments the average taken from the thermal camera is in a strong agreement with the pyrometer averages with the maximum difference being 12.4°C.

Table 20: Temperature at start, middle and end of laser track

Laser Power	**Area 1 (°C)**	**Area 2 (°C)**	**Area 3 (°C)**	**Area Averages (°C)**	**Pyrometer Average (°C)**
250 Watts	1477.3	1476.7	1460.9	1471.6	1481.5
300 Watts	1473.6	1482.7	1481.7	1479.3	1486.7
400 Watts	1504.8	1486.1	1493.8	1494.9	1507.3

To further examine the results the peak temperatures recorded are plotted across each of the ten layers. Figure 49, Figure 50 and Figure 51 show these plots. However, they do not show any visible trends at different areas of the laser track..

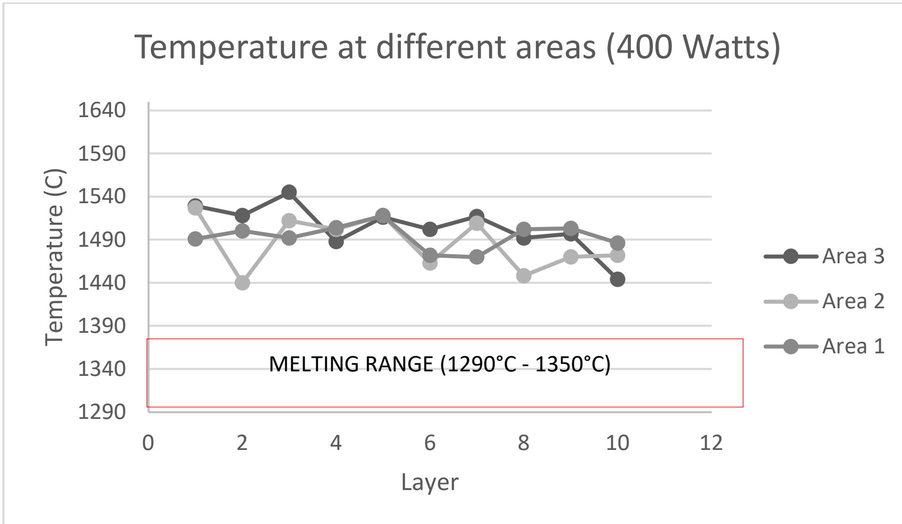

Figure 49: Temperature at each area for 400 Watts

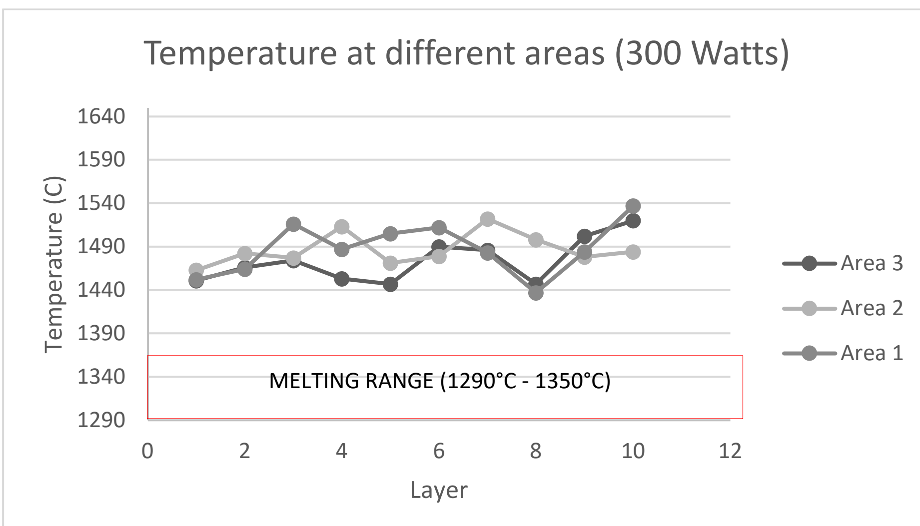

Figure 50: Temperature at each area for 300 Watts

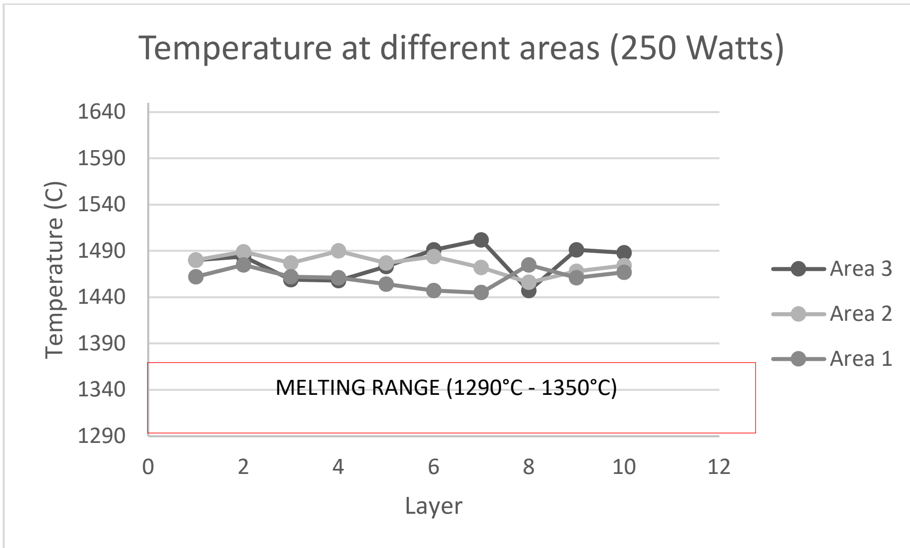

Figure 51: Temperature at each area for 250 Watts

Temperature Profiles

As depicted in Figure 47 given a temperature profile or path it is possible to capture the temperature across that path. This was done at each area along the laser track for each laser power. The interesting part of the temperature profiles collected is that they resemble a second order response. Shown Figure 52 is an example of melt pool profile temperature. Note: This is the temperature response is that of the melt pool (within the layer) and does not represent the temperature response of the part temperature (layer to layer). Based on the profile, the melt pool response is believed to be a second order underdamped system. Some clues are available looking at the response or profile of the melt pool. Firstly, looking at the steady state value there is a clear over shoot in the response. A first order system cannot oscillate as it has no oscillatory components and therefore will not have over shoot. If a system does have overshoot it is at least a second order system which is underdamped as a system which is over damped or critically damped also has no overshoot. An overshoot can be observed as is highlighted in Figure 52 .

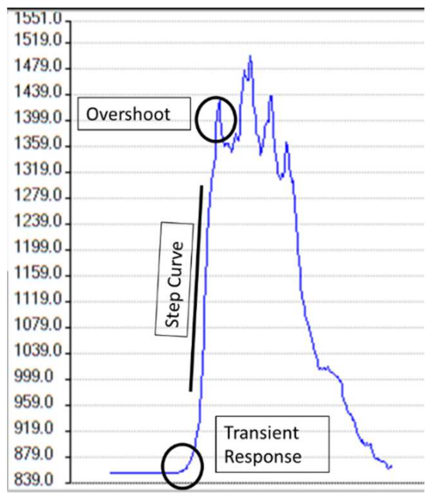

Figure 52: Example of in layer melt pool response

Another check which can be performed is to examine the initial transient response, which can be examined for the slope and shape of the initial rise of the response. That is to ask if the response starts with a small exponential shape followed by an aggressive slope or is it instead a smooth increase to the steady state value. Examining the output of the response there is a steep slope to the initial transient response as well as an exponential component as shown above. This leads to the conclusion that this system can be modelled using a second order underdamped model if it is desired to control the laser power within each layer rather than layer to layer. The following pages show examples of laser tracks at the different laser powers in support of this hypothesis.

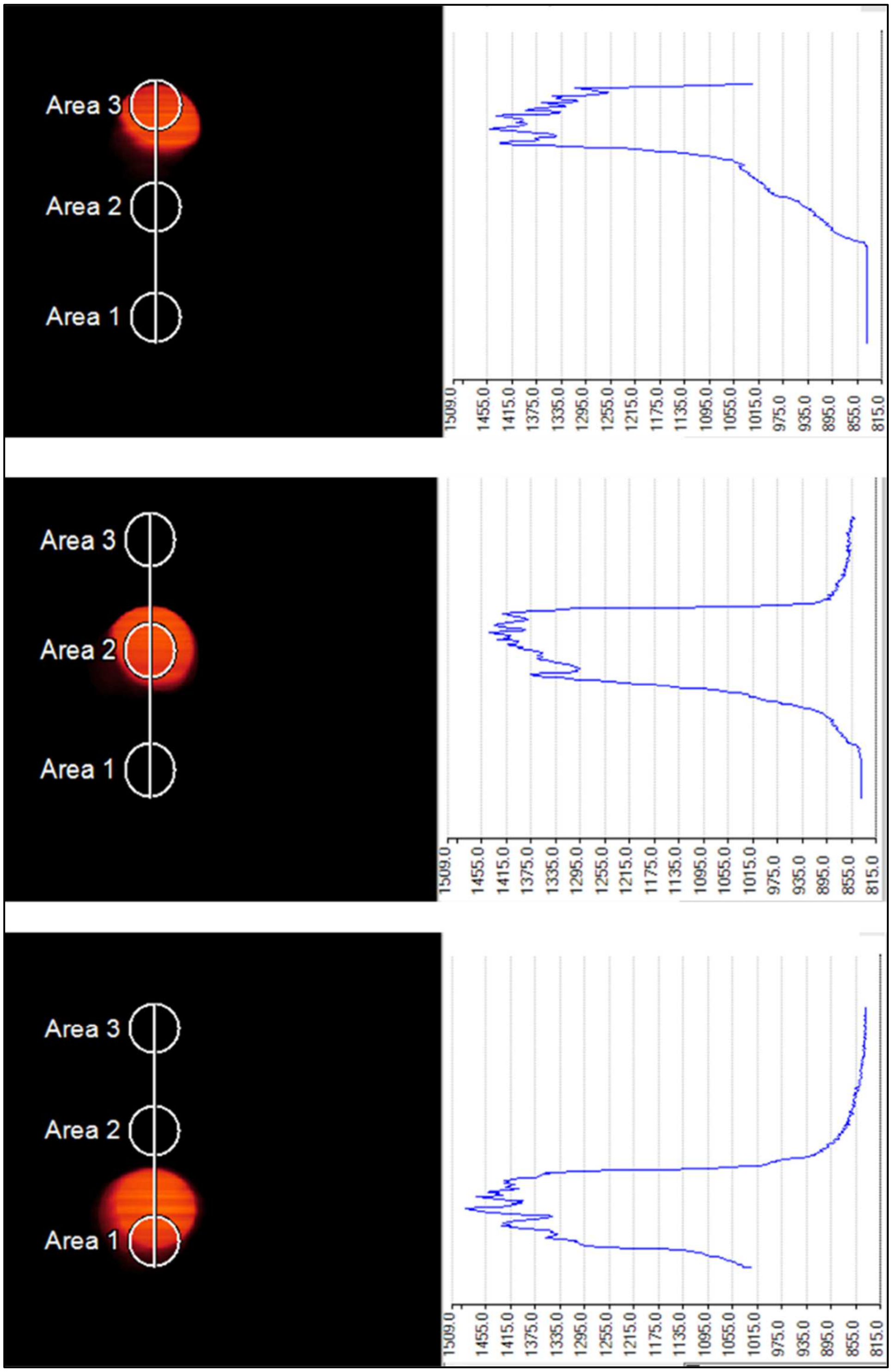

Figure 53: Temperature profile example 1 250 watts

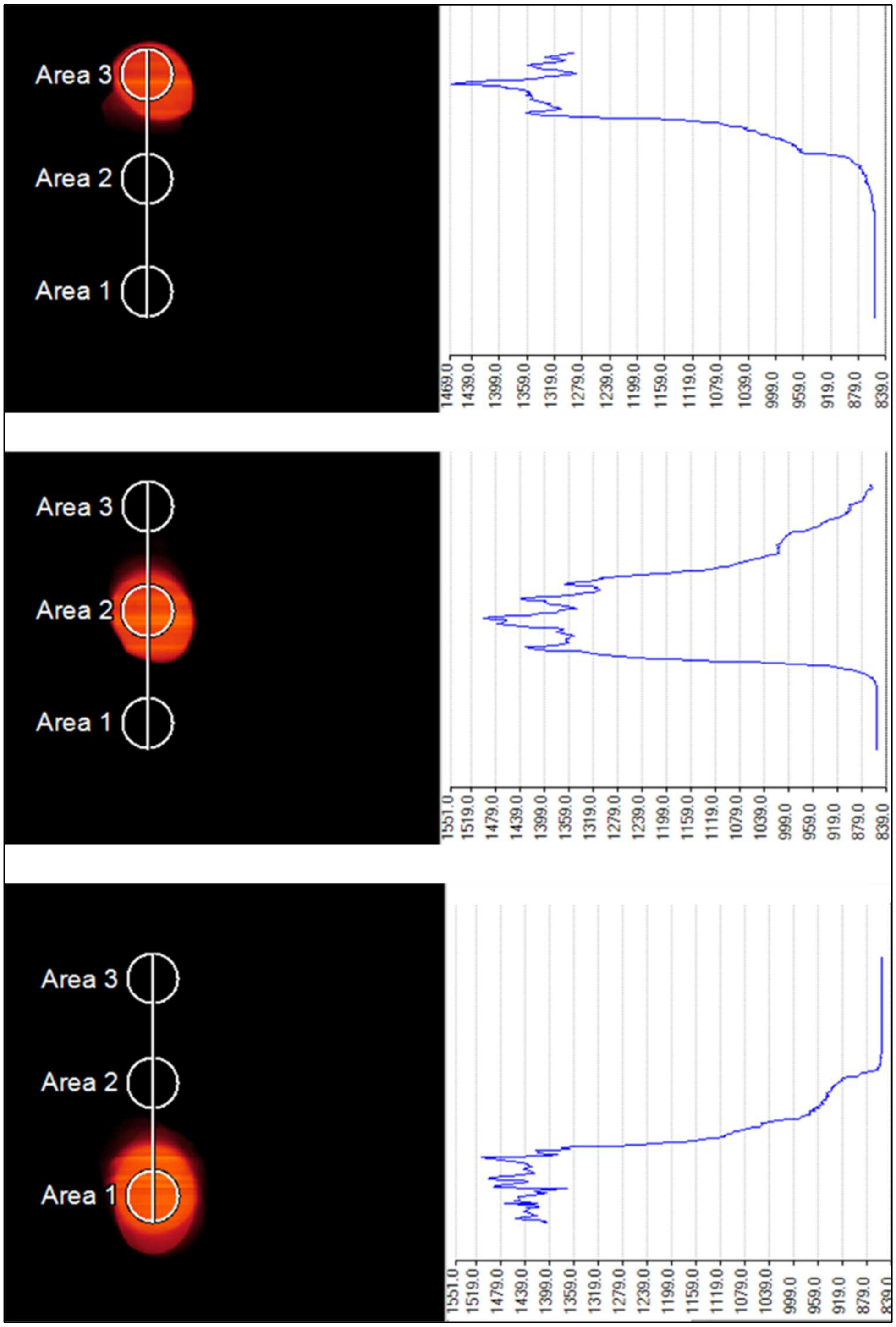

Figure 54: Temperature profile example 1 400 watts

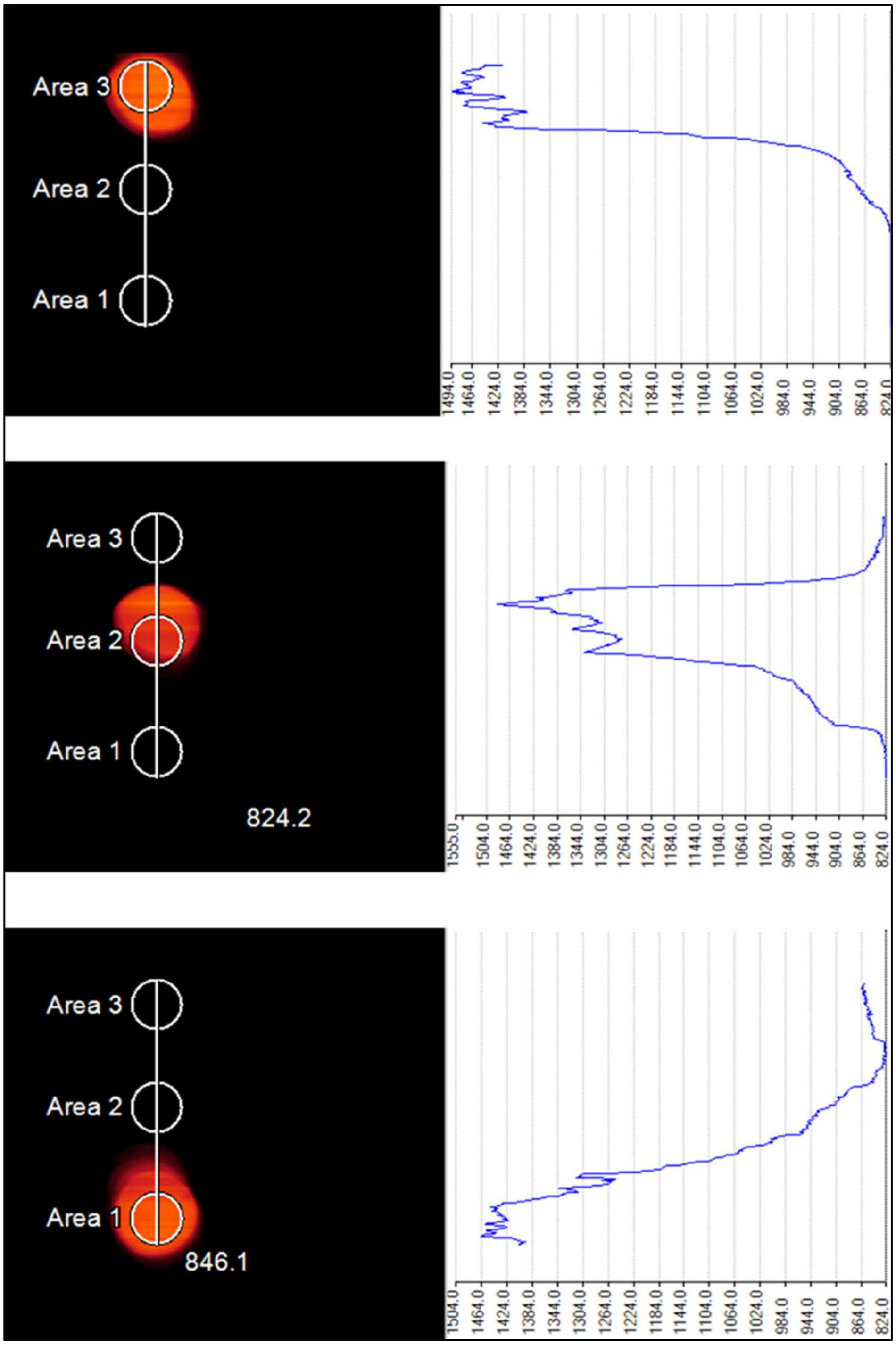

Figure 55: Temperature profile example 1 300 Watts

Chapter 5: Modelling and Simulation

Model

We first define the volume-based energy density

$$E_v = \frac{P}{v \cdot h \cdot t} \ \left(\frac{J}{mm^3}\right) \quad (1)$$

Where, P is the laser power $(watts)$, v is the scan speed $(\frac{mm}{s})$, h is the hatch spacing (mm), and t is the layer thickness (mm). The energy density required to melt/fuse a single particle is E_m, (i.e some portion of Ev is required to melt a single particle where that portion is defined by the volume e which is unknown).

$$E_m = eE_v \quad (2)$$

$$E_m = (C_p \Delta \mathrm{T} + C_1)\ \rho \mathrm{V} \quad (3)$$

Where $C_p$is the specific heat of the powder ($\frac{J}{KgK^{\circ}}$), $C_1$is the latent melt energy ($\frac{J}{kg}$) or latent heat of fusion of the powder, ρ is the density ($\frac{kg}{mm^3}$), V is the volume of the particle (assumed sphere)(mm^3). Simply put the amount of energy to melt a particle is the enthalpy + the latent heat of fusion (to get the total energy in the system per unit kg) multiplied by the mass of one particle to find the energy required to melt a single particle.

Working with equation (3) and substituting equation (2)

$$eE_v = (C_p \Delta \mathrm{T} + C_1)\ \rho \mathrm{V} \tag{5}$$

Now substitution of equation (1) into (5)

$$e \cdot \frac{P}{v \cdot h \cdot t} = (C_p \Delta \mathrm{T} + C_1)\ \rho \mathrm{V} \tag{6}$$

$$e \cdot \frac{P}{v \cdot h \cdot t \cdot \rho \cdot \mathrm{V}} = (C_p \Delta \mathrm{T} + C_1) \tag{7}$$

$$\Delta \mathrm{T} = e \cdot \frac{P}{C_p \cdot v \cdot h \cdot t \cdot \rho \cdot \mathrm{V}} - \frac{C_1}{C_p} \tag{8}$$

Let,

$$K = \frac{e}{C_p \rho \cdot \mathrm{V}} \tag{9}$$

And sub into (8)

$$\Delta \mathrm{T} = \mathrm{K} \cdot \frac{P}{v \cdot h \cdot t} - \frac{C_1}{C_p} \tag{10}$$

In this simulation the layer to layer dynamics are models using a first order response. The transient response the model is as followers

$$\Delta \mathrm{T} = \mathrm{K} \cdot \frac{P}{v \cdot h \cdot t} * \frac{K'}{\mathrm{s} + t_w} \tag{11}$$

We assume that $K' * K = K$ resulting in

$$\Delta T = \frac{P}{v \cdot h \cdot t} * \frac{K}{s + t_w} \tag{12}$$

Where the control signal U is a demand in power (P) and the temperature change is the output. To approximate K, we set ΔT to be 1450°C (1724K) (the melting point of IN625) in (13) and solve for K Using variable values from Table 1 below and the Matlab simulation. It is found that K= 6.

Table 1: Model Parameter Values	
Variable	Value
K	6
P	150-400 W
v	0.2-0.6 m/s = 200mm/s – 600 mm/s
h	100 um = 0.1mm
t	20-40 um = 0.02-0.04mm
C1	227 J/kg [43]
Cp	412 J/KgK [43]

Using a ZOH (sample time = 0.01 seconds) we obtain the discrete time:

$$Gz = \frac{0.07478}{z - 0.994} \tag{14}$$

Simulation

In order to simulate the control system some considerations must be taken into account about the system. Firstly we are considering the system to be point on a section of a track rather then the entire track or build as outlined in Chapter 2. dynamics of the of the cooling will not be directly consider the but rather peak to peak temperature. In the following figure it can be seen that a simplified simulation of the controller and temerpature signal has been developed. In the large circle is each change in laser power and in small circle is the peak temperature from the laser.

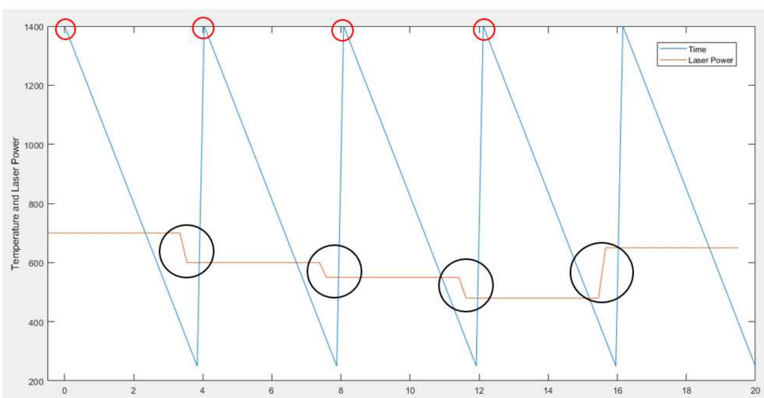

Figure 56: Simplified Simulation of Temperature and Laser Power Control

If the decrease in temperature is not consdiered then it can be looked at as peak temperature being a discrete signal in which each peak temperature is a data point. This works nicely with the feedback sensors because both can measure the highest temperature in the FOV. That being said if the decrease in temperature is not considered then the controller will always think that the meltpool temperature is correct (or nearly) as it reads the peak temperature from the previous layer which will be close to the desired temperature and thus the control signal will be to low to maintain the temperature. To componsate for this an additional variable is introduced called K_drop which is a tuning parameter used to estimate the temperature drop and could be done in situ using the thermal camera. K_drop works by adding an additional gain to the feedback loop of the controller. Additionally the simulation incopreates white noise in the feedback loop by multiplying the loop by random value before the K_drop gain. The final control loop is shown Figure 57, with this finilized the implementation and discretization of the PID controller could be explored.

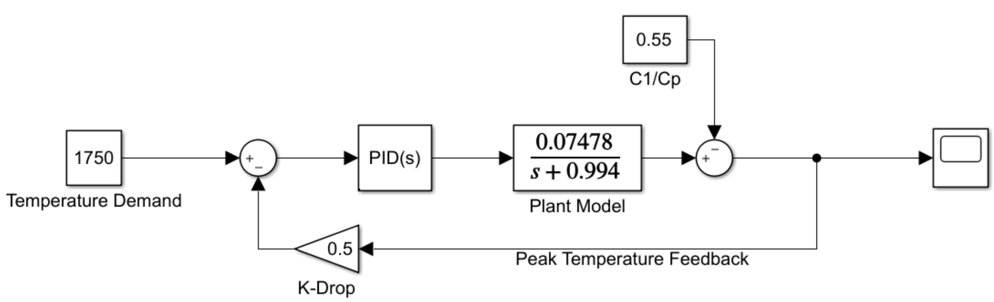

Figure 57: Closed loop controller

Discrete PID control

The differential equation to describe the PID controller is;

$$u(t) = K_p \left[e(t) + K_d \dot{e}(t) + K_i \int_0^t e(t) dt \right]$$

Where,

$$The\ error\ e(t) = r(t) - y(t)$$

$$K_p = Proportional\ Gain\ K_i = Integral\ Control\ K_d = Derivative\ Control$$

Assuming zero initial conditions the Laplace transform can be taken

$$\mathcal{L}\{u(t)\} = U(s) = K_p \left[E(s) + K_d E(s) + K_i \tfrac{1}{s} E(s) \right]$$

∴ The transfer function is

$$D(s) = \frac{U(s)}{E(s)} = K_p \left[1 + K_d + K_i \frac{1}{s} \right]$$

Using backward differentiation, we obtain the discrete time transfer function

$$D(z) = \frac{U(z)}{E(z)} = K_p \left[1 + K_d \frac{z-1}{Tz} + K_i \frac{Tz}{z-1} \right]$$

In order to solve the simulation equations, we rearrange

$$\frac{U(z)}{E(z)}(z^2 - z) = K_p(z^2 - z) + K_p K_d \frac{(z-1)^2}{T} + K_p K_i T z^2$$

$$\frac{U(z)}{E(z)}(z^2 - z) = \left[K_p + \frac{K_p K_d}{T} + K_p K_i T \right] z^2 + \left[K_p + \frac{2K_p K_d}{T} \right] z + \frac{K_p K_d}{T}$$

$$Let\ K_1 = \left[K_p + \frac{K_p K_d}{T} + K_p K_i T\right], K_2 = \left[K_p + \frac{2K_p K_d}{T}\right], K_3 = \frac{K_p K_d}{T}$$

To obtain the discrete transfer function which can be programmed with we use the difference equation assuming zero initial conditions

$$U(z)z^2 - U(z)z = K_1E(z)z^2 + K_2E(z)z + K_3E(z)$$

$$U(z) - U(z)z^{-1} = K_1E(z) + K_2E(z)z^{-1} + K_3E(z)z^{-2}$$

$$u(k) - u(k-1) = K_1e(k) + K_2e(k-1) + K_3e(k-2)$$

$$u(k) = K_1e(k) + K_2e(k-1) + K_3e(k-2) + u(k-1)$$

Testing

The simulation could be implemented in Matlab and testing could begin. Three main areas researched to observe their effects on the controller;

1) Constraints on the control signal (i.e. laser power limits)
2) Modelling Error
3) Effects of Noise

For each of these areas the response time, percent overshoot and settling times were compared. It should be noted that the response time and settling of this system are quite interesting, as the laser power only gets changed from layer to layer the response time is quite long and can take from a few seconds to a full minute depending on the complexity of the build. In this simulation we consider each layer to take 10 seconds. For the sake of this paper and the understanding of the effects the response and settling time they will be considered in the number of layers it takes to reach 90% of the final value and reach steady state (1% of final value) rather then the time.

For these experiments a setpoint of 1400C was used and IN625 process parameters were used. In the simulations the following parameter set were used ;Noise = 100, Umin = 100 and Umax =400, and assuming a perfect model, unless one of those parameters were being changed. For example, when laser power is changed (Control Constraint) noise is kept constant and modelling error is 0 well laser power is changed and so forth for each parameter change.

Trial 1: Control Constraints

In the first simulations a constraint placed on the control signal is tested with three separate constraints on the minimum and maximum values of laser power. The following table summarizes the results from these tests. It can be seen in Table 21 that as the constraint on the laser power is tightened the response and settling

time increase

Table 21: Trial 1 response time, settling time and overshoot

Trial Number	**Control Signal Constraint**	**Response Time**	**Settling Time**	**%Overshoot**
1.1	U - min 150 U - max 400	12 Layers	20 Layers	0.286%
1.2	U - min 200 U - max 350	18 Layers	34 Layers	0.191%
1.3	U - min 250 U - max 300	31 Layers	48 Layers	0.102%

Interestingly the overshoot decreases, which is do to the fact that the controller is less aggressive because it cannot command the power it wants resulting in a more gentle increase to the setpoint, confirmed by the pattern in response and settling time. An example of the response of the laser and system is shown in Figure 58 and Figure 59. The response and laser power response from all three trials can be seen in the Appendix A. Control Signal and Step Response (Control Constraint).

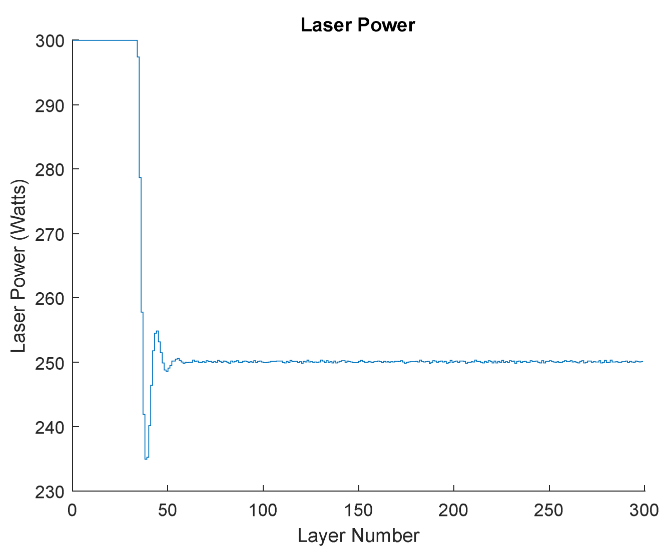

Figure 58: Constrained laser power demand

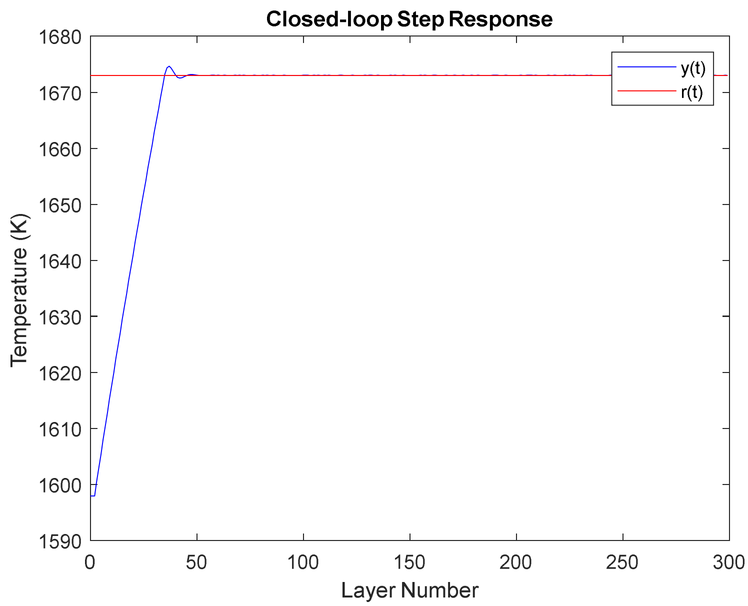

Figure 59: Closed -loop step response with constraint on laser power

Trial 2: Modelling Error

In the second set of trials .modelling error was tested next with modeling errors of -20%, +50% and +100%. The results are recorded in Table 22. Compared to a perfect model the response and settling time decreased when the error was positive and decreased when the error was negative where as percent overshoot behaved inversely. The laser power demand also decreased as modelling error decreased proven by the fact that it spends less time saturated. An example of the response can be found in Figure 60 and Figure 61 while the remaining plots for the other trials can be found in the Appendix B. Control Signal and Step Response (Modeling Errors).

Table 22: Trial 2 response time, settling time and overshoot

Experiment Number	**Modelling Error**	**Response Time**	**Settling Time**	**%Overshoot**
2.1	0.8	24	40	0.173%
2.2	1.5	7	18	0.399%
2.3	2	5	15	0.357%

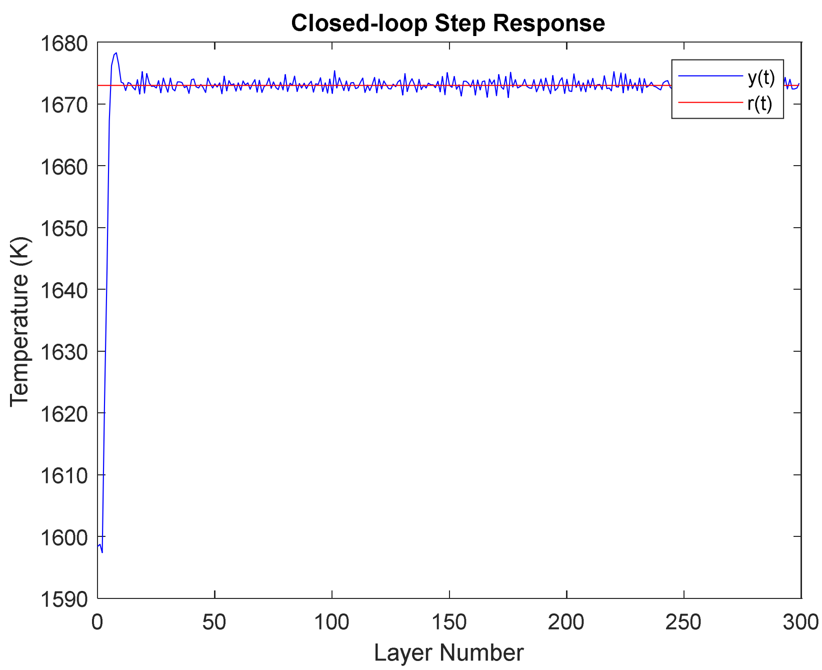

Figure 60: Closed -loop step response with modelling error

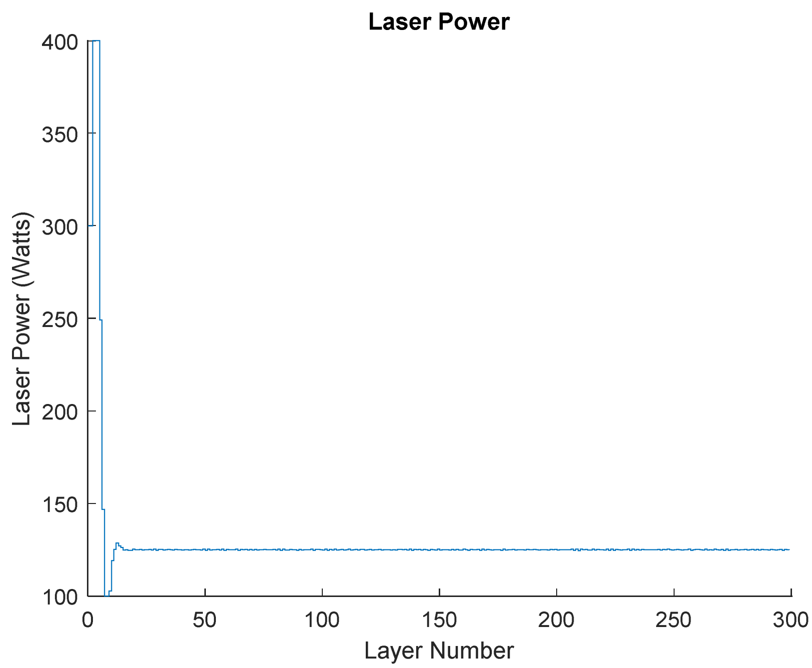

Figure 61: Laser power demand with modelling error

Trials 3: Effects of noise

Noise had some fascinating results with the control signal. As noise increased the demand for laser power became more erratic to the point where at 10000 noise value the actuator reached saturation after the temperature had reached 90% of its final value. Additionally, when noise was increased an increase in percent overshoot was seen and at max noise the signal never settled to 1% of its final value. The response of the controller and laser power can be seen in the appendix. An example of the response can be found inf Figure 63 and Figure 62 while the remaining plots for the other trials can be found in the Appendix C.. Control Signal and Step Response (Effects of Noise)

Table 23: Trial 3 response time, settling time and overshoot

Experiment Number	Noise Value	Response Time	Settling Time	%Overshoot
3.1	100	13	27	0.286%
3.2	1000	13	23	0.274%
3.3	10000	12	NA	0.594%

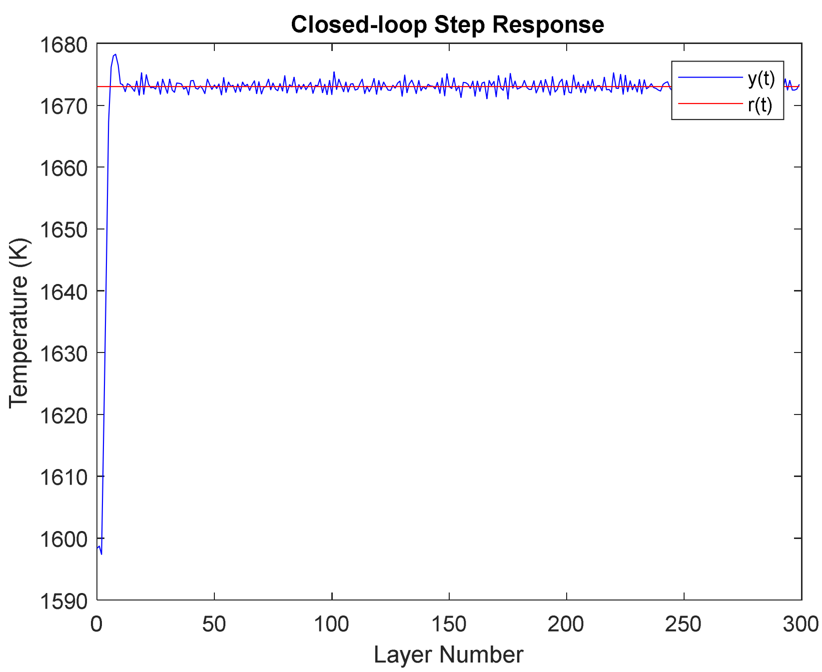

Figure 62: Closed -loop step response with noise

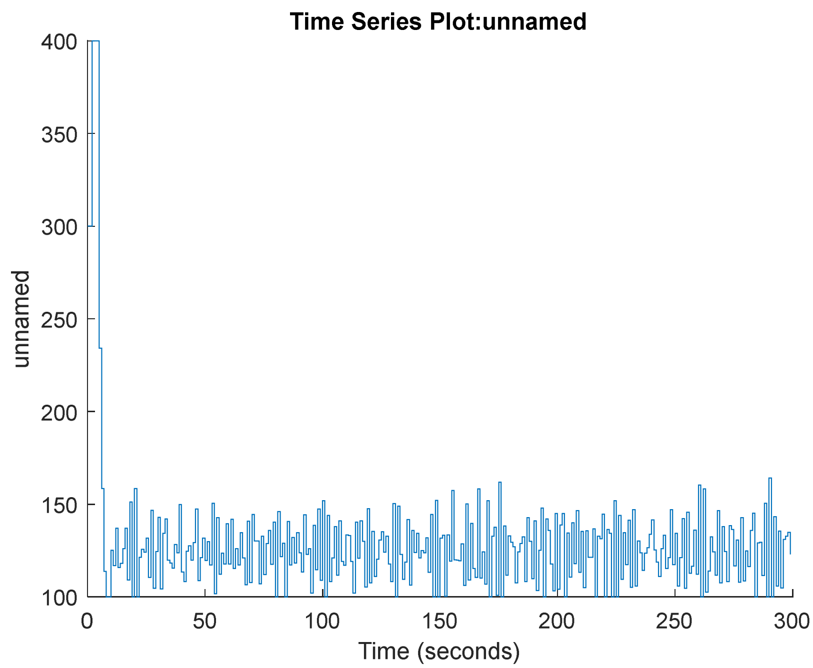

Figure 63: Laser power demand with noise

Controller Interface

Two methods were developed for interfacing with the laser power on the Omnisint 160 in order to change its value in situ. The first method is a software solution which allows for any process parameter to be changed between each layer. In the second method it is only possible for the laser power as this method interrupts the laser control signal and changes it to either increase or decrease the laser power during each layer.

Method 1: Handshake

In this method the software running the Omnisint 160 called OmniMark was altered. The pyrometer and camera are connected directly to the temperature controller using Gig E for the pyrometer and USB for the thermal camera. To change the laser power or any other process parameter a process to perform a handshake with the Laser Controller was developed and explained below.

At the end of each layer, OmniMark writes the string "LAYER DONE" to file called LayerDone.txt present in the same directory as the Omnimark100.exe file. It polls every 0.5 seconds to see if the file LayerStart.txt contains the string "LAYER START". If it does the layer will start and the OMnimark software will clear LaserStart.txt.

The controller only needs to poll for the file LayerDone.txt every 0.5 seconds until it reads "LAYER DONE" in that file. Once it reads "LAYER DONE" it will write the parameters.txt file with the new process parameters. Then it writes the string " " to file LayerDone.txt and writes the string "LAYER START" to file LayerStart.txt thus starting the layer. A flow chart of this decision making can be found below.

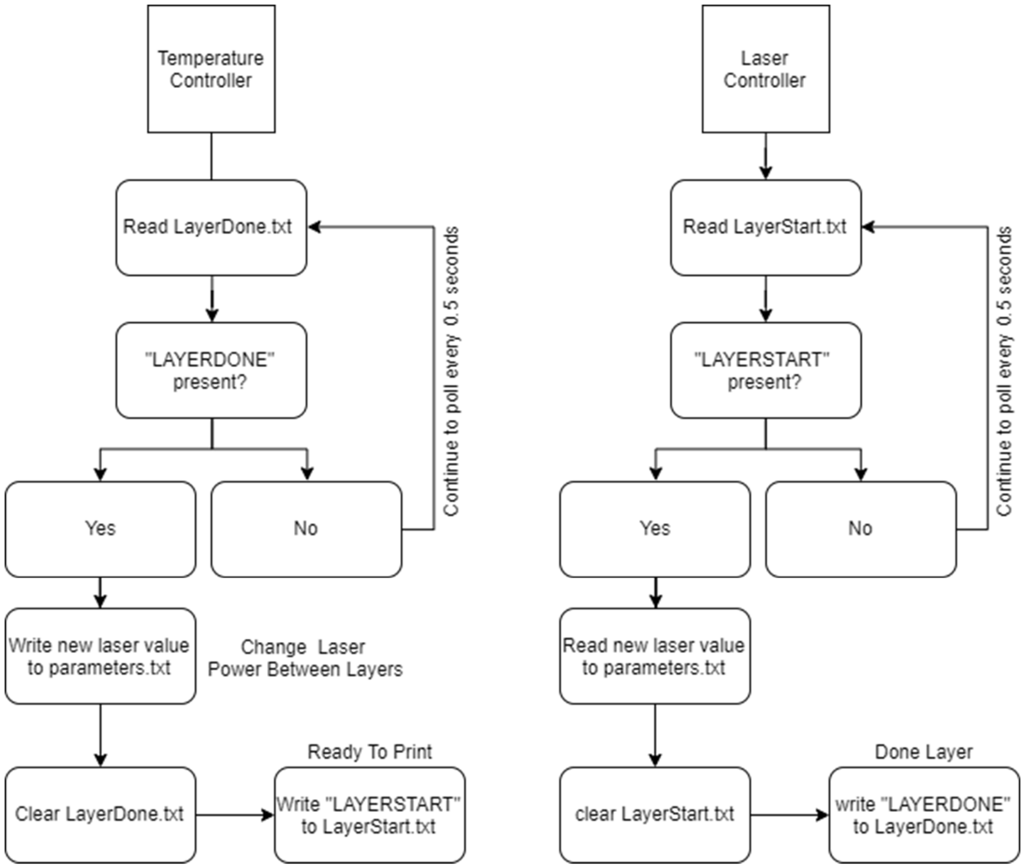

Figure 64: Handshake Flow Chart

This method allows for the temperature controller to only need to monitor two text files and can very easily interface with a program such as LabView. This method was implemented and tested with no controller.

Method 2: Change laser power during the build process

This method has not been employed on the machine but the concept has been outlined. As seen in the figure below it is possible to interrupt the signal which communicates between the Omnisint 160 controller and the laser controller (Line QA2). By interrupting this signal changes can be made to the laser controller from the temperature controller through pins 22 and 25 on the laser controller. This allows for the laser power to be changed at any time, not just between layers. This methodology may also have an RS232 or USB connection to the host computer of the Omnisint 160 to read or write other process parameters between layers using Method 1.

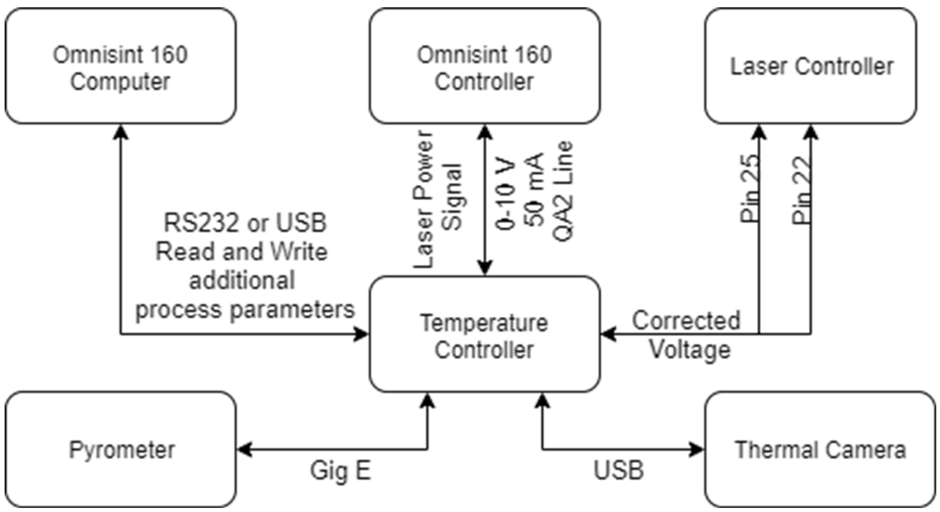

Figure 65: Concept for changing laser power within a track

Conclusion

In conclusion the literature review conducted revealed that additively manufactured components are not reliable, often having internal voids, accuracy issues nd very poor surface finish [3]. Most importantly for the application of AM to be wide spread the technology needs to make significant strides to increase the reliability of additively manufactured parts. To make these strides there is a push to learn more about AM and to try and control the process more tightly to increase part quality. The goal of this research was to lay the ground work so that a controller could be implemented on a SLM printer called the Omnisint 160. To do this a monitoring system was developed using a pyrometer and thermal imager mounted on the Omnisint 160 to record the peak temperature of the melt pool. The pyrometer and thermal imager were carefully selected and calibrated to ensure their accuracy. Additionally, thermocouples were tested as a potential third measurement point for the monitoring systems, however did not have sufficient response times for the speed of the process and was therefore not used.

The success of this monitoring system allowed for experiments to be run to explore different relationships of input and output parameters. It was found that laser power affected the peak melt pool temperature, as the power was increased the peak melt pool temperature also increased. This was confirmed for both IN625 and Invar 36. Similar to the effects of laser power scan speed also affected the peak melt pool temperature. As the scan speed was decreased the peak melt pool temperature increased. From the experiments run with the thermal camera a trend could not be found across a laser track. That is to say the temperature profile at the beginning middle and end of a track was even, and no single area showed as being predominantly hotter or colder. This could be significant in the assumptions made by a layer to layer controller. In addition to examining the temperature across a laser track the melt pool temperature profile was examined resembled a second order response to laser. This could help develop a model in the future for laser power control within each laser track.

Offline measurements were also taken of the PDAS of the as-built IN625 coupons and it was found that as peak temperature increased the PDAS also increased. This makes sense as the higher peak temperature allows for longer cooling times giving the dendrites more time to grow. It is suspected that the laser power is directly tied to the microstructure as the laser power dictates the peak temperature and peak temperature effects the microstructure. However, additional experiments would need to be run to ensure no other factors were at involved in the results PDAS.

In addition to the monitoring system a first order model of the system was created and successfully simulated using a discreet PID controller. Lastly, two separate methods were found to interface a controller with the Omnisint 160 so that this simulation or other controllers could change the laser power based on the temperature feedback.

Overall this research was successful and contributed unique data about the temperatures in the selective laser melting of IN625. Furthermore, the monitoring system and interface methods allow for the implementation of a control system which can monitor the temperature of the melt pool and change process parameters in situ.

Bibliography

[1] Wohlers, "What is Additive Manufacturing?," 2010. [Online]. Available: https://wohlersassociates.com/additive-manufacturing.html. [Accessed: 14-Dec-2019].

[2] T. G. Spears and S. A. Gold, "In-process sensing in selective laser melting (SLM) additive manufacturing," *Integr. Mater. Manuf. Innov.*, 2016.

[3] A. V. Gusarov, A. A. Okun'kova, P. Y. Peretyagin, I. V. Zhirnov, and P. A. Podrabinnik, "Means of Optical Diagnostics of Selective Laser Melting with Non-Gaussian Beams," *Meas. Tech.*, vol. 58, no. 8, pp. 872–877, 2015.

[4] J. Gockel and J. Beuth, "Understanding Ti-6Al-4V Microstructure Control in Additive Manufacturing via Process Maps Joy Gockel and Jack Beuth Department of Mechanical Engineering, Carnegie Mellon University, Pittsburgh, PA 15213," *4th Int. SFF Symp. - An Addit. Manuf. Conf.*, pp. 666–674, 2013.

[5] J. L. Beuth *et al.*, "Process Mapping for Qualification Across Multiple Direct Metal Additive Manufacturing Processes," *Proc. Solid Free. Fabr. Symp.*, pp. 655–665, 2014.

[6] J. Fox and J. Beuth, "Process mapping of transient melt pool response in wire feed e-beam additive manufacturing of Ti-6Al-4V," *24th Int. SFF Symp. - An Addit. Manuf. Conf. SFF 2013*, pp. 675–683, 2013.

[7] J. Gockel, J. Fox, J. Beuth, and R. Hafley, "Integrated melt pool and microstructure control for Ti-6Al-4V thin wall additive manufacturing," *Mater. Sci. Technol. (United Kingdom)*, vol. 31, no. 8, pp. 912–916, 2015.

[8] J. Gockel, J. Beuth, and K. Taminger, "Integrated control of solidification microstructure and melt pool dimensions in electron beam wire feed additive manufacturing of ti-6al-4v," *Addit. Manuf.*, vol. 1, pp. 119–126, 2014.

[9] P. A. Kobryn and S. L. Semiatin, "Microstructure and texture evolution during solidification processing of Ti – 6Al – 4V," vol. 135, pp. 330–339, 2003.

[10] S. Bontha, N. W. Klingbeil, P. A. Kobryn, and H. L. Fraser, "Thermal process maps for predicting solidification microstructure in laser fabrication of thin-wall structures," vol. 178, pp. 135–142, 2006.

[11] C. Li, Y. B. Guo, and J. B. Zhao, "Journal of Materials Processing Technology Interfacial phenomena and characteristics between the deposited

material and substrate in selective laser melting Inconel 625," vol. 243, pp. 269–281, 2017.

[12] G. P. Dinda, A. K. Dasgupta, and J. Mazumder, "Laser aided direct metal deposition of Inconel 625 superalloy : Microstructural evolution and thermal stability," vol. 509, pp. 98–104, 2009.

[13] J. T. Mckeown *et al.*, "Time-Resolved In Situ Measurements During Rapid Alloy Solidification : Experimental Insight for Additive Manufacturing," vol. 68, no. 3, 2016.

[14] L. E. Murr, E. Martinez, S. M. Gaytan, D. A. Ramirez, and B. I. Machado, "and Mechanical Properties for a Nickel-Base Superalloy Fabricated by Electron Beam Melting," vol. 42, no. November, pp. 3491–3508, 2011.

[15] S. Li, Q. Wei, Y. Shi, Z. Zhu, and D. Zhang, "Journal of Materials Science & Technology Corrigendum to Microstructure Characteristics of Inconel 625 Superalloy Manufactured by Selective Laser Melting Journal of Materials Science & Technology , Volume 31 (2015), Pages 946 – 952," *J. Mater. Sci. Technol.*, vol. 32, no. 7, p. e1, 2016.

[16] S. Bontha and N. W. Klingbeil, "Thermal Process Maps for Controlling Microstructure in Laser-Based Solid Freeform Fabrication," *SFF Proc.*, pp. 219–226, 2003.

[17] M. Doubenskaia, S. Grigoriev, I. Zhirnov, and I. Smurov, "Parametric analysis of SLM using comprehensive optical monitoring," *Rapid Prototyp. J.*, vol. 22, no. 1, pp. 40–50, 2016.

[18] G. W. J. Z, Jacobsmuhlen, S, Kleszczynski, D, Schneider, "High resolution imaging for inspection of laser beam melting systems," *2013 IEEE Int. Instrum. Meas. Technol. Conf.*, 2013.

[19] H. Krauss, T. Zeugner, and M. F. Zaeh, "Layerwise monitoring of the Selective Laser Melting process by thermography," *Phys. Procedia*, vol. 56, no. C, pp. 64–71, 2014.

[20] C. J-P, Kruth, P, Mercelis, J, Vaerenbergh, C, "Hybrid Simulation : Combining Constraints and Impulses," *Proc. First Work. Simul. Interact. Virtual Environ.*, pp. 1–7, 1995.

[21] A. V. Gusarov, A. A. Okun'kova, P. Y. Peretyagin, I. V. Zhirnov, and P. A. Podrabinnik, "Means of Optical Diagnostics of Selective Laser Melting with Non-Gaussian Beams," *Meas. Tech.*, vol. 58, no. 8, pp. 872–877, 2015.

[22] A. Segerstark, J. Andersson, and L. E. Svensson, "Evaluation of a

temperature measurement method developed for laser metal deposition," *Sci. Technol. Weld. Join.*, vol. 22, no. 1, pp. 1–6, 2017.

[23] M. F. Zäh and S. Lutzmann, "Modelling and simulation of electron beam melting," *Prod. Eng.*, vol. 4, no. 1, pp. 15–23, 2010.

[24] L. Qian, J. Mei, J. Liang, and X. Wu, "Influence of position and laser power on thermal history and microstructure of direct laser fabricated Ti–6Al–4V samples," *Mater. Sci. Technol.*, vol. 21, no. 5, pp. 597–605, 2005.

[25] S. Price, J. Lydon, K. Cooper, and K. Chou, "Temperature Measurements in Powder-Bed Electron Beam Additive Manufacturing," *ASME Int. Mech. Eng. Congr. Expo. Proc.*, vol. 2, Nov. 2014.

[26] H. Rieder, M. Spies, J. Bamberg, and B. Henkel, "On- and offline ultrasonic characterization of components built by SLM additive manufacturing," *AIP Conf. Proc.*, vol. 1706, no. February, 2016.

[27] J. B. Spicer, "In situ, laser-ultrasonic monitoring of stainless steel microstructure evolution during heat treatment," *High Temp. Mater. Sci.*, vol. 37, no. 1, 1997.

[28] M. H. Farshidianfar, A. Khajepour, and A. Gerlich, "Real-time control of microstructure in laser additive manufacturing," *Int. J. Adv. Manuf. Technol.*, vol. 82, no. 5–8, pp. 1173–1186, 2016.

[29] W. Devesse, D. De Baere, M. Hinderdael, and P. Guillaume, "Hardware-in-the-loop control of additive manufacturing processes using temperature feedback," *J. Laser Appl.*, vol. 28, no. 2, p. 022302, 2016.

[30] C. Doumanidis and Y. M. Kwak, "Geometry modeling and control by infrared and laser sensing in thermal manufacturing with material deposition," *J. Manuf. Sci. Eng. Trans. ASME*, vol. 123, no. 1, pp. 45–52, 2001.

[31] E. Rodriguez *et al.*, "Integration of a thermal imaging feedback control system in electron beam melting," *23rd Annu. Int. Solid Free. Fabr. Symp. - An Addit. Manuf. Conf. SFF 2012*, no. Figure 1, pp. 945–961, 2012.

[32] D. Hu and R. Kovacevic, "Sensing, modeling and control for laser-based additive manufacturing," *Int. J. Mach. Tools Manuf.*, vol. 43, pp. 51–60, 2002.

[33] L. I. of America, "Laser Ultrasonic Inspection of Laser Cladded 316LSS and Ti-6-4," *ICALEO*, vol. 23, 2004.

[34] K. et Al., “Laser-ultrasonic detection of sub- surface defects in processedmetals: NO 7,278,315 B1,” 2005.

[35] A. J. Manzo and H. Helvajian, “ Pulsed laser ultrasonic excitation and heterodyne detection for in situ process control in laser 3D manufacturing ,” *J. Laser Appl.*, vol. 29, no. 1, p. 012012, 2017.

[36] R. B. Dinwiddie, R. R. Dehoff, P. D. Lloyd, L. E. Lowe, and J. B. Ulrich, “Thermographic in-situ process monitoring of the electron-beam melting technology used in additive manufacturing,” *Thermosense Therm. Infrared Appl. XXXV*, vol. 8705, no. May 2013, p. 87050K, 2013.

[37] S. Price, K. Cooper, and K. Chou, “EVALUATIONS OF TEMPERATURE MEASUREMENTS BY NEAR-INFRARED THERMOGRAPHY IN POWDER-BASED ELECTRON-BEAM ADDITIVE MANUFACTURING,” pp. 761–773, 2012.

[38] L. Han, F. W. Liou, and S. Musti, “Thermal behavior and geometry model of melt pool in laser material process,” *J. Heat Transfer*, vol. 127, no. 9, pp. 1005–1014, 2005.

[39] L. Tang and R. G. Landers, “Melt Pool Temperature Control for Laser Metal Deposition Processes—Part I: Online Temperature Control,” *J. Manuf. Sci. Eng*, vol. 132, no. 1, pp. 1–9, 2010.

[40] L. Tang and R. G. Landers, “Melt pool temperature control for laser metal deposition processes-part II: Layer-to-layer temperature control,” *J. Manuf. Sci. Eng. Trans. ASME*, vol. 132, no. 1, pp. 0110111–0110119, 2010.

[41] A. V. Gusarov and I. Smurov, “Modeling the interaction of laser radiation with powder bed at selective laser melting,” *Phys. Procedia*, vol. 5, no. PART 2, pp. 381–394, 2010.

[42] Y. Li and D. Gu, “Parametric analysis of thermal behavior during selective laser melting additive manufacturing of aluminum alloy powder,” *Mater. Des.*, vol. 63, pp. 856–867, 2014.

[43] L. Criales, Y. M. Arısoy, and T. Özel, “Sensitivity analysis of material and process parameters in finite element modeling of selective laser melting of Inconel 625No Title,” *Int. J. Adv. Manuf. Technol.*, vol. 86, no. 9–12, pp. 2653–2666, 2016.

[44] M. Letenneur, A. Kreitcberg, and V. Brailovski, “Optimization of Laser Powder Bed Fusion Processing Using a Combination of Melt Pool Modeling and Design of Experiment Approaches: Density Control,” *J. Manuf. Mater.*

Process., vol. 3, no. 1, p. 21, 2019.

[45] K. Shahzad, J. Deckers, Z. Zhang, J. P. Kruth, and J. Vleugels, “Additive manufacturing of zirconia parts by indirect selective laser sintering,” *J. Eur. Ceram. Soc.*, vol. 34, no. 1, pp. 81–89, 2014.

[46] S. M. Yusuf and N. Gao, “Influence of energy density on metallurgy and properties in metal additive manufacturing,” *Mater. Sci. Technol.*, vol. 33, no. 11, pp. 1269–1289, Jul. 2017.

[47] T. Craeghs, F. Bechmann, S. Berumen, and J. P. Kruth, “Feedback control of Layerwise Laser Melting using optical sensors,” *Phys. Procedia*, vol. 5, no. PART 2, pp. 505–514, 2010.

[48] A. Fathi, A. Khajepour, M. Durali, and E. Toyserkani, “Geometry control of the deposited layer in a nonplanar laser cladding process using a variable structure controller,” *J. Manuf. Sci. Eng. Trans. ASME*, vol. 130, no. 3, pp. 0310031–03100311, 2008.

[49] L. Dong, A. Makradi, S. Ahzi, and Y. Remond, “Three-dimensional transient finite element analysis of the selective laser sintering process,” *J. Mater. Process. Technol.*, vol. 209, no. 2, pp. 700–706, 2009.

[50] A. V. Gusarov and I. Smurov, “Radiation transfer in metallic powder beds used in laser processing,” *J. Quant. Spectrosc. Radiat. Transf.*, vol. 111, no. 17–18, pp. 2517–2527, 2010.

[51] A. Anam, D. Pal, and B. Stucker, “Modeling and Experimental validation of Nickel-based super alloy (Inconel 625) made using Selective Laser Melting,” *J. B. Speed Sch. Eng. Univ. Louisv.*

[52] S. Clijsters, T. Craeghs, S. Buls, K. Kempen, and J.-P. Kruth, “In situ quality control of the selective laser melting process using a high-speed, real-time melt pool monitoring system,” *Int. J. Adv. Manuf. Technol.*, vol. 75, no. 5–8, pp. 1089–1101, 2014.

[53] D. Hu and R. Kovacevic, “Modelling and measuring the thermal behaviour of the molten pool in closed-loop controlled laser-based additive manufacturing,” *Proc. Inst. Mech. Eng. Part B J. Eng. Manuf.*, vol. 217, no. 4, pp. 441–452, 2003.

[54] J. Mireles, C. Terrazas, S. M. Gaytan, D. A. Roberson, and R. B. Wicker, “Closed-loop automatic feedback control in electron beam melting,” *Int. J. Adv. Manuf. Technol.*, vol. 78, pp. 1193–1199, 2015.

[55] T. Corporation, “TYPE K THERMOCOUPLE,” 2012. [Online]. Available:

https://www.thermometricscorp.com/thertypk.html.

[56] "How Do Ratio Pyrometers Work? | Fluke Process Instruments," 2019. [Online]. Available: https://www.flukeprocessinstruments.com/en-us/service-and-support/knowledge-center/infrared-technology/how-do-ratio-pyrometers-work. [Accessed: 29-Aug-2019].

[57] F. Inc., *Endurance Series Manual*. 2017.

[58] L. E. Criales, Y. M. Arısoy, B. Lane, S. Moylan, A. Donmez, and T. Özel, "Laser powder bed fusion of nickel alloy 625: Experimental investigations of effects of process parameters on melt pool size and shape with spatter analysis," *Int. J. Mach. Tools Manuf.*, vol. 121, no. March, pp. 22–36, 2017.

[59] V. D. Manvatkar, A. A. Gokhale, G. J. Reddy, U. Savitha, and A. De, "Investigation on laser engineered net shaping of multilayered structures in H13 tool steel," *J. Laser Appl.*, vol. 27, no. 3, p. 032010, 2015.

[60] V. Manvatkar, A. De, and T. DebRoy, "Spatial variation of melt pool geometry, peak temperature and solidification parameters during laser assisted additive manufacturing process," *Mater. Sci. Technol. (United Kingdom)*, vol. 31, no. 8, pp. 924–930, 2015.

[61] Y. P. Lei, H. Murakawa, Y. W. Shi, and X. Y. Li, "Numerical analysis of the competitive influence of Marangoni flow and evaporation on heat surface temperature and molten pool shape in laser surface remelting," *Comput. Mater. Sci.*, vol. 21, no. 3, pp. 276–290, 2001.

[62] K. N. Amato *et al.*, "Microstructures and mechanical behavior of Inconel 718 fabricated by selective laser melting," *Acta Mater.*, vol. 60, no. 5, pp. 2229–2239, 2012.

[63] C. U. Brown *et al.*, "The effects of laser powder bed fusion process parameters on material hardness and density for nickel alloy 625," *NIST Adv. Manuf. Ser.*, pp. 100–119, 2018.

Appendix

Appendix A. Control Signal and Step Response (Control Constraint)

	Control Signal	System Response
1.1	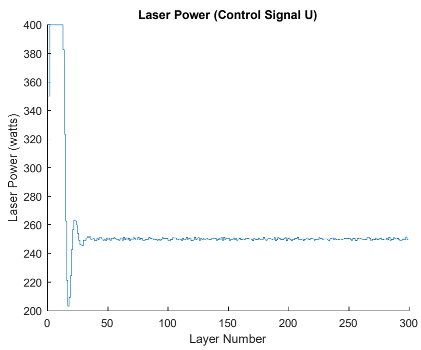	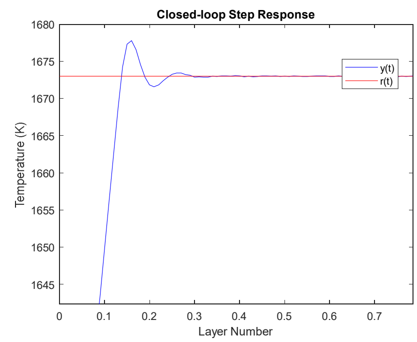
1.2	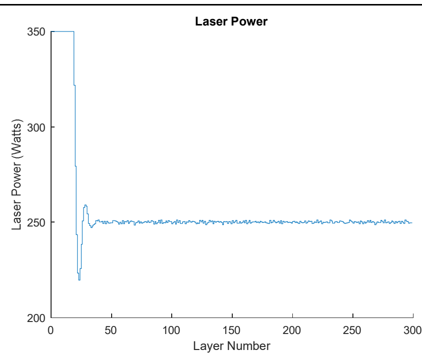	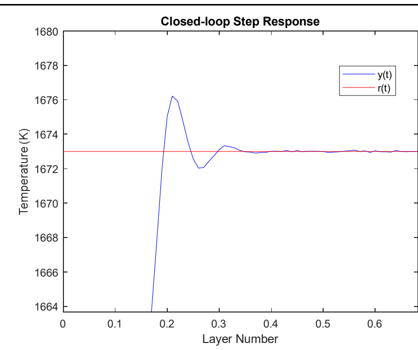
1.3	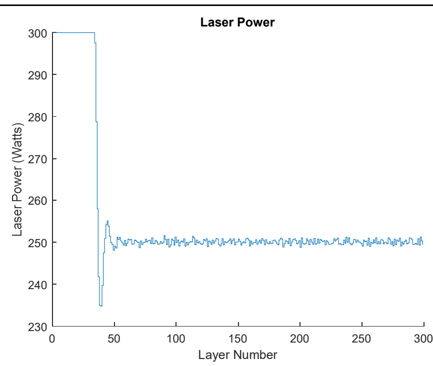	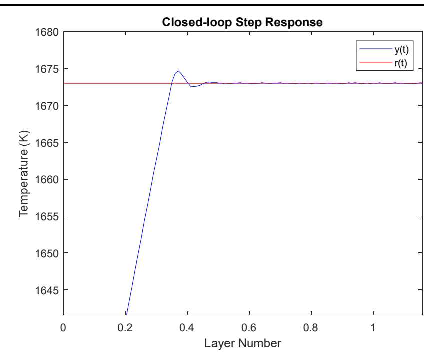

Appendix B. Control Signal and Step Response (Modeling Errors)

<table>
<tr><th></th><th>Control Signal</th><th>System Response</th></tr>
<tr><td>2.1</td><td>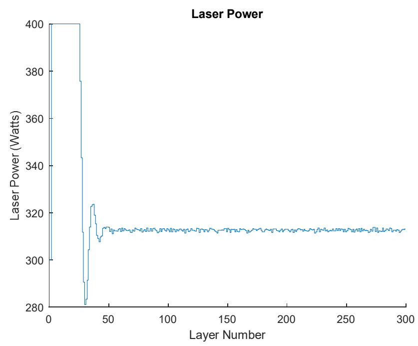
</td><td>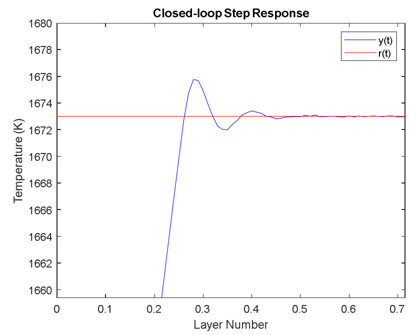
</td></tr>
<tr><td>2.2</td><td>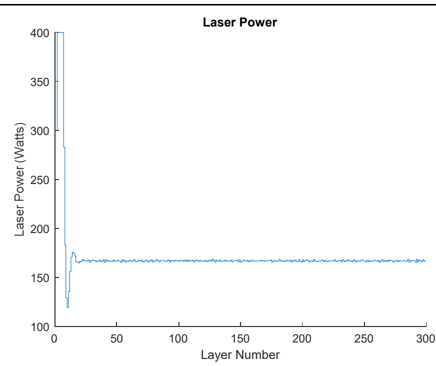
</td><td>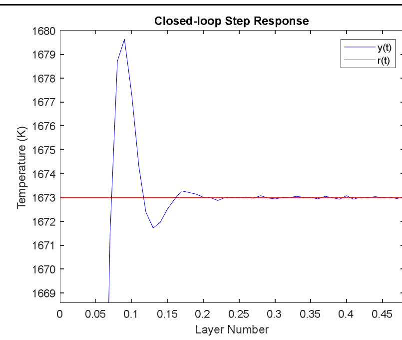
</td></tr>
<tr><td>2.3</td><td>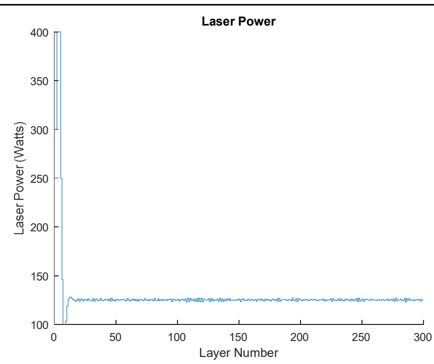
</td><td>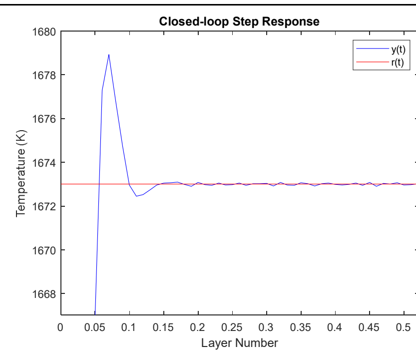
</td></tr>
</table>

Appendix C.. Control Signal and Step Response (Effects of Noise)

<table>
<tr><td></td><td>Control Signal</td><td>System Response</td></tr>
<tr><td>3.1</td><td>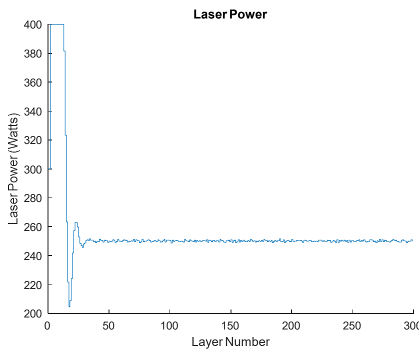
</td><td>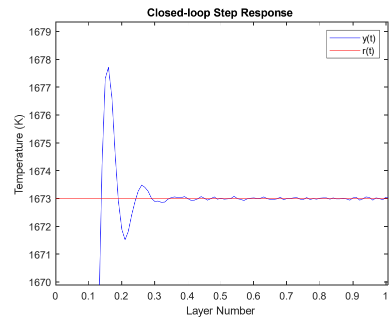
</td></tr>
<tr><td>3.2</td><td>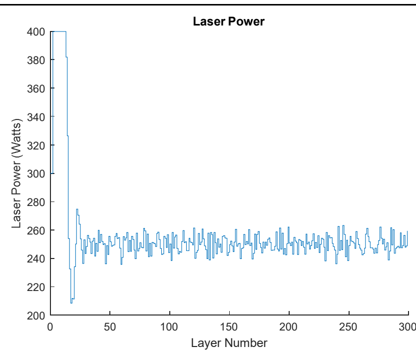
</td><td>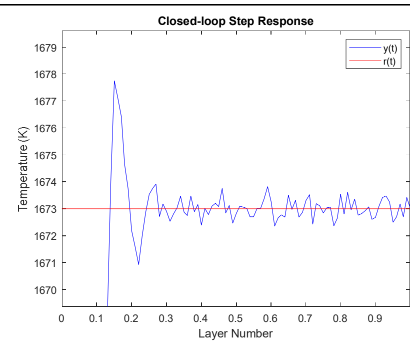
</td></tr>
<tr><td>3.3</td><td>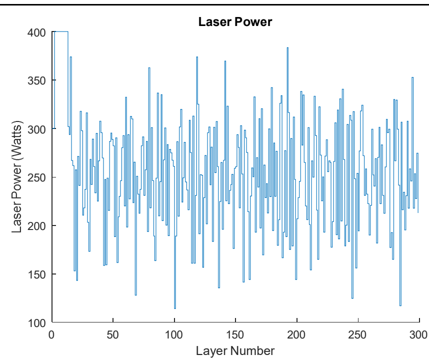
</td><td>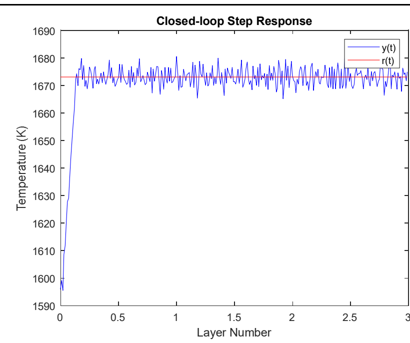
</td></tr>
</table>

Appendix D. Matlab code for simulation

```
clear all;
close all;
%%Model Paramters
s= tf('s');
K = 6; %
v = 200; %
h = 0.1; %
t = 0.04; %
tw = 0.6; % (FROM PAPER)
c1 = 227; %
cp = 412; % specific heat (j/kg)
num = (K/(v*h*t));
den = [1 tw];


%% System
Gs = tf(num,den); %(K'/(v*h*t))
T =0.01; %Sampling time of 50 mils
Gz = c2d(Gs,T);


%% Controller variables
Ku = 15;
Pu =0.1/5;
Kp=0.6*Ku;
Ki= 2/Pu;
Kd=Pu/8;
K1=Kp+(Kp*Kd/T)+(Kp*Ki*T);
K2=-Kp-(2*Kp*Kd/T);
K3=Kp*Kd/T;

%% SIMULATION SETUP

    %% Modeling Error
    Mod_Err= 2; %% 1 is zero modelling error

    Gs_error =  tf(num*Mod_Err,den); %(K'/(v*h*t))
    T =0.01; %Sampling time of 50 mils
    Gz_error = c2d(Gs_error,T); %discrete transfer function

    %% Noise parameter
    noise=40000;
    %% Control Constraints
    Umin = 100;%(must be low then umax and must be greater then
100)
```

```
    Umax = 400;%(must be greater then umin and must be less then
400)

    %% Additional model parameter inialisation
    N= 300; %Number of Layers
    setpoint = 1673;
    r=setpoint*ones(1,N);
    setpoint_error = -75;
    K_Drop = 1300;
    y=(setpoint+K_Drop+setpoint_error)*ones(1,N);
    ySensed=1400 *ones(1,N);
    u=300*ones(1,N);
    e=zeros(1,N);
    noise_signal= zeros(N);
    kdrop = (y(1) - K_Drop)/y(1);


%% Simulation
    for i=1:N

    % Noisy sensor (genereate signal from sensor based on )
      noise_signal(i) = noise*3E-4*(rand-0.5);
      ySensed(i)=(y(i)+ noise_signal(i))*kdrop; % - K_Drop;

    e(i)=r(i)-ySensed(i); %generate error signal
        if i>2
             u(i)=K1*e(i)+K2*e(i-1)+K3*e(i-2)+ u(i-1);
             if u(i) > Umax
                u(i) = Umax;
             end
           if u(i) < Umin
                u(i) =Umin;
            end
            y(i+1)=Gz_error.num{1}(2)*u(i) -
Gz_error.den{1}(2)*y(i);
            %y(i+1)=Gz.num{1}(2)*u(i) - Gz.den{1}(2)*y(i);
            y(i+1) = y(i+1) - c1/cp;

        end
    end
    %T= 0.05;
    time=T*(0:(N-1));
    layer = (0:N);
    figure
    plot(layer(1:N), ySensed(1:N),'b',layer(1:N),r,'r');
legend('y(t)', 'r(t)')
    %plot(time(1:N), ySensed(1:N),'b',time(1:N),r,'r');
legend('y(t)', 'r(t)')
    title('Closed-loop Step Response');
```

```
    xlabel('Layer Number');
    ylabel('Temperature (K)');


    figure
%   Ts = timeseries(ySensed(1:N),time);
%   ts = Ts.setinterpmethod('zoh');
%   plot(ts)
    hold
    Ts = timeseries(u(1:N),layer(1:N));
    ts = Ts.setinterpmethod('zoh');
    plot(ts)
    %plot(time(1:N), ySensed(1:N),'b',time(1:N),r,'r');
legend('y(t)', 'r(t)')

    title('Laser Power');
    xlabel('Layer Number');
    ylabel('Laser Power (Watts)');
```